Universität Bonn

Physikalisches Institut

Semileptonic Decays of Strange Beauty Mesons at Belle

Christian Oswald

Physikalisches Institut der Universität Bonn
Nußallee 12 - D-53115 Bonn

Semileptonic Decays of Strange Beauty Mesons at Belle

Dissertation
zur
Erlangung des Doktorgrades (Dr. rer. nat.)
der
Mathematisch-Naturwissenschaftlichen
Fakultät
der
Rheinischen Friedrich-Wilhelms-Universität
Bonn

von
Christian Oswald
aus
München

Bonn, April 2015

Dieser Forschungsbericht wurde als Dissertation von der Mathematisch-Naturwissenschaftlichen Fakultät der Universität Bonn angenommen und ist auf dem Hochschulschriftenserver der ULB Bonn `http://hss.ulb.uni-bonn.de/diss_online` elektronisch publiziert.

1. Gutachter:	Prof. Dr. Jochen Dingfelder
2. Gutachter:	Prof. Dr. Klaus Desch
Tag der Promotion:	19.06.2015
Erscheinungsjahr:	2015

Contents

CHAPTER 1

Introduction

The term “semileptonic decay” may sound exotic to persons not belonging to the small group of particle physicists. In fact, semileptonic decays are a very common phenomenon in nature. For example, the β decay

$$ {}^{14}_{6}\mathrm{C} \to {}^{14}_{7}\mathrm{N} + e^- + \bar{\nu}_e \,. \tag{1.1}$$

is a semileptonic decay. At the scale of the constituents of the atomic nucleus, the process is described as a neutron (n) decaying to a proton (p),

$$ n \to p + e^- + \bar{\nu}_e \,. \tag{1.2}$$

In particle physics, the proton and the neutron are not elementary, but composed of so-called up (u) quarks and down (d) quarks with $p = uud$ and $n = udd$. In this picture, the process is expressed as a d quark decaying into a u quark,

$$ d \to u + e^- + \bar{\nu}_e \,. \tag{1.3}$$

Since no substructure of the quarks has been found yet, the described process changes an intrinsic property of matter. This property is called “flavour”. The particles u, d, e^- and ν_e suffice to describe ordinary mat-

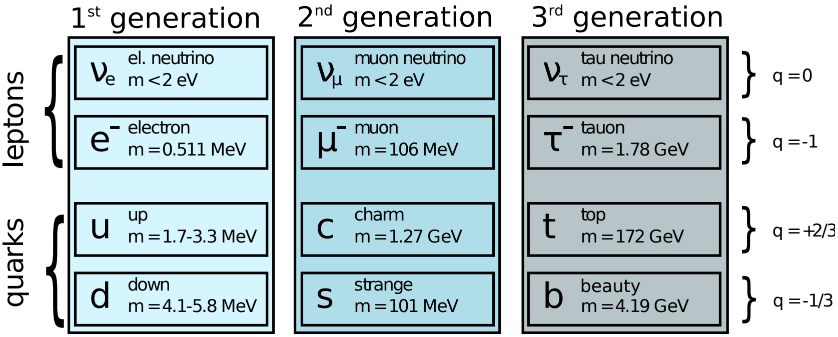

Figure 1.1: The elementary particles of the standard model. Figure taken from Ref. [1].

ter on earth. In the last century, however, heavier copies of these elementary particles (and their anti-particles) were discovered (see Fig. 1.1). These heavy relatives are produced in collisions of high-energy particles from extraterrestrial sources with particles in the Earth's atmosphere or they are produced at dedicated particle collider experiments. In this thesis, semileptonic decays of B_s mesons produced at KEK[1] in Tsukuba, Japan, are investigated. The B_s meson is composed of a $\bar{b}s$ quark pair[2]. In semileptonic decays, or more generally, in charged weak decays, quarks prefer to decay to the partner quark from the same generation. The mass of the b quark is, however, two orders of magnitude smaller than the mass of its partner, the t quark. A decay within the same generation is thus energetically not allowed and the b quark can only decay into a quark of the first or second generation. Among these, the decay

$$\bar{b} \to \bar{c} + e^+ + \nu_e \,, \tag{1.4}$$

is the most likely. This transition has been studied already in great detail by analysing the decays of $B^0 = \bar{b}d$ and $B^+ = \bar{b}u$ mesons (for

---

[1] KEK = kō-enerugī kasokuki kenkyū kikō = High Energy Accelerator Research Organization

[2] A horizontal line above a particle name denotes the corresponding anti-particle, $\bar{b}$ is for example the anti-beauty quark.

a review see Ref. [2]). What is the motivation to additionally study semileptonic B_s decays? The simple answer is: because they have not been studied yet in detail. Table 1.1 reviews the state of the art of semileptonic B_s decays before this thesis was started.

In this thesis, the decays $B_s \rightarrow D_s X \ell \nu$ and $B_s \rightarrow D_s^* X \ell \nu$ are investigated, where the symbol X stands for an arbitrary number (including zero) of additional hadrons and photons in the final state. The measurement of the yield of $B_s \rightarrow D_s X \ell \nu$ decays also allows for a precise determination of the number of B_s mesons contained in the Belle data set. Moreover, the $B_s \rightarrow X \ell \nu$ branching fraction is measured. This quantity has been measured before, but its precision has to be improved to be comparable to their equivalent in B[3] decays.

The fact that one can measure "something new" does not justify for a physicist the effort to carry out a measurement; there has to be some deeper connection to the understanding of the physical laws governing the world. In general, semileptonic $B_{(s)}$ decays allow for an extraction of the transition probability of a $\bar{b}$ to a $\bar{c}$ quark in processes of the charged weak interaction. This transition probability is expressed in the standard model of particle physics by the complex element V_{cb} of the Cabibbo-Kobayashi-Maskawa (CKM) matrix. Being a fundamental physical constant, V_{cb} cannot be derived from first principles; it has to be determined experimentally and semileptonic $B_{(s)}$ decays are particularly suited for this purpose. There is however an obstacle in the way: the $\bar{b}$ quark cannot be investigated as a free particle because it is contained in a bound state of a $B^0 = \bar{b}d$, $B^+ = \bar{b}u$ or $B_s = \bar{b}s$ meson held together by the strong interaction. These strong forces are described by the theory of Quantum Chromodynamics (QCD). A good understanding of the impact of QCD processes on semileptonic $B_{(s)}$ decays is crucial for the determination of V_{cb}. This is exactly where studies of semileptonic B_s decays become important. QCD itself is insensitive to the quark flavour, i.e. it does not matter if the decaying $\bar{b}$ quark is contained in a B or a B_s quark. This behaviour is described by $\mathrm{SU}(3)_{\mathrm{flavour}}$ symmetry. However, while the masses of the u and d quarks are comparable, the s quark is significantly heavier. QCD predicts that the differences between semileptonic B and B_s decays caused by this breaking

---

[3] The notation "B" denotes in this thesis the non-strange b-flavoured mesons B^0 and B^+.

Mode	Branching fraction [%]	Experiment
$B_{(s)} \to Xe\nu$	10.0 ± 1.0	CUSB [3]
$B_s \to X\ell\nu$	10.2 ± 1.2	Belle [4]
$B_s \to X\ell\nu$	9.5 ± 2.7	BaBar [5]
$B_s \to D_{s1}(2536)X\mu\nu$; $D_{s1} \to D^*K$	0.25 ± 0.07	D0 [6]
$B_s \to D_{s1}(2536)X\mu\nu$; $D_{s1} \to D^*K$	0.43 ± 0.17	LHCb [7]
$B_s \to D_{s2}(2573)X\mu\nu$; $D_{s2} \to D^0K$	0.26 ± 0.12	LHCb [7]

Table 1.1: Measurements of semileptonic B_s decays before the research carried out in this thesis.

of $\mathrm{SU(3)}_{\mathrm{flavour}}$ symmetry are small. The experimental test of this prediction can provide a confirmation and is an additional cross-check of QCD.

The thesis is organised as follows: It starts with a brief review of the theoretical background of semileptonic B_s decays in Chapter 2. This is followed by a description of the Belle detector (Chapter 3) and the collected data samples (Chapter 4). In Chapter 5, it will be explained how semileptonic B_s decays are reconstructed. The measurements of the "semi-inclusive" $B_s \to D_s^{(*)}X\ell\nu$ and the "inclusive" $B_s \to X\ell\nu$ branching fractions are documented in Chapters 6 and 7, respectively. The results are discussed in Chapter 8 and a brief outlook on future possible measurements of semileptonic B_s decays is given. Finally, the conclusions of this thesis are presented in Chapter 9.

CHAPTER 2

Theoretical framework

The standard model of particle physics describes processes at very small scales, at the size of the proton ($\approx 1\,\mathrm{fm}$) and below. It provides the currently best description of the interactions between the building bricks of matter which are the fermions (spin $\frac{1}{2}$ particles) shown in Fig. 1.1. Spin-1 Bosons exchanged between the fermions describe the electromagnetic, weak and strong interactions observed in nature. An additional spin-0 boson, the Higgs particle, generates the particle masses. The standard model is a quantum field theory with a gauge symmetry described by the gauge group

$$\mathrm{SU}(3)_{\mathrm{colour}} \times \mathrm{SU}(2)_{\mathrm{weak}} \times \mathrm{U}(1)_{Y}\,. \tag{2.1}$$

The group describes transformations in the space of the associated charges: colour, weak isospin and weak hypercharge, respectively. In the following, the relevant concepts for measurements of semileptonic B_s decays are briefly introduced.

Process	Participating fermions	Gauge bosons (Mass)	
Electromagnetic	Electrically charged	γ	(massless)
Charged weak	Left-handed	W^+, W^-	(80 GeV)
Neutral weak	All	Z^0	(91 GeV)

Table 2.1: Processes of the elektroweak interaction.

2.1 Electroweak interaction

The group $\mathrm{SU(2)}_{\mathrm{weak}} \times \mathrm{U(1)}_Y$ represents the electroweak interaction and unites the following processes: the electromagnetic interaction responsible for example for the binding of the electrons to the atomic nucleus, the charged weak interaction modifying the particle flavour and the neutral weak interaction describing for example elastic neutrino scattering. The processes differ in the kind of fermions that participate in them and in the masses of the exchanged gauge bosons, as summarised in Table 2.1.

The gauge bosons A, W^+, W^- and Z^0 observed in nature are not identical to the gauge bosons W^1, W^2, W^3 and B of the symmetry group $\mathrm{SU(2)}_{\mathrm{weak}} \times \mathrm{U(1)}_Y$, but they are a superposition of these states:

$$W^\pm = 1/\sqrt{2}\left(W^1 \pm W^2\right), \tag{2.2}$$

$$Z = -\sin\theta_{\mathrm{W}} B + \cos\theta_{\mathrm{W}} W^3\,, \tag{2.3}$$

$$A = \quad \cos\theta_{\mathrm{W}} B + \sin\theta_{\mathrm{W}} W^3\,. \tag{2.4}$$

Here, θ_{W} denotes the Weinberg angle defined by

$$\tan\theta_{\mathrm{W}} = \frac{g'}{g} \tag{2.5}$$

with the coupling constants g and g' of the weak isospin and the weak hypercharge, respectively. The coupling constant g is usually expressed in the literature by the Fermi constant [8]:

$$G_\mathrm{F} = \frac{\sqrt{2}}{8}\left(\frac{g}{M_W}\right)^2 = 1.1663787(6) \times 10^{-5}\,\mathrm{GeV}^{-2}\,. \tag{2.6}$$

The problem of relating electromagnetic and weak processes via Equations 2.2, 2.3 and 2.4 is that the mediator of the weak interaction, the photon A, is massless, but the gauge bosons of the weak interaction, $W^\pm$ and Z^0, are very massive. This "unnaturalness" can maybe be accepted, but the presence of mass terms for the $W^\pm$ and Z^0 bosons in the standard model Lagrangian breaks the gauge invariance under $\mathrm{SU}(2)_\mathrm{weak} \times \mathrm{U}(1)_Y$ transformations. This problem can be solved using the concept of a spontaneously broken symmetry. For this, the additional Higgs field, Φ, is introduced which is invariant under $\mathrm{SU}(2)_\mathrm{weak} \times \mathrm{U}(1)_Y$ transformations. The symmetry is spontaneously broken if one requires that the vacuum expectation value of the field is different from zero:

$$\langle|\Phi|\rangle = \frac{1}{\sqrt{2}}v\,. \tag{2.7}$$

To generate the masses of the $W^\pm$ and Z^0 bosons, a minimum of two complex scalar fields is necessary,

$$\Phi = \begin{pmatrix} \Phi^+ \\ \Phi^0 \end{pmatrix}. \tag{2.8}$$

The $W^\pm$ and Z^0 masses are related to the vacuum expectation value, v, via

$$M_{W^\pm} = \frac{g}{2}v\,, \qquad M_{Z^0} = \frac{\sqrt{g^2 + g'^2}}{2}v\,. \tag{2.9}$$

The introduction of the Higgs field implies the existence of an additional particle, the Higgs boson. The Large Hadron Collider (LHC) experiments recently found a boson at a mass of $M_H = [125.9 \pm 0.4]$ GeV, which has properties compatible with the long sought-for Higgs boson [8–10].

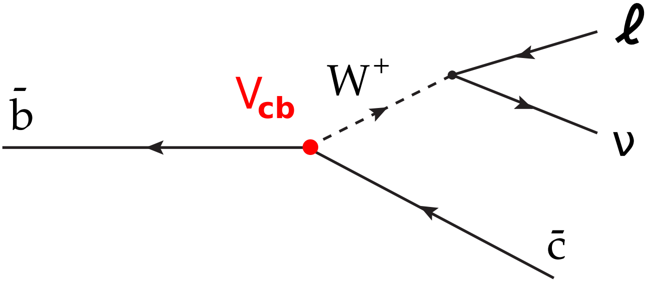

Figure 2.1: Example of quark flavour change through the weak interaction.

The discussion in the following focuses on the charged weak interaction. Processes of the charged weak interaction have the property to maximally violate parity, i.e. only left-handed[1] fermions and right-handed anti-fermions participate in the interaction [11]. This is a strong statement because it refutes the intuitive expectation that the mirror picture of a physical process is always a valid physical process. An example for a charged weak process, a semileptonic decay, is depicted in Fig. 2.1. An anti-beauty quark decays into an anti-charm quark under the emission of a W^+ boson which subsequently decays into a lepton-anti-lepton pair. The transition amplitude of the process is proportional to the $W^\pm$ propagator

$$-i\frac{g_{\mu\nu} - q_\mu q_\nu / M_{W^\pm}^2}{q^2 - M_{W^\pm}^2}\,, \tag{2.10}$$

where q is the four-momentum transferred by the W^+ boson. For values of $|q^2|$ much smaller than $M_{W^\pm}^2$, the propagator can be approximated very well by

$$\frac{g_{\mu\nu}}{M_{W^\pm}^2}\,. \tag{2.11}$$

---

[1] The term "left-handed" refers to an intrinsic property of a particle. For massless particles, left-handedness is equivalent to an anti-parallel orientation of the spin and the flight direction.

The fermion vertices contribute each a factor

$$\frac{-ig}{\sqrt{2}}\bar{v}_L\gamma^\mu u_L \tag{2.12}$$

to the transition amplitude, where γ^μ are the Dirac matrices and $\bar{v}_L$, u_L are the left-handed spinors which form doublets of the weak isospin. In the the case of leptons, the doublets are composed of pairs of the charged and neutral leptons from the same generation,

$$\begin{pmatrix} e \\ \nu_e \end{pmatrix}_{\mathrm{L}}, \begin{pmatrix} \mu \\ \nu_\mu \end{pmatrix}_{\mathrm{L}}, \begin{pmatrix} \tau \\ \nu_\tau \end{pmatrix}_{\mathrm{L}}. \tag{2.13}$$

The "L" signifies that the fermions of the doublet are left-handed. The assignment of same-generation quark pairs to weak isospin doublets,

$$\begin{pmatrix} u \\ d \end{pmatrix}_L, \begin{pmatrix} c \\ s \end{pmatrix}_L, \begin{pmatrix} t \\ b \end{pmatrix}_L, \tag{2.14}$$

is not correct; for example, the $\bar{b} \to \bar{c}$ transition depicted in Fig. 2.1 would be forbidden as the $\bar{b}$ and $\bar{c}$ quarks stem from different generations — the process, however, takes place at a relatively high rate. The reason for this is that the quark mass eigenstates, q, and the quark flavour eigenstates, q', are not identical: a mass eigenstate cannot be identified with one single flavour eigenstate, but contains a mixture of multiple flavours. The relation between mass and flavour eigenstates is given by the CKM matrix, V_{ij}:

$$\begin{pmatrix} d' \\ s' \\ b' \end{pmatrix} = \begin{pmatrix} V_{ud} & V_{us} & V_{ub} \\ V_{cd} & V_{cs} & \boldsymbol{V_{cb}} \\ V_{td} & V_{ts} & V_{tb} \end{pmatrix} \begin{pmatrix} d \\ s \\ b \end{pmatrix}. \tag{2.15}$$

The weak isospin quark doublets are in this formalism given by

$$\begin{pmatrix} u \\ d' \end{pmatrix}_L, \begin{pmatrix} c \\ s' \end{pmatrix}_L, \begin{pmatrix} t \\ b' \end{pmatrix}_L. \tag{2.16}$$

The CKM parameters cannot be derived from first principles, but they are fundamental parameters of the standard model and have to be determined experimentally. The absolute values of the complex CKM matrix elements obtained from a fit to the available measurements are [8]:

$$|V_{ij}| = \begin{pmatrix} 0.974 & 0.225 & 0.004 \\ 0.225 & 0.986 & \mathbf{0.041} \\ 0.008 & 0.040 & 0.999 \end{pmatrix} . \tag{2.17}$$

The magnitudes of the CKM matrix elements describe the coupling strength of the W boson to a particular quark pair, i.e. they modify the weak coupling constant by a factor $|V_{ij}|$ for quarks as compared to leptons. The change of quark flavour evoked by the charged weak interaction happens most likely within the same quark generation, less likely between the first and second, or the second and third generations and very unlikely between the first and the third generations. In the example of Fig. 2.1, the decomposition of the mass eigenstate $\bar{b}$ into flavour eigenstates reads

$$\bar{b} = V^*_{ub}\bar{d}' + V^*_{cb}\bar{s}' + V^*_{tb}\bar{b}' . \tag{2.18}$$

It is the small admixture of size $|V_{cb}|$ of anti-strange flavour, $\bar{s}'$, in the $\bar{b}$ state that makes the observed decay of the $\bar{b}$ quark to a $\bar{c}$ quark possible.

The CKM matrix is unitary which reflects the conservation of probability in weak processes. A complex 3×3 matrix is in general described by $2 \times 3 \times 3 = 18$ real numbers. The unitarity conditions,

$$\sum_{k=d,s,b} V_{ik} V^*_{jk} = \delta_{ij} , \tag{2.19}$$

constrain the number of parameters of the CKM matrix to $3^2 = 9$ real numbers. Each of the 6 external quark fields can absorb one complex phase. However, one global phase remains, so the total number of independent parameters is reduced by $6 - 1 = 5$. In conclusion, the CKM

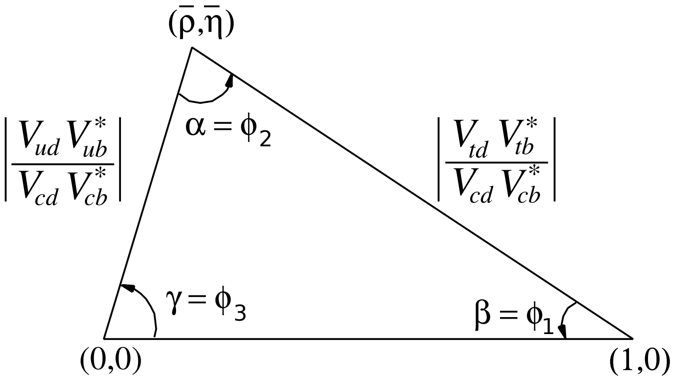

Figure 2.2: The unitarity triangle defined by Eq. 2.22. There are two naming conventions for the angles introduced by the experiments Belle (ϕ_1, ϕ_2, ϕ_3) and BaBar (α, β, γ). Figure taken from Ref. [8].

matrix is described by $9 - 5 = 4$ real numbers. A common representation uses three "rotation angles" $\theta_{12}, \theta_{23}, \theta_{13}$ and one phase factor δ:

$$\begin{pmatrix} c_{12}c_{13} & s_{12}c_{13} & s_{13}e^{-i\delta_{13}} \\ -s_{12}c_{23} - c_{12}s_{23}s_{13}e^{i\delta_{13}} & c_{12}c_{23} - s_{12}s_{23}s_{13}e^{i\delta_{13}} & s_{23}c_{13} \\ s_{12}s_{23} - c_{12}c_{23}s_{13}e^{i\delta_{13}} & -c_{12}s_{23} - s_{12}c_{23}s_{13}e^{i\delta_{13}} & c_{23}c_{13} \end{pmatrix}, \qquad (2.20)$$

where c_{ij} and s_{ij} stand for $\cos\theta_{ij}$ and $\sin\theta_{ij}$, respectively. The phase factor δ determines the amount of *CP* violation in the standard model. One of the unitarity conditions from Eq. 2.19 is:

$$V_{ud}V_{ub}^* + V_{cd}V_{cb}^* + V_{td}V_{tb}^* = 0\,. \qquad (2.21)$$

This condition can be represented as the triangle depicted in Fig. 2.2, where the point $(\bar{\rho}, \bar{\eta})$ is given by

$$\bar{\rho} + i\bar{\eta} = -\frac{V_{ud}V_{ub}^*}{V_{cd}V_{cb}^*}\,. \qquad (2.22)$$

The sides and the angles of the triangle can be constrained experi-

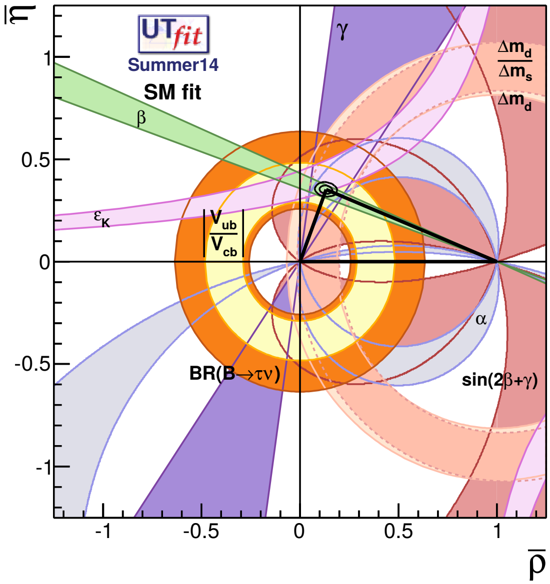

Figure 2.3: Constraints on the unitarity triangle from different measurements and the fit result obtained by the UTfit collaboration [12]. A similar fit is performed by the CKMfitter collaboration [13].

mentally, for example by measurements of the semileptonic B decays ($|V_{ub}/V_{cb}|$), measurements of $B_{(s)}$ meson mixing (Δm_d, Δm_s) or the measurement of the direct CP violation of the kaon system (ϵ_K). Figure 2.3 shows the result of a fit to the available measurements and demonstrates that they are compatible with the unitarity of the CKM matrix.

One implication of the CKM mechanism is that $B_s = \bar{b}s$ and $B^0 = \bar{b}d$ mesons can "oscillate" into their anti-particles, $\bar{B}_s = b\bar{s}$ and $\bar{B}^0 = b\bar{d}$, respectively, via the box diagrams depicted in Fig. 2.4. In the following, the mixing of B_s mesons is discussed; the reasoning is analogous for

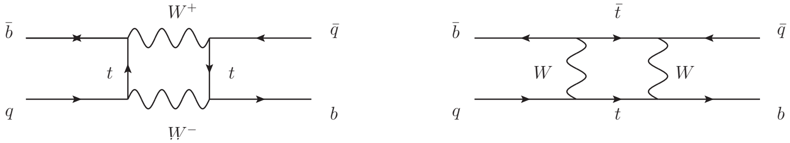

Figure 2.4: The leading order diagrams for B_q ($q = d, s$) mixing.

B mesons. The heavy and light mass eigenstates, $B_{s,\mathrm{H}}$ and $B_{s,\mathrm{L}}$, are a mixture of the flavour eigenstates B_s and $\bar{B}_s$:

$$|B_{s,\mathrm{L/H}}\rangle = p|B_s\rangle \pm q|\bar{B}_s\rangle\,, \tag{2.23}$$

where p and q are complex numbers. The time evolution of a flavour eigenstate $|B_s\rangle$ can be written as [8]:

$$|B_s(t)\rangle = g_+(t)|B_s\rangle + \frac{q}{p}g_-(t)|\bar{B}_s\rangle\,. \tag{2.24}$$

The time-dependent oscillation probability is given by[2]

$$|g_\pm(t)|^2 = e^{-\Gamma t/2}\left[1 \pm \cos\left(\frac{\Delta m}{\Gamma}\Gamma t\right)\right]\,, \tag{2.25}$$

where Γ is the average width of the heavy and light mass eigenstates and Δm is the mass difference between the two states. The small difference of the width, $\Delta\Gamma = \Gamma_L - \Gamma_H$ between the heavy and the light state can be neglected. At Belle, B_s mesons are produced in $B_s^{(*)}\bar{B}_s^{(*)}$ pairs which are coherent $C = \pm 1$ states, where C are the eigenvalues of the charge conjugation operator. Therefore the expression for the $B_s^{(*)}\bar{B}_s^{(*)}$ state needs to be symmetrised:

$$|B_s(t_1)\bar{B}_s(t_2)\rangle = \frac{1}{\sqrt{2}}\left(|B_s(t_1)\rangle \otimes |\bar{B}_s(t_2)\rangle + C|\bar{B}_s(t_1)\rangle \otimes |B_s(t_2)\rangle\right)\,. \tag{2.26}$$

---

[2] This assumes $|q/p| = 1$, i.e. the absence of CP violation in mixing, which is confirmed by measurements (within the experimental uncertainties) [8].

From this, one can derive the time integrated mixing probability, i.e. the probability that the two B_s mesons decay with the same flavour [14]:

$$\chi_s^{(C)} = \frac{x_s^2(x_s^2 + 2 + C)}{2(1 + x_s^2)^2}\,, \tag{2.27}$$

which depends only on the quantity $x_s = \Delta m/\Gamma = 26.85 \pm 0.13$ [8]. The mixing parameter is different for B^0 mesons: $x_d = 0.774 \pm 0.008$ [8]. For B_s mesons, the parameter x is so large that $\chi^{(-)} \approx \chi^{(+)} \approx 50\,\%$. For B^0 mesons, different mixing probabilities are obtained depending on the C eigenstate of the $B^0\bar{B}^0$ pair: $\chi_d^{(-)} = 18.7\,\%$ and $\chi_d^{(+)} = 42.2\,\%$.

2.2 Strong interaction

Quarks and anti-quarks are held together in mesons ($q\bar{q}$) and baryons (qqq) by the strong interaction. The theory of the strong interaction is QCD with the (non-abelian) symmetry group $\mathrm{SU}(3)_{\mathrm{colour}}$. The quarks carry a colour charge, “red”, “green” or “blue”; the anti-quarks one of the respective anti-colours. The exchange particles of the strong interaction, the massless gluons, carry themselves colour charges and thus couple to each other. The self-coupling of the gluons induces an anti-screening effect making the coupling at large distances, i.e. small momentum transfers, q^2, very large. This leads to the “confinement” of the quarks in hadrons. The confinement provides an explanation why so far no coloured objects have been observed in nature. At small distances, i.e. high momentum transfers, q^2, the effective coupling constant becomes negligible and the quarks can be described as free particles, a phenomenon which is referred to as “asymptotic freedom”. The effective strong coupling constant is given by:

$$\alpha_{\mathrm{S}}(q^2) = \frac{12\pi}{(33 - 2n_f)\ln\left(\frac{q^2}{\Lambda_{\mathrm{QCD}}^2}\right)}\,, \tag{2.28}$$

where n_f is the number of quark flavours, q is the momentum transferred in the interaction and Λ_{QCD} is defined by the typical length scale of a hadron,

$$\frac{1}{\Lambda_{\text{QCD}}} \approx \frac{1}{200\,\text{MeV}} \approx 1\,\text{fm}\,. \tag{2.29}$$

The condition $q^2 \gg \Lambda_{\text{QCD}}$ defines the regime, where the strong coupling constant is small enough that the quark dynamics can be calculated perturbatively, i.e. as an expansion in powers of α_{s}.

The strong interaction is insensitive to the flavour of the quarks. Therefore, processes of the strong interaction are in principle invariant under the exchange of the quark flavour. This symmetry is, however, not as fundamental as the gauge symmetries and in fact it is broken due to the different masses of the quarks. The scale Λ_{QCD} divides the six quark species into light quarks ($q = u, d, s$) and heavy quarks ($Q = c, b, t$):

$$m_q < \Lambda_{\text{QCD}} < m_Q\,. \tag{2.30}$$

The symmetry of the light quarks is described by the group $\text{SU}(3)_{\text{flavour}}$. Therefore, the pseudo-scalar mesons can be arranged graphically in an octet and a singlet according to the value of the third component of the strong isospin, I_z, and the strangeness quantum number, S, as depicted in Fig. 2.5 (a). The breaking of $\text{SU}(3)_{\text{flavour}}$ symmetry manifests itself in the different meson masses due to the different masses of the constituent quarks. Neglecting the categorisation into light and heavy quarks, the diagram can be extended by adding additional dimensions for the charm and beauty quantum numbers, C and B. Figure 2.5 (b) illustrates this for the quantum number B. Although this extension does not make sense along the B axis, the $\text{SU}(3)_{\text{flavour}}$ symmetry within the $B = \pm 1$ planes is a good approximation and this will become important later in the discussion of semileptonic $B_{(s)}$ decays.

The $B_{(s)}$ mesons as well as the $D_{(s)} = \bar{c}q$ ($q = u, d, s$) mesons are so-called heavy-light states because they are composed of a heavy and a light quark. The large masses of the heavy quark, m_Q, implies that the associated Compton wavelength, $\lambda_Q \sim 1/m_Q$, is small compared to $1/\Lambda_{\text{QCD}}$ and therefore, relativistic effects such as colour magnetism in bound states become small [15]. Such relativistic effects are solely responsible for the coupling of the heavy quark spin to the rest of the strongly interacting system. In the approximation of infinite heavy quark mass, the spins entirely decouple [15] and therefore the meson wave function can be factorised:

$$|D_s, s_c, s_s\rangle \approx |c, s_c\rangle |s, s_s\rangle \,, \tag{2.31}$$

where s_c and s_s are the spins of the c and s quark, respectively. An experimental hint of the decoupling of the heavy-quark spin is the small mass splitting between the $c\bar{s}$ states D_s (spin 0) and D_s^* (spin 1) [15],

$$m_{D_s^*} - m_{D_s} = 144\,\mathrm{MeV}\,, \tag{2.32}$$

compared to the large mass splitting of the $u\bar{d}$ states π (spin 0) and ρ (spin 1),

$$m_\rho - m_\pi = 635\,\mathrm{MeV}\,. \tag{2.33}$$

The decoupling of the quark spins corresponds to a new symmetry, the heavy quark symmetry.

In addition to the D_s^* excitation, there are also higher excitations of the D_s meson. The most important are: $D_{s0}^*(2317)$, $D_{s1(2536)}$, $D_{s1}'(2460)$ and $D_{s2}^*(2573)$. In this thesis, they are denoted by "D_s^{**}". Figure 2.6 shows an overview of the D_s mass spectrum.

2.3 Semileptonic decays

The process depicted in Fig. 2.1 where the virtual W boson decays to a lepton pair, $\ell^+\nu$, are ideal to extract the magnitude of the CKM matrix element V_{cb}, because the decay matrix element factorises into a leptonic and a hadronic component (neglecting higher-order electroweak corrections). The replacement of the $\ell^+\nu$ pair in the final state with an anti-quark-quark pair, $\bar{q}q$, would, in contrast, involve additional QCD effects causing unnecessary complications in the $|V_{cb}|$ extraction. However, even the process $\bar{b} \to \bar{c}\ell\nu$ cannot be observed in a "QCD-free" environment because the $\bar{b}$ and $\bar{c}$ quarks are bound in hadrons due to the confinement. In the decays investigated in this thesis, the b quark is contained in a $B_s = \bar{b}s$ meson and consequently in most cases there

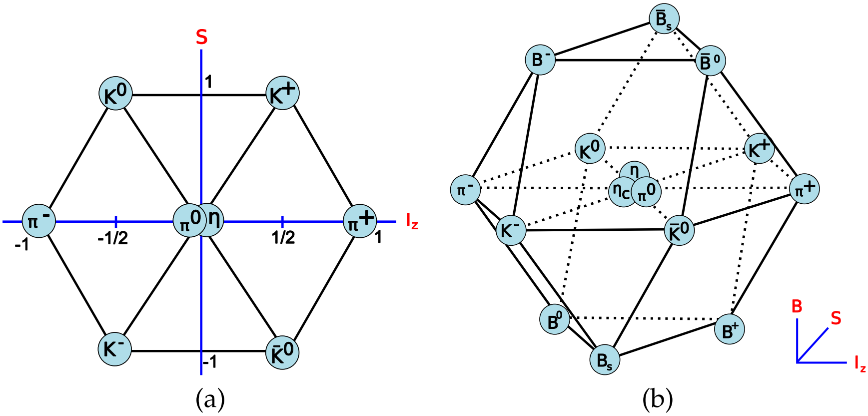

Figure 2.5: Arrangement of pseudoscalar mesons in geometrical structures. (a) Two-dimensional representation of the light spin 0 mesons (“eightfold way”). The blue axes are the z-component of the isospin, I_z and the strangeness, S. (b): Extended version with “beauty”, B, as third dimension. Figures adapted from material available in the public domain.

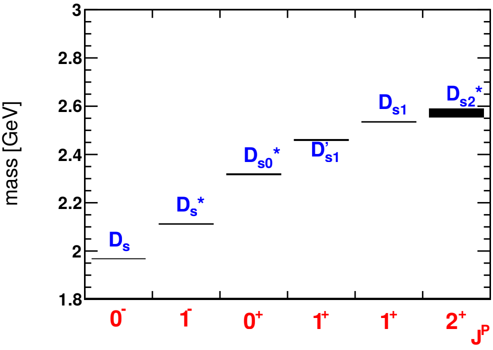

Figure 2.6: D_s meson mass spectrum. The centre of the grey rectangles represents the mass of the state and the height corresponds to twice the width.

is a $D_s = \bar{c}s$ meson in the final state. Figure 2.7 shows the Feynman diagram of this process. Although the light s quark is only a spectator of the weak process, the heavy b and c quarks "feel" their light partner via the strong interaction.

There are two ways of studying semileptonic $B_{(s)}$ decays and determining $|V_{cb}|$. The first way is the exclusive approach, where a specific hadron in the final state is reconstructed. The second way is the inclusive approach, where the hadron in the final state is not explicitly reconstructed and rather the sum of all possible hadrons in the final state is studied. The two approaches are complementary in the sense that different experimental techniques and theoretical descriptions are used.

2.4 Exclusive semileptonic decays

The extraction of $|V_{cb}|$ from exclusive measurements of semileptonic $B_{(s)}$ decays requires the knowledge of form factors describing the influence of QCD effects in the transition matrix elements. The form factors also are necessary ingredients for the modelling of the signal kinematic distributions in the measurement. The form factors, h_i, depend on the "recoil" energy, $\tilde{E}_{D_{(s)}}$[3], of the final state hadron with mass $m_{D_{(s)}}$. Usually, they are expressed as a function of

$$w = v \cdot v' = \frac{\tilde{E}_{D_{(s)}}}{m_{D_{(s)}}}, \tag{2.34}$$

where v and v' are the B_s and $D_s^{(*)}$ four-velocities. The parameter w can also be expressed in terms of the four-momentum, q, transferred to the lepton-neutrino pair in the semileptonic decay:

$$w = \frac{m_{B_s} + m_{D_s^{(*)}} - q^2}{2 \cdot m_{B_s} \cdot m_{D_s^{(*)}}}. \tag{2.35}$$

---

[3] The "~" symbol signifies that the quantity is calculated in the rest frame of the $B_{(s)}$ meson.

In the following, the $B_s \to D_s^{(*)} \ell \nu$ form factors are given in a notation especially tailored to facilitate their interpretation. For this, the weak current $j^\mu = \bar{u}\gamma^\mu(1-\gamma^5)u$ is introduced in Eq. 2.12 with the vector component $j_V^\mu = \bar{u}\gamma^\mu u$ and the axial component $j_A^\mu = \bar{u}\gamma^\mu\gamma^5 u$. For the decay mode with the pseudoscalar D_s meson in the final state, only the vector component contributes,

$$\frac{\langle D_s(v')|\bar{c}\gamma^\mu b|B_s(v)\rangle}{\sqrt{m_{D_s} m_{B_s}}} = h_+(w)(v+v') + h_-(w)(v-v')^\mu \,, \tag{2.36}$$

while for the mode with the vector D_s^* meson, both the vector and the axial components contribute [16]:

$$\frac{\langle D_s^*(v',\epsilon)|\bar{c}\gamma^\mu b|B_s(v)\rangle}{\sqrt{m_{D_s^*} m_{B_s}}} = i h_V \epsilon^{\mu\alpha\beta\gamma} \epsilon^*_\alpha v'_\beta v_\gamma \,, \tag{2.37}$$

$$\frac{\langle D_s^*(v',\epsilon)|\bar{c}\gamma^\mu\gamma_5 b|B_s(v)\rangle}{\sqrt{m_{D_s^*} m_{B_s}}} = h_{A_1}(w)(w+1)\epsilon^{*\mu} - \Big[h_{A_2}(w)v^\mu + \tag{2.38}$$

$$h_{A_3}(w)v'^\mu)(\epsilon^* \cdot v\Big] \,, \tag{2.39}$$

where ϵ^μ is the polarisation vector of the D_s^* meson and $\epsilon^{\mu\alpha\beta\gamma}$ is the Levi-Civita symbol. Defining $r^{(*)} = m_{D_s^{(*)}}/m_{B_s}$, the differential decay rates read

$$\frac{\mathrm{d}\Gamma}{\mathrm{d}w}(B_s \to D_s \ell \nu) = \frac{G_F^2 |V_{cb}|^2 m_{B_s}^5}{48\pi^3} (w^2-1)^{3/2} r^3 (1+r)^2 |\eta_{\mathrm{EW}} V_1(w)|^2 \,, \tag{2.40}$$

with

$$V_1(w) = h_+ + \left(\frac{1-r}{1+r}\right) h_- \,, \tag{2.41}$$

and

$$\frac{\mathrm{d}\Gamma}{\mathrm{d}w}(B_s \to D_s^*\ell\nu) = \frac{G_F^2|V_{cb}|^2 m_{B_s}^5}{48\pi^3}(w^2-1)^{1/2}(w+1)^2 r^{*3}(1-r^*)^2 \times \\ \left[1 + \frac{4w}{w+1}\frac{1-2wr^*+r^{*2}}{(1-r^*)^2}\right]|\eta_{\mathrm{EW}}\mathcal{F}(w)|^2\,, \tag{2.42}$$

with

$$\mathcal{F}(w)^2 = \left[2(1-2wr^*+r^{*2})\left(h_{A_1}^2 + \left(\frac{w-1}{w+1}\right)h_V^2\right) + \Big((1-r^*)h_{A_1} + \\ (w-1)(h_{A_1} - h_{A_3} - r^* h_{A_2})\Big)^2\right] \times \Big[(1-r^*)^2 + \\ \frac{4w}{w+1}(1-2wr^*+r^{*2})\Big]^{-1}\,. \tag{2.43}$$

The factor

$$\eta_{\mathrm{EW}} = 1.007 \tag{2.44}$$

corrects for small effects of the electroweak interaction, e.g. photons radiated of the charged lepton. Equation 2.40 describes the full kinematics of $B_s \to D_s\ell\nu$ decays, while the differential decay width of $B_s \to D_s^*\ell\nu$ decays also has a non-trivial dependence on the angles between the decay products which have been integrated out in Eq. 2.42. These angles which are also shown in Fig. 2.8 are defined as follows:

- θ_ℓ — the angle defined between the direction of the lepton in the virtual W rest frame and the direction of the W in the B_s rest frame. This angle is of particular importance, because it is directly linked to the final state lepton momentum distribution, which will be used in the analyses for the signal extraction.

- θ_V — the polar angle in the rest frame of the D_s^* meson between the momentum of the D_s meson from the D_s^* decay and the direction opposite to the W boson.

- χ — the angle between the plane defined by the decay of the D_s^* meson and the plane defined by the decay of the W boson.

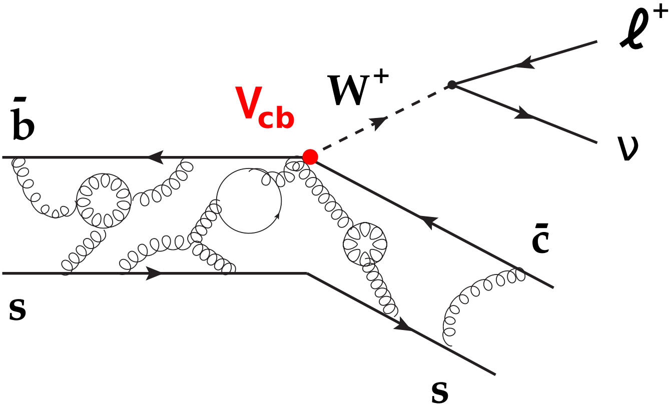

Figure 2.7: Feynman diagram of the decay $B_s \to D_s \ell \nu$. The curly lines illustrate the gluon exchange between the heavy (b, c) and the light (s) quark. The gluon lines are only an example how the interaction between the quarks could look like.

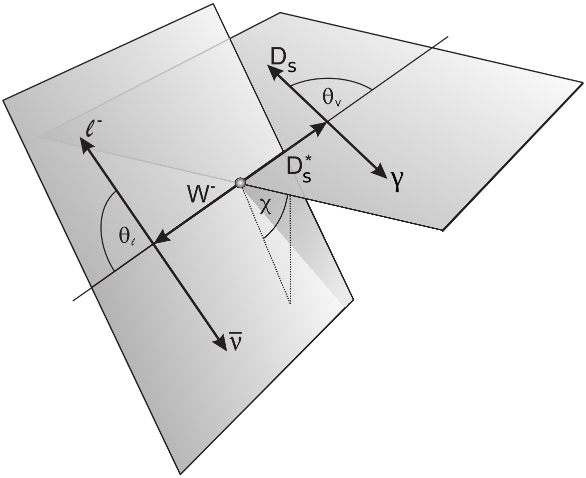

Figure 2.8: Angles defined between the decay products of the $B_s \to D_s^* \ell \nu$ decays. Adapted from Ref. [17].

2.4.1 Interpretation of the form factors in the limit of infinite heavy quark masses

The differential decay rates and form factors presented above are given in a generic, model-independent way. In order to extract $|V_{cb}|$ from the measured decay rates it is necessary to determine the numeric values of the form factors and their dependence on the recoil w. For this, one starts with the approximation that the mass of the heavy b and c quarks is infinite. The remaining content of the meson, consisting of the light anti-quark, the gluons and light $q\bar{q}$ pairs, is subsumed under the term "light degrees of freedom". The approximation of infinite heavy quark masses, m_b and m_c, makes only sense if the momentum transfer to the light degrees of freedom, q^2_{light}, is small in comparison. This is the case because the light degrees of freedom move with the velocities of the mesons, v and v', from which the order of magnitude of q^2_{light} can be estimated by [16]:

$$q^2_{\text{light}} = (p_{\text{light}} - p'_{\text{light}})^2 = (\Lambda_{\text{QCD}}v - \Lambda_{\text{QCD}}v')^2 = 2\Lambda^2_{\text{QCD}}(1-w) \leq m_{b,c}\,. \tag{2.45}$$

In the heavy-quark limit, $m_Q \to \infty$, the meson wave functions factorise (cf. Eq. 2.31) and the transition matrix of a semileptonic B_s decay can be written as

$$\langle D_s, s'_c, s'_s, v'|\bar{c}\Gamma b|B_s, s_b, s_s, v\rangle \approx \langle cs'_c v'|\bar{c}\Gamma b|b, s_b v\rangle\langle s, s'_s, v'|s, s_s, v\rangle \tag{2.46}$$

$$\approx \langle cs'_c v'|\bar{c}\Gamma b|b, s_b v\rangle \xi_{s'_s s_s}(w)\,, \tag{2.47}$$

where the notation $j^\mu = \bar{c}\Gamma b$ was introduced for the weak current [15]. The transition matrices are all proportional to one identical function, $\xi(w)$, the so-called Isgur-Wise function describing the nonperturbative dynamics of the light degrees of freedom. Applying this result to the form factors defined in Eq. 2.36 to 2.39 one obtains

$$\langle D_s(v')|\bar{c}\gamma^\mu b|B_s(v)\rangle = \xi(w)(v_\mu + v'_\mu)\,, \tag{2.48}$$

$$\langle D^*_s(v', \epsilon)|\bar{c}\gamma^\mu b|B_s(v)\rangle = \xi(w)\epsilon^{\mu\alpha\beta\gamma}\epsilon^*_\alpha v'_\beta v_\gamma\,, \tag{2.49}$$

$$\langle D^*_s(v', \epsilon)|\bar{c}\gamma^\mu\gamma_5 b|B_s(v)\rangle = -i\xi(w)((w+1)\epsilon^{*\mu} - (\epsilon^* \cdot v)v'_\mu)\,, \tag{2.50}$$

from which follows

$$\begin{gathered} h_+(w) = h_V(w) = h_{A_1}(w) = h_{A_3}(w) = \xi(w)\,, \\ h_-(w) = h_{A_2}(w) = 0\,. \end{gathered} \tag{2.51}$$

At the zero recoil point, $w = 1$, the velocity of the meson does not change ($v = v'$) and therefore the overlap is maximal between the wave functions describing the light degrees of freedom in the initial and final state. From the normalisation condition of the wave function follows

$$\xi(1) = 1\,. \tag{2.52}$$

This point represents the ideal conditions for the determination of $|V_{cb}|$ because the influence of QCD effects becomes minimal. A precise $|V_{cb}|$ extraction from a measured decay rate in this region requires, however, a more realistic estimation of the form factors taking into account the finite heavy-quark masses and the impact of hard gluon radiation [2]. Moreover, it is experimentally not feasible to measure the decay rate exactly at zero recoil. The differential decay rate has to be measured for multiple intervals $w > 1$ and then the value at $w = 1$ has to be extrapolated. The theoretical precision of the $|V_{cb}|$ measurement depends thus also on the accuracy of the functional shape of the $\mathrm{d}\Gamma/\mathrm{d}w$ distribution used for the extrapolation. Currently, the most precise predictions are obtained numerically from Lattice QCD where the nonperturbative QCD processes are calculated on a discrete Euclidean space-time grid [18]. Recently, first Lattice QCD calculations were published for $B_s \to D_s \ell \nu$ decays [19, 20]. The drawback of the Lattice QCD technique is that it can predict the form factors only in the region near $w = 1$. Many measurements require the knowledge of the full w dependence of the form factors in order to correctly model the kinematic distributions that allow to estimate the rates of signal and background processes. In the following, two approaches to obtain this information are discussed: QCD sum rules and quark models. The calculations by Fan et. al performed in the framework of "perturbative QCD" [21, 22] are omitted, since their model is already disproved by measurements of $B \to D^{(*)} \ell \nu$ decays [23].

2.4.2 QCD sum rules

In the QCD sum rules approach, perturbation theory is applied in the allowed kinematic range and subsequently, an extrapolation to the non-perturbative region via cleverly chosen correlation functions is performed. This extrapolation is based on the unitarity and analyticity condition [2]. Dedicated calculations for semileptonic B_s decays were carried out in this technique by Li et al. [24], Azizi et al. [25, 26] and Blasi et al. [27]. In the latter reference, $\mathrm{SU(3)}_{\mathrm{flavour}}$ symmetry breaking effects between the form factors for B and B_s decays are estimated to be at the order of 10 %.

A nowadays widely used form factor parametrisation for B decays was introduced by Caprini, Lellouch and Neubert (CLN) [28]. It is inspired by QCD sum-rules and uses the variable transformation,

$$z(w) = \frac{\sqrt{w+1} - \sqrt{2}}{\sqrt{w+1} + \sqrt{2}}, \tag{2.53}$$

that maps each point w to a point inside the unit disc $|z| < 1$. The following expansion of the $B \to D\ell\nu$ form factor is derived:

$$V_1(w) = V_1(1)[1 - 8\rho_D^2 z + (51\rho_D^2 - 10)z^2 - (252\rho_D^2 - 84)z^3]\,. \tag{2.54}$$

The $B \to D^*\ell\nu$ form factor,

$$h_{A_1}(w) = \frac{2r^*}{w+1} A_1(w)\,, \tag{2.55}$$

is described in the CLN parametrisation by the function

$$A_1(w) = A_1(1)[1 - 8\rho^2 z + (53\rho^2 - 15)z^2 - (231\rho^2 - 91)z^3]\,. \tag{2.56}$$

The w dependence of the other $B \to D^*\ell\nu$ form factors is given relative to h_{A_1} by the two ratios:

$$R_1(w) = \frac{h_V(w)}{h_{A_1}(w)} = R_1(1) - 0.12(w-1) + 0.05(w-1)^2\,, \tag{2.57}$$

$$R_2(w) = \frac{h_{A_3}(w) + r^* h_{A_2}(w)}{h_{A_1}(w)} = R_2(1) + 0.11(w-1) - 0.06(w-1)^2 \,. \tag{2.58}$$

The parameters ρ_D, ρ, $R_1(1)$ and $R_2(1)$ were determined from measurements of semileptonic B decays (see below). Motivated by the small amount of $\mathrm{SU(3)}_{\mathrm{flavour}}$ symmetry breaking predicted by Blasi et al. [27], the CLN parametrisation with the parameters from B decays is used in this thesis to model semileptonic B_s decays.

2.4.3 Quark models

In quark models, an assumption is made about the quark anti-quark potential in the B_s and D_s mesons. An ansatz for the meson wave functions is then inserted in the Schrödinger equation which is solved numerically. The parameters of the model are tuned in such a way that the measured meson mass spectra are reproduced. The weak point of quark models is that the assumed quark potentials are arbitrary in the sense that they cannot be obtained from first principles. Due to the unclear connection to QCD, the systematic uncertainties of the model cannot be reliably estimated [2]. Nevertheless, a large number of quark model predictions for semileptonic B_s decays have been published. They comprise calculations in the relativistic constituent quark model [29], the non-relativistic constituent quark model [30–32], Bethe-Salpeter techniques[33] and the light front quark model [34]. Widely used for the simulation of semileptonic decays in particle physics experiments, is also the ISGW2 quark model. It is based on the "mock-mesons" method by Isgur and Wise [35] which makes the unphysical assumption that the masses of the light u, d, s quarks are larger than Λ_{QCD}, so that B_s and D_s mesons can be treated similar to the quarkonium-states $b\bar{b}$ and $c\bar{c}$, respectively. The results obtained with this assumption are extrapolated to the physical region of interest. Later, Scora and Isgur incorporated constraints from heavy-quark symmetry and relativistic corrections into the model [36].

Figure 2.9 shows a comparison of $B_s \to D_s^{(*)} \ell \nu$ branching fractions predicted by quark models and QCD sum rules. They do not only differ in the central values, but also in the size of the assigned uncertainties.

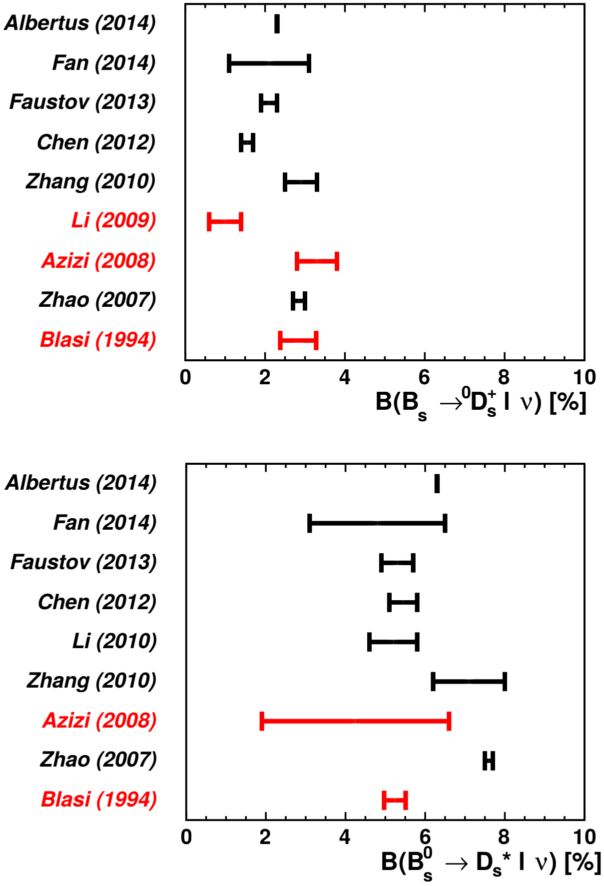

Figure 2.9: Theory predictions for the $B_s \to D_s^{(*)}\ell\nu$ branching fractions. Predictions with QCD sum rules are shown in red. Albertus [30] does not quote uncertainties. The range predicted by Azizi et al. [26] for $B_s \to D_s^*\ell\nu$ includes also the case $\ell = \tau$. NB: The value of $|V_{cb}|$ used in the individual predictions is not always identical.

In Fig. 2.10, the q^2 spectra of $B_s \to D_s^{(*)}\ell\nu$ decays predicted by some of the quark models and the sum rule prediction by Li et al. [24] are compared to each other. They all describe a similiar functional shape which is of course not a validation of the calculations, but an important consistency check. The model by Fan et al. [21], which is already ruled out by studies of $B \to D^*\ell\nu$ decays, is plotted for reference and diverges significantly. The q^2 spectra from the dedicated calculations for semileptonic B_s decays are also compared to the prediction of the CLN parametrisation using the parameters ρ_D and ρ, $R1$, $R2$ obtained from measurements of $B \to D^{(*)}\ell\nu$ decays (see below). Each parameter is varied by ±10 % which corresponds to the level of $\mathrm{SU(3)_{flavour}}$ symmetry breaking estimated in Ref. [27]. The resulting uncertainty band is in agreement with the other predictions which justifies the choice of the CLN parametrisation with the assigned 10 % uncertainty for the modelling of $B_s \to D_s^{(*)}\ell\nu$ decays.

Modes with D_s^{**} mesons in the final state are less attractive for the determination of $|V_{cb}|$ for several reasons. As the spectrum and the nature of the D_s^{**} mesons is theoretically not yet understood, it is challenging to provide a sensible description of the QCD effects in the $B_s \to D_s^{**}$ transition. Recent predictions for the D_s^{**} decay modes can be found in Refs. [24, 29–32, 37]. A summary of the predicted branching fraction is presented in Table 2.2. The fact that the expected branching fractions are one order of magnitude lower than in the case of $B_s \to D_s^{(*)}\ell\nu$ also represents a disadvantage on the experimental side because this means smaller signal yields. The $B_s \to D_s^{**}\ell\nu$ decays are, however, a non-negligible contribution in the semi-inclusive $B_s \to D_s^{(*)}X\ell\nu$ and inclusive $B_s \to X\ell\nu$ measurements presented later. In the semi-inclusive analysis the model from Leibovich-Ligeti-Stewart-Wise (LLSW) [38] originally developed for $B \to D^{**}\ell\nu$ decays is used. For the inclusive measurements, the ISGW2 model is used. These choices are somewhat arbitrary and reflect the current ignorance of semileptonic $B_{(s)}$ decays to the orbitally excited D_s^{**} mesons.

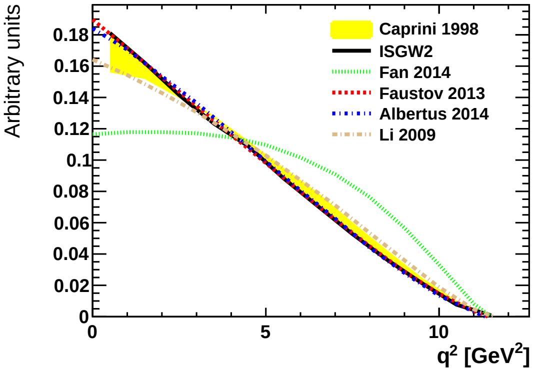

(a) $B_s \to D_s \ell \nu$

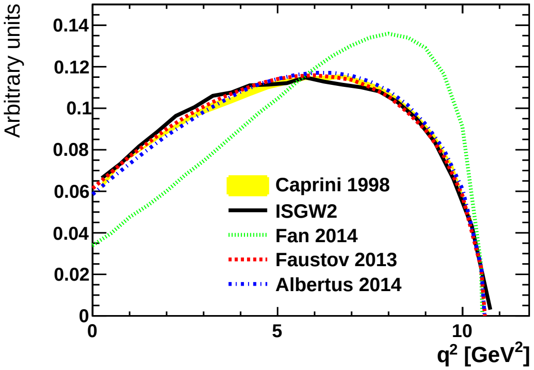

(b) $B_s \to D_s^* \ell \nu$

Figure 2.10: Comparison of the q^2 spectra of $B_s \to D_s^{(*)} \ell \nu$ decays predicted by the ISGW2 model [35, 36] and other quark models (Faustov [29], Albertus [30]) as well as QCD sum rules (Li [24]). The normalisation is chosen such that the integral under the curve equals unity in order to be independent of the $|V_{cb}|$ value chosen in the individual calculations. The yellow band represents the prediction from the CLN parametrisation [28] using the model parameters determined from measurements of $B \to D^{(*)} \ell \nu$ decays and assigning a 10% uncertainty due to SU(3)$_{\text{flavour}}$ breaking effects. The spectrum obtained by Fan et al. [21] with perturbative QCD is plotted as reference to demonstrate the disagreement with the other models.

Ref.	Branching fraction [%]			
	$D_{s0}^{*}\ell\nu$	$D_{s1}(2536)\ell\nu$	$D_{s1}(2460)'\ell\nu$	$D_{s2}^{*}\ell\nu$
[24]	0.23	—	—	—
[29]	0.36 ± 0.04	0.84 ± 0.09	0.19 ± 0.02	0.67 ± 0.07
[30]	0.39	0.32	0.47	0.44
[31]	0.443	0.477	$0.174 \ldots 0.570$	0.376
[32]	$0.490 \ldots 0.571$	—	$0.752 \ldots 0.869$	—
[37]	0.20	—	0.10	—

Table 2.2: Branching fraction predictions for $B_s \to D_s^{**}\ell\nu$ decays.

2.4.4 Determination of $|\mathbf{V_{cb}}|$ from exclusive semileptonic *B* decays

Measurements of $B \to D\ell\nu$ and $B \to D^*\ell\nu$ decays were performed at different experiments to extract the CKM matrix element $|V_{cb}|$ [2].

In the $B \to D\ell\nu$ analyses, the theoretical prediction for the differential decay rate, $\mathrm{d}\Gamma/\mathrm{d}w$, using the CLN form factor parametrisation was fitted to the measured data distribution. The floating parameters in the fit were the CLN parameter ρ_D^2 and the product $\eta_{\mathrm{EW}} \cdot V_1(1) \cdot |V_{cb}|$. The limiting factor for the precision of the measurements is the suppression of the decay rate at small w which goes with the third power of the D momentum. The world average for ρ_D^2 is [39]:

$$\rho_D^2 = 1.19 \pm 0.06 \,. \tag{2.59}$$

The analyses of the $B \to D^*\ell\nu$ decay investigated besides the w distribution also the $\cos\theta_\ell$, $\cos\theta_V$ and χ distributions. The value of the product $\eta_{\mathrm{EW}} \cdot \mathcal{F}(1) \cdot |V_{cb}|$ and the CLN parameters ρ^2, $R_1(1)$ and $R_2(1)$ were extracted from a fit to the measured spectra. An example of such fit is depicted in Fig. 2.11. The current world averages of the extracted

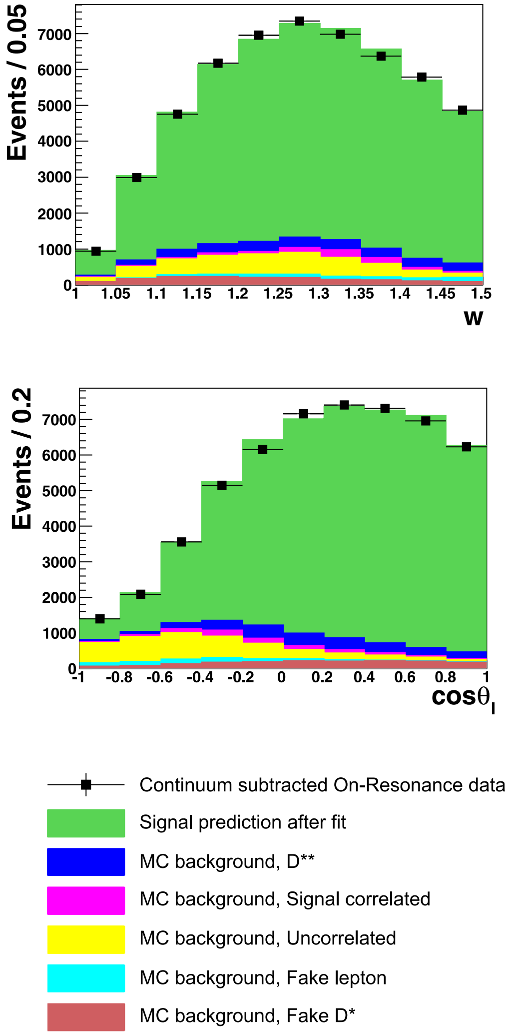

Figure 2.11: Extraction of the CLN parameters from a sample of reconstructed $B^0 \to D^*\ell\nu$ decays in $\Upsilon(4S)$ data [40]. The black points show the distributions measured in data. The superimposed histograms are the MC predictions of the signal and background contributions, where the shape of the signal was varied based on the parameters ρ, $R_1(1)$ and $R_2(1)$. Additionally to the shown w and $\cos\theta_\ell$ distribution also the $\cos\theta_V$ and χ distributions were considered in the fit.

CLN parameters are [39],

$$\rho^2 = 1.21 \pm 0.03\,, \tag{2.60}$$

$$R_1(1) = 1.41 \pm 0.03\,, \tag{2.61}$$

$$R_2(1) = 0.85 \pm 0.02\,. \tag{2.62}$$

The CKM matrix element $|V_{cb}|$ can be extracted from the measured products $\eta_{\mathrm{EW}} \cdot V_1(1) \cdot |V_{cb}|$ and $\eta_{\mathrm{EW}} \cdot \mathcal{F}(1) \cdot |V_{cb}|$ using the electroweak correction (see Eq. 2.44) and the form factors, $V_1(1)$ and $\mathcal{F}(1)$ at zero recoil, $w = 1$. The form factors are usually determined by lattice QCD calculations. The world average of the exclusive measurements is [8]:

$$|V_{cb}| = (39.5 \pm 0.8) \times 10^{-3}\,. \tag{2.63}$$

2.5 Inclusive semileptonic decays

The theory description of the inclusive semileptonic $B_{(s)}$ decay width relies on the principle of heavy quark symmetry introduced above. To take into account the interaction of the heavy b quark with the surrounding cloud of gluons and quark-antiquark pairs (cf. Fig. 2.7), an expansion in powers of $1/m_b$ is performed based on the Operator Product Expansion (OPE) technique, providing the correct treatment of perturbative and non-perturbative contributions. The explanations below follow mainly the papers from Benson, Bigi, Mannel and Uraltsev [2, 41–43]. In the OPE, an auxiliary scale, μ, is introduced to separate short- and long-distance dynamics:

$$\Lambda_{\mathrm{QCD}} \ll \mu \ll m_b\,. \tag{2.64}$$

The expansion of the semileptonic $B_{(s)}$ width reads

$$\Gamma_{\mathrm{sl}}\left(B_{(s)}\right) = \frac{G_{\mathrm{F}}^2}{192\pi^3}|V_{cb}|^2 m_b^5 z_0(r)\left[1 + \frac{1}{2m_b^2}\left(c_G\mu_G^2 + c_\pi\mu_\pi^2\right) + \frac{1}{m_b^3}c_D\rho_D^3 + \ldots\right], \tag{2.65}$$

where the tree-level phase space factor is given by

$$z_0(r) = 1 - 8r + 8r^3 - r^4 - 12r^2 \ln r \text{ with } r = m_c^2/m_b^2 \,. \tag{2.66}$$

The leading term of the decay width is proportional to the fifths power of the b-quark mass, m_b. Therefore, the use of a suitable definition of the heavy-quark mass is crucial. The short-distance dynamics are contained in the coefficients c_G, c_π and c_D in Eq. 2.65, which can be calculated perturbatively in QCD. The approximate values of the coefficients are $c_G \approx 1$, $c_\pi \approx -1$ and $c_D \approx -16$. The long-distance dynamics are nonperturbative QCD effects and are absorbed in the effective operators μ_i. The leading operators are the *chromomagnetic operator* $\mu_G^2 \approx 0.35\,\text{GeV}^2$, the *kinetic operator* $\mu_\pi^2 \approx 0.45\,\text{GeV}^2$ and the *Darwin operator* $\rho_D^3 \approx 0.2\,\text{GeV}^3$. The predictive power of the theory arises from the fact that the expectation values of these operators can be extracted from measurements of the hadron masses and from measurements of inclusive semileptonic decays.

2.5.1 Determination of $|\mathbf{V_{cb}}|$ with inclusive semileptonic *B* decays

In order to determine $|V_{cb}|$ from inclusive semileptonic B decays, several observables are measured as a function of the lower lepton energy threshold, E_cut, with values between 0.6 GeV and 2.0 GeV. Typical observables are the partial branching fraction, $B_{E_\ell > E_\text{cut}}(B_{(s)} \to X_c \ell \nu)$, the shapes of the lepton energy spectra, E_ℓ, and the hadronic mass spectra, m_X^2. The moments of the measured distributions are studied rather than the differential spectra, since the precision of the QCD calculations is better for inclusive rates. The latest global fit of the heavy-quark expansion to the measurements of $B \to X_c \ell \nu$ decays from the experiments BaBar, Belle, CLEO, CDF and DELPHI gives [8]:

$$|V_{cb}| = (42.2 \pm 0.7) \times 10^{-3} \,, \tag{2.67}$$

where the uncertainty is the combination of the experimental and theoretical uncertainties of the fit. The b-quark mass, m_b was a free parameter in the fit. This result for $|V_{cb}|$ is slightly inconsistent with the result from the exclusive analyses (cf. Eq. 2.63).

2.5.2 Ratio of the semileptonic widths of the B_s and B^0 mesons

In the following, the SU(3)$_{\text{flavour}}$ symmetry breaking effects of the operators μ_i are evaluated to obtain an estimate for the ratio

$$\frac{\Gamma_{\text{sl}}(B_s)}{\Gamma_{\text{sl}}(B^0)} . \tag{2.68}$$

The discussion below is a summary of the arguments given in Ref. [42]. At zeroth order in $1/m_b$, the expression in Eq. 2.65 corresponds to the decay of a free b quark and thus does not depend on the light quark in the $B_{(s)}$ meson: the inclusive semileptonic decay widths of the B_s and the B^0 meson are thus expected to be identical. In other words, SU(3)$_{\text{flavour}}$ symmetry is expected to be conserved. However, the terms of higher order in $1/m_b$ may introduce sizeable SU(3)$_{\text{flavour}}$ symmetry breaking effects. The vanishing term linear in $1/m_b$ implies that the $B_{(s)}$ mass has no impact on the width. The masses of the final state hadrons, however, affect the semileptonic width indirectly by constraining the nonperturbative QCD expectation values, μ_i, in the $B_{(s)}$ meson. The expectation value of the *chromomagnetic operator*,

$$\mu_G^2(\mu) = \frac{1}{2M_{B_{(s)}}} \langle B_{(s)} | \bar{b} (\frac{i}{2} \sigma_{jk} G^{jk}) b | B_{(s)} \rangle_\mu , \tag{2.69}$$

can be extracted from the hyperfine splitting of the masses,

$$\Delta M_{B_{(s)}} = M_{B^*_{(s)}} - M_{B_{(s)}} \simeq \frac{4}{3} \frac{\mu_G^2}{2m_b} . \tag{2.70}$$

With $\Delta M_{B^0} = [45.78 \pm 0.35]$ MeV and $\Delta M_{B_s} = [49.0 \pm 1.5]$ MeV, one obtains

$$\frac{\mu_G^2(B_s)}{\mu_G^2(B^0)} \simeq 1.07 \pm 0.03 \tag{2.71}$$

This relatively small breaking of the SU(3)$_{\text{flavour}}$ symmetry leads to a small −0.25 % shift of $\Gamma_{\text{sl}}(B_s)$ with respect to $\Gamma_{\text{sl}}(B^0)$. The *kinetic operator* is defined by

$$\mu_\pi^2(\mu) = \frac{1}{2M_{B_{(s)}}} \langle B_{(s)} | \bar{b} (i\vec{D})^2 b | B_{(s)} \rangle_\mu \,. \tag{2.72}$$

From the difference of the B_s and B^0 meson masses, one can estimate

$$\bar{\Lambda}_s - \bar{\Lambda} \approx M_{B_s} - M_B \approx 85\,\text{MeV}\,, \tag{2.73}$$

and using $m_b = 4.6\,\text{GeV}$ and $m_c = 1.25\,\text{GeV}$ one obtains

$$\mu_\pi^2(B_s) - \mu_\pi^2(B^0) \simeq 0.041\,\text{GeV}^2\,. \tag{2.74}$$

However, $1/m_c^2$ corrections in the charm meson masses of the order of 30 to 50 MeV need to be taken into account, which doubles the expected SU(3)$_{\text{flavour}}$ symmetry breaking

$$\mu_\pi^2(B_s) - \mu_\pi^2(B^0) \simeq 0.08\,\text{GeV}^2 \ldots 0.1\,\text{GeV}^2\,, \tag{2.75}$$

and leads to a −0.15 % change of $\Gamma_{\text{sl}}(B_s)$ as compared to $\Gamma_{\text{sl}}(B^0)$. The SU(3)$_{\text{flavour}}$ symmetry breaking of the *Darwin operator*,

$$\rho_D^3 = \frac{1}{2M_{B_{(s)}}} \langle B_{(s)} | \bar{b} (-\frac{1}{2} \vec{D}\vec{E}) b | B_{(s)} \rangle_\mu \,, \tag{2.76}$$

can be evaluated by two approaches. In the first approach, the relation

$$\rho_D^3(B^0) \simeq \frac{2}{3} \frac{(\mu_\pi^2(B^0))^2}{\bar{\Lambda}} \tag{2.77}$$

from exact sum rules in the heavy quark limit is used to obtain

$$\frac{\rho_D^3(B_s)}{\rho_D^3(B^0)} \simeq \left(\frac{\mu_\pi^2(B_s)}{\mu_\pi^2(B^0)} \right)^2 \frac{\bar{\Lambda}}{\bar{\Lambda}_s} \simeq 1.27\,. \tag{2.78}$$

In the second approach based on the vacuum factorisation estimate for the four-fermion heavy quark operator, the relation

$$\frac{\rho_D^3(B_s)}{\rho_D^3(B^0)} \simeq \frac{f_{B_s}^2}{f_B^2} \gtrsim \frac{f_K^2}{f_\pi^2} = 1.43 \tag{2.79}$$

is obtained, where f_i are the axial decay constants of the mesons $i = B_s, B, K, \pi$. In both approaches, the SU(3)$_{\text{flavour}}$ symmetry breaking of ρ_D^3 is estimated to be of the order of 20 %, which corresponds to a −0.8 % relative change of $\Gamma_{\text{sl}}(B_s)$. The spin-orbit operator, $\rho_{LS}^3(\mu)$, also appearing at the order $1/m_b^3$ is expected to make no significant contribution to SU(3)$_{\text{flavour}}$ symmetry breaking. Other *higher order operators* cause a total enhancement of $\Gamma_{\text{sl}}(B_s)$ with respect to $\Gamma_{\text{sl}}(B^0)$ of about 0.5 %.

In conclusion, the *Darwin operator*, ρ_D^3, is the dominant SU(3)$_{\text{flavour}}$ breaking contribution and leads to a −0.8 % change of $\Gamma_{\text{sl}}(B_s)$ with respect to $\Gamma_{\text{sl}}(B^0)$. The *chromomagnetic* and the *kinetic operator* add a −0.25 % and −0.15 % change in the same direction. Only the *higher order operators* lead to a small relative increase of $\Gamma_{\text{sl}}(B_s)$ of about 0.5 %. On the whole, SU(3)$_{\text{flavour}}$ symmetry is only slightly broken in semileptonic $B_{(s)}$ decays and the ratio of the B_s to the B^0 width is predicted to be

$$\frac{\Gamma_{\text{sl}}(B_s)}{\Gamma_{\text{sl}}(B^0)} = 0.99 \pm 0.01\,. \tag{2.80}$$

This estimate goes in the opposite direction compared to the one obtained by Gronau and Rosner [44]:

$$\frac{\Gamma_{\text{sl}}(B_s)}{\Gamma_{\text{sl}}(B^0)} = 1.01\,. \tag{2.81}$$

Their estimate is based only on a simple phase-space model, i.e. the fact that the mass ratio $M_{B_s}/M_{D_s^{(*)}}$ is larger than $M_B/M_{D^{(*)}}$.

CHAPTER 3

The Belle experiment at KEKB

The data analysed in this thesis were collected by the Belle experiment at the KEKB e^+e^- collider in Tsukuba, Japan [45]. The KEKB facility depicted in Fig. 3.1 is a so-called "B-factory" designed to produce pairs of b-flavoured mesons, $B_{(s)}\bar{B}_{(s)}$, at high rates. For this, centre-of-mass energies of $\sqrt{s} = 10.58\,\text{GeV}$ and $\sqrt{s} = 10.87\,\text{GeV}$ corresponding to the $\Upsilon(4S)$ and $\Upsilon(5S)$ resonances, respectively, are particularly suitable. More information on the collected datasets can be found in the next chapter. High collision rates are achieved by using high beam currents (1.1 A for e^- and 2.6 A for e^+) and small beam sizes at the interaction point (90 µm in the horizontal direction and 1.9 µm in the vertical direction) [46]. A further increase of the collision rate was achieved with the installation of so-called "crab cavities" which compensate the crossing angle of 22 mrad at the interaction point [47]. The 8 GeV electron beam and the 3.5 GeV positron beam are injected from a linear accelerator complex at full energies into two rings of 3016 m circumference. The e^+ and e^- beam energies are chosen to be asymmetric for time-dependent measurements, so that the produced B mesons have a boost in the lab frame and the decay time of the B mesons can be related to the flight length between the e^+e^- collision point and the B decay vertex. This is

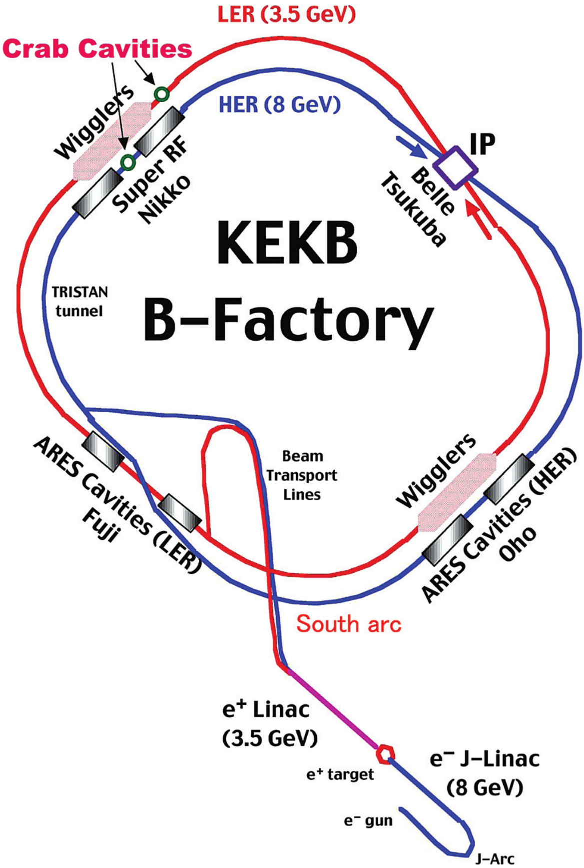

Figure 3.1: Schematic view of the KEKB facility. Figure taken from Ref. [45].

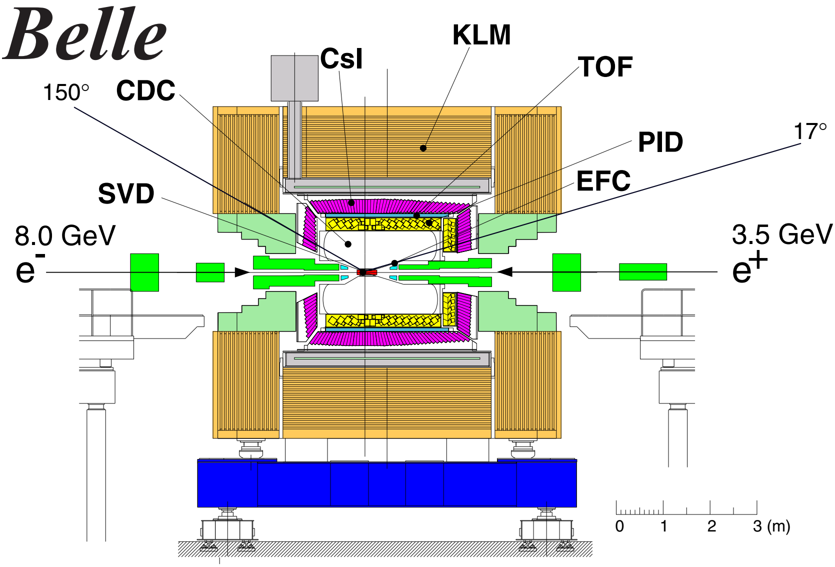

Figure 3.2: The Belle detector with the subdetectors from inside to outside: silicon vertex detector (SVD), extreme-forward calorimeter (EFC), central drift chamber (CDC), aerogel Cherenkov counters (PID), time-of-flight detectors (TOF), electromagnetic calorimeter (CsI), K_L and muon detector (KLM) [48].

particularly beneficial for studies of time-dependent CP violation in the decay of neutral B mesons. The Belle detector depicted in Fig. 3.2 is a system of subdetectors arranged in spherical layers around the nominal interaction point. Combining the information from the different subdetectors, the four-momenta of the traversing particles originating from the region close to the interaction point can be reconstructed. The nominal interaction point defines the origin of the coordinate system of the Belle detector. The z-axis of the coordinate system points in the direction of the electron beam, the y-axis points upwards and the x-axis is defined such that the system is right-handed. The Belle detector operated between 1 June 1999 and 30 June 2010 and collected a large data set which made it possible not only to discover CP violation in B^0 meson decays [49], but also to carry out many other interesting measurements such as the observation of direct and indirect *CP*-violation, the determination of CKM matrix elements, branching fraction measurements of rare decays and discoveries in the field fo hadron spectroscopy [50]. In the following, the functioning of the subdetectors will be briefly described – a detailed description of the Belle detector is given in Ref. [48].

3.1 Momentum measurement of charged particles

The tracks of charged particles are measured in the Central Drift Chamber (CDC) – a gas-filled cylindrical aluminium chamber with an inner radius of 8.3 cm, an outer radius of 88.0 cm and a length of 220.4 cm. A charged particle passing through the CDC creates a track of ionised gas atoms. A low-Z gas mixture (50 % helium and 50 % ethane) is chosen to minimise multiple scattering and to maintain a sufficient resolution for track momenta typically below 1 GeV. A high electrical potential is set at field wires to make the electrons from the ionisation of gas atoms drift towards sense wires where they trigger an electric signal which is then further processed. The Belle CDC comprises 50 cylindrical layers of sense and field wires with a total of 8400 drift cells. A super-conducting solenoid surrounding the detector creates a nearly homogeneous magnetic field, $\vec{B}$, with a field strength of about 1.5 T. Non-uniformities of the field are mapped by measuring the field strength at 100 000 points in the detector. The trajectories of charged particles are bent in the magnetic field due to the Lorentz force. The momentum of the particles, p, can be determined from the track radius, R, using the equation

$$R = \frac{p}{Q \cdot B}, \tag{3.1}$$

where Q is the particle charge. The transverse momentum resolution for tracks with a transverse momentum of 1 GeV is 0.35 % [51]. The optimal track parameters near the interaction point are determined with the most precise tracking detector, the silicon vertex detector (SVD). The analyses contained in this thesis use only the data taken with the second version of this detector [52] consisting of 4 layers of silicon strip detectors of which the innermost layer is located 2 cm from the beam line. The SVD firstly improves the track reconstruction precision and secondly allows for the determination of secondary vertices in time-dependent measurements. The latter feature of the SVD is not used for the analyses in this thesis, which are time-independent measurements.

3.2 Photon detection

The energy and direction of photons are measured with the electromagnetic calorimeter (ECL). The calorimeter is also important for the identification of electrons (see Sec. 5.3). The ECL is composed of a barrel section located at an inner radius of 1.25 m and two end caps located at $z = -1.0\,\mathrm{m}$ and $z = 2.0\,\mathrm{m}$. The acceptance region covers the polar angle range $17° \ldots 150°$. The ECL has a total mass of 43 tons and is constructed as a highly segmented array of 8736 CsI(TI) crystals. The fine segmentation allows for the resolution of two neighbouring photons from a π^0 decay. The tower-shaped crystals point to the interaction point with a small tilt of a few degrees to avoid photons escaping undetected in the gap between two crystals. The scintillation light signal is read out with a pair of silicon photodiodes and charge-sensitive preamplifiers at the end of each crystal, and is then transmitted for further processing. The energy resolution is measured to be $\sigma_E/E = 1.3\,\%/\sqrt{E/\mathrm{GeV}}$ and the position resolution $\sigma_{\mathrm{pos}} = 0.5\,\mathrm{cm}/\sqrt{E/\mathrm{GeV}}$. The Belle detector is also equipped with an extreme forward calorimeter (EFC), which is for example used to trigger events for the luminosity measurement.

3.3 Particle identification

At a B factory experiment, the separation of charged kaon and pion tracks is of particular importance for the reconstruction of charm and beauty mesons. The Belle detector contains several particle identification devices, each dedicated to specific particle types and a specific momentum range.

3.3.1 Specific ionisation in the CDC

The CDC does not only measure particle tracks, but also provides information about the energy loss of the particles due to ionisation per unit length, $-\mathrm{d}E/\mathrm{d}x$. This specific ionisation has a characteristic momentum dependence for every particle type and can be used for particle identification, in particular for the separation of kaons and pions (see Fig. 3.3). The energy loss for hadrons with electric charge $Q = e$ is given by the Bethe-Bloch formula [53, 54]:

$$-\frac{\mathrm{d}E}{\mathrm{d}x} = 2\pi N_a r_e^2 m_e c^2 \rho \frac{Z}{A} \frac{1}{\beta^2} \left[\ln\left(\frac{2 m_e \gamma^2 v^2 W_{\mathrm{max}}}{I^2} \right) - 2\beta^2 \right] . \tag{3.2}$$

The parameters in the Bethe-Bloch formula are:

r_e	Classical electron radius,
m_e	Electron mass,
N_a	Avogadro constant,
ρ	Density of the gas,
Z	Average atomic number of the gas,
A	Average atomic weight of the gas,
β	Particle velocity in units of c,
γ	$1/\sqrt{1-\beta^2}$,
I	Mean excitation potential of the gas,
W_{max}	Maximum energy transfer in a single collision: $\approx 2m_e c^2 \beta^2 \gamma^2$.

This is the most basic version of the Bethe-Bloch formula. There are several small effects that have to be taken into account by extra terms [55]: the *density* effect reduces the specific ionisation at higher particle momenta because polarised gas atoms along the particle trajectory lead to a shielding of the more distant gas atoms; the *shell* correction is necessary if the approximation that the particle velocity is much larger than the orbital velocity of the electrons bound in the gas atoms is not valid.

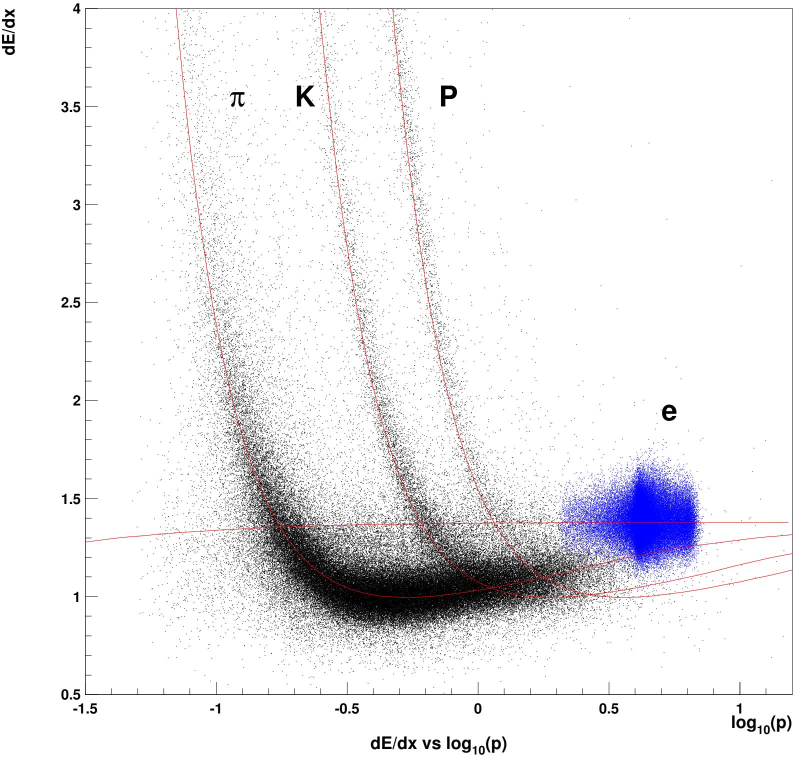

Figure 3.3: Truncated mean of dE/dx as a function of the momentum. The track momentum is given in units of GeV. The black and blue points are data recorded from e^+e^- collisions. The red lines represent the expected energy loss for pions, kaons, protons and electrons. Figure taken from Ref. [48].

3.3.2 Time-of-flight counters

The time-of-flight system (TOF) measures the flight time of a particle to determine its velocity. Combining this information with the measured particle momentum, the particle mass, and thus the particle species can be deduced. The TOF is equipped with 128 scintillator modules which are located at a radius of 1.2 m from the interaction point and covers polar angles between 34° and 120°. Charged particles with a minimum momentum of 0.28 GeV reach the system and particles with momenta up to approximately 1.2 GeV can be identified. A time resolution of 100 ps is achieved by

- choosing fast scintillators that have a long attenuation length of 3.9 m in average,
- avoiding long light guides,
- using large-area photocathodes directly mounted on the scintillators.

Besides particle identification, the TOF system provides fast timing signals for the trigger system. To keep the trigger rate below the design value of 70 kHz, the system is complemented by a second layer of 64 thin trigger scintillation counters to veto background from converted photons by requiring coinciding signals between the two layers [56].

3.3.3 Aerogel Cherenkov counters

To extend the coverage of the CDC and the TOF detectors for kaon/-pion separation to particles with momenta above 1.5 GeV, a system of silica Aerogel Cherenkov counters (ACC) is installed [57]. Cherenkov radiation is generated if a particle travels inside a medium with refractive index $n(\omega)$ faster than the speed of light in that medium:

$$v > \frac{c}{n} \,. \tag{3.3}$$

The Cherenkov light yield depends on the velocity, v, of the particles and therefore allows for a separation of kaon and pion tracks with known momentum [58]:

$$-\frac{\mathrm{d}E}{\mathrm{d}x} = \frac{4\pi e^2}{c^2} \int \omega \, \mathrm{d}\omega \left(1 - \frac{1}{\left(\frac{v}{c}\right)^2 n(\omega)^2} \right), \tag{3.4}$$

where the integral is over the frequencies with $n(\omega)v/c > 1$. The Cherenkov light yield is measured in the ACC with 960 modules in the barrel region and 228 modules in the end cap region. The refractive index of the aerogel is chosen between 1.01 and 1.03 depending on the polar angle region to ensure a good kaon/pion separation. A special treatment is applied to the silica gel making the surface hydrophobic in order to maintain a long-term transparency. The Cherenkov light yield is converted into electric charge by 1 or 2 mesh-type photomultiplier tubes per module. This kind of photomultipliers can be operated under the conditions of the strong magnetic field of 1.5 T in the Belle detector.

3.3.4 K_L and muon detection system

The K_L and muon detection system (KLM) consists in the barrel (endcap) region of 15 (14) layers of glass-electrode-resistive plate counters (RPC) alternating with 4.7 cm-thick iron layers. The RPCs consist of a gas-filled volume (62 % CH_2FCF_3, 30 % Ar, 8 % C_4H_{10}) between two parallel glass-plate electrodes to which a high voltage of about $\approx$ 8 kV is applied. Charged particles passing through theses devices cause ionisation of the gas leading to a local discharge of the plates which is registered by external pickup strips. The measured penetration depth and transverse scattering are used to discriminate muon tracks from charged kaons and pions. K_L can be detected after they are converted by nuclear interactions into charged particles. The probability that a K_L is converted is given in units of the interaction length defined by the distance after which the number of impinging K_L is reduced by a factor of $1/e$. The iron layers correspond to 3.9 interaction lengths and the ECL corresponds to 0.8 interaction lengths.

3.4 Luminosity measurement

The rate of produced $B_{(s)}\bar{B}_{(s)}$ pairs, $\mathrm{d}N/\mathrm{d}t$ is determined by the cross-section, σ, and the instantaneous luminosity, L, depending on the beam currents and the transversal overlap of the beams at the interaction point:

$$\frac{\mathrm{d}N}{\mathrm{d}t} = L \cdot \sigma \,. \tag{3.5}$$

The KEKB accelerator achieved the current world record with a peak luminosity of $L = 2.1 \times 10^{34}\,\mathrm{cm}^{-2}\mathrm{s}^{-1}$ [59]. The time-integrated luminosity, $\mathcal{L}$, determines the total number of collected $B_{(s)}\bar{B}_{(s)}$ pair events, N:

$$N = \int L \cdot \mathrm{d}t \cdot \sigma = \mathcal{L} \cdot \sigma \,. \tag{3.6}$$

The measurement of $\mathcal{L}$ is performed by studying two theoretically well understood reference processes: Bhabha scattering, $e^+e^- \to e^+e^-$, and two photon production, $e^+e^- \to \gamma\gamma$. The systematic uncertainty of this approach is about 1.5 % and it is dominated by the accuracy of radiative corrections. The Belle detector recorded in total $\mathcal{L} = 1040\,\mathrm{fb}^{-1}$ of data[1] comprising a $711\,\mathrm{fb}^{-1}$ sample of $\Upsilon(4S)$ data, a $121\,\mathrm{fb}^{-1}$ sample of $\Upsilon(5S)$ data and further samples collected at other Υ resonances, energy scans and off-resonance sidebands for the estimation of backgrounds (see Sec. 4.1).

3.5 Trigger

Table 3.1 lists the cross sections for $B_{(s)}$ meson production and for the expected backgrounds at the $\Upsilon(5S)$ and $\Upsilon(4S)$ centre-of-mass energies. The objective of the trigger logic is to select the hadronic events with high efficiency, to retain some of the BhaBha and $\gamma\gamma$ events for luminosity measurements and calibration purposes, but to reject the other beam-induced backgrounds. The trigger system is composed of a hardware trigger and several software triggers. The hardware trigger decision is based on redundant information from track and energy trig-

---

[1] $1\,\mathrm{b} = 1\,\mathrm{barn} = 1 \times 10^{-24}\,\mathrm{cm}^2$.

Physics process	Cross section [nb]	
	$\Upsilon(5S)$	$\Upsilon(4S)$
$B\bar{B}$	0.2	1.2
$B_s\bar{B}_s$	0.1	—
Hadron production from continuum	2.7	2.8
$\mu^+\mu^-$ and $\tau^+\tau^-$	1.5	1.6
BhaBha scattering ($\theta_{\text{lab}} > 17°$)	42	44
$\gamma\gamma$ ($\theta_{\text{lab}} > 17°$)	2.3	2.4
2γ process ($\theta_{\text{lab}} > 17°, p_t \geq 0.1\,\text{GeV}$)	14	15

Table 3.1: Cross sections of e^+e^- collisions at beam energies near the $\Upsilon(5S)$ and $\Upsilon(4S)$ resonance. Adapted from Ref. [48].

gers to guarantee high efficiencies under varying experimental conditions (see Fig. 3.4). The CDC makes a main contribution to the track trigger by providing information on the number of tracks, the maximum opening angle between tracks and the track topologies. It is complemented by the TOF for timing information and the KLM for muon identification. The energy trigger uses the total energy and the number of isolated clusters measured in the ECL. The EFC serves to select BhaBha and $\gamma\gamma$ events. The combined efficiency for the selection of hadronic events with the hardware trigger system is higher than 99.5 %. Software triggers are applied to the preselected events both online and during the offline processing of the data. They are based on more advanced but still simple track reconstruction algorithms. Before the final processing of the data for the analysis, further reduction of non-hadronic events is achieved with the so-called "HadronB" [60] algorithm, which selects events according to the track multiplicity, the visible energy of tracks and photons, the total reconstructed ECL energy, the average energy per ECL cluster, the momentum balance in the event, the reconstructed primary vertex and a variable sensitive to τ-pair events.

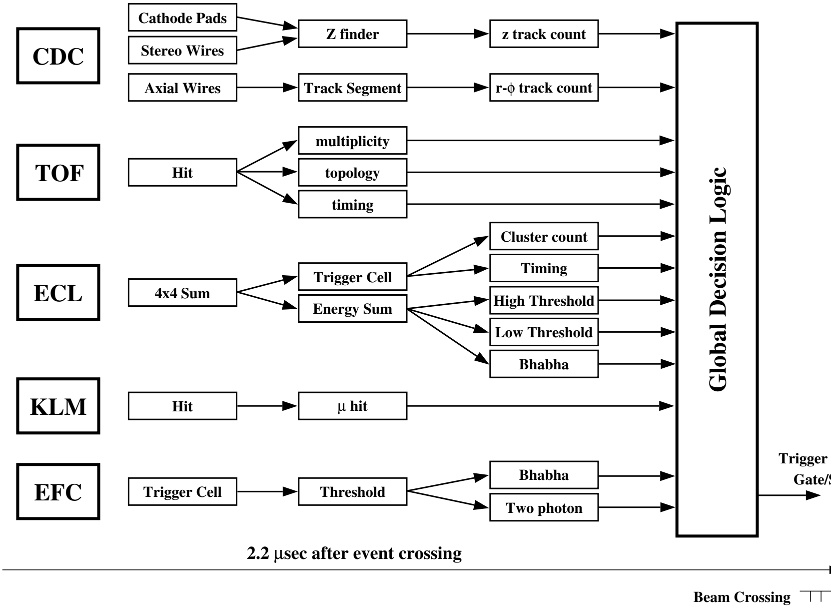

Figure 3.4: Overview of the Belle hardware trigger logic [48].

CHAPTER 4

The $\Upsilon(5S)$ data set

The Belle experiment was originally designed to study decays of B mesons produced in the process

$$e^+e^- \to \Upsilon(4S) \to B\bar{B}\,. \tag{4.1}$$

The $\Upsilon(4S)$ resonance has a mass of $[10\,579.4 \pm 1.2]$ MeV [8] and is a "bottomonium" state, a bound $b\bar{b}$ system. It decays nearly exclusively to $B\bar{B}$ pairs.[1] The operation of the experiment at a centre-of-mass energy of the e^+e^- collision corresponding to the mass of the $\Upsilon(4S)$ resonance has several advantages. Firstly, the $b\bar{b}$ cross section and hence the $B\bar{B}$ production is enhanced due to the resonant process. Secondly, the difference between the $\Upsilon(4S)$ mass and twice the B mass is very small, only about 20 MeV [8]. Therefore B mesons decay almost at rest in the rest frame of the e^+e^- collision. This can be used as an additional constraint to deduce the presence of unreconstructed particles such as neutrinos.

Figure 4.1 shows the rate of produced hadronic events as a function of the centre-of-mass energy, $\sqrt{s}$. The increase in the cross section at the $\Upsilon(4S)$ resonance is clearly visible. At a higher energy of

---

[1] $\mathcal{B}(\Upsilon(4S) \to \text{non } B\bar{B}) < 4\,\%$ at the 95 % confidence level [61].

[10 876 ± 11] MeV [8], another, less pronounced peak can be identified: the $\Upsilon(5S)$ resonance. The $\Upsilon(5S)$ resonance is also interpreted as a bottomonium state and was already observed in 1985 by the CLEO and CUSB collaborations in 0.1 fb^{-1} of data collected at the Cornell Electron Storage Ring [62, 63]. As the $\Upsilon(5S)$ mass of [5366.77 ± 0.24] MeV [8] is larger than twice the B_s mass it was expected that it can decay to $B_s\bar{B}_s$ pairs. It took nearly two decades to verify this assumption; in 2003, the analysis of a larger $\Upsilon(5S)$ sample of 0.42 fb^{-1} collected by the CLEO III detector led to the first evidence for B_s production at the $\Upsilon(5S)$ collision energy [64, 65]. This aroused interest in the Belle collaboration to study B_s decays and a large sample of $\Upsilon(5S)$ data with a total integrated luminosity of 121.4 fb^{-1} was collected between 2005 and 2009.

In contrast to the $\Upsilon(4S)$ resonance, which nearly exclusively decays into B pairs, the production of b-flavoured particles in $\Upsilon(5S)$ decays is much more diverse. Figure 4.2 illustrates the classification of hadronic events at the $\Upsilon(5S)$ beam energy. First of all, hadronic events can be categorised in the two cases: the production of either $b\bar{b}$ pairs or pairs of the lighter quarks ("u, d, s, c continuum"). In the former case, three different types of events can be distinguished: events with B_s production, events with B production and events with bottomonium production ("non-$B_{(s)}$"). The production of $B_{(s)}$ pairs includes also the excited states $B^*_{(s)}$. The production of B pairs can be even accompanied by an additional pion. A thorough understanding of the various event types in $\Upsilon(5S)$ decays is indispensable for any kind of B_s measurement with these data. This chapter is dedicated to the discussion of the $\Upsilon(5S)$ data set and the modelling of the processes in $\Upsilon(5S)$ decays.

4.1 Light quark continuum

When electrons and positrons are brought to collision at the $\Upsilon(5S)$ centre-of-mass energy, the majority of the produced hadronic events are not $b\bar{b}$ pairs, but form the "continuum" processes

$$e^+e^- \to q\bar{q} \quad (q = u, d, s, c)\,. \tag{4.2}$$

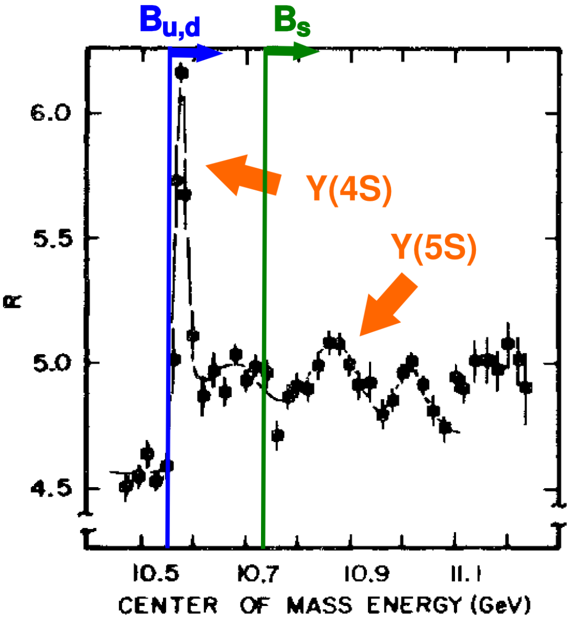

Figure 4.1: Ratio $R = \sigma(e^+e^- \to \text{hadrons})/\sigma(e^+e^- \to \mu^+\mu^-)$ as a function of the centre-of-mass energy. The ratio is plotted before the subtraction of backgrounds. The vertical lines illustrate the thresholds for $B\,\bar{B}$ and $B_s\,\bar{B}_s$ production. Adapted from Ref. [62].

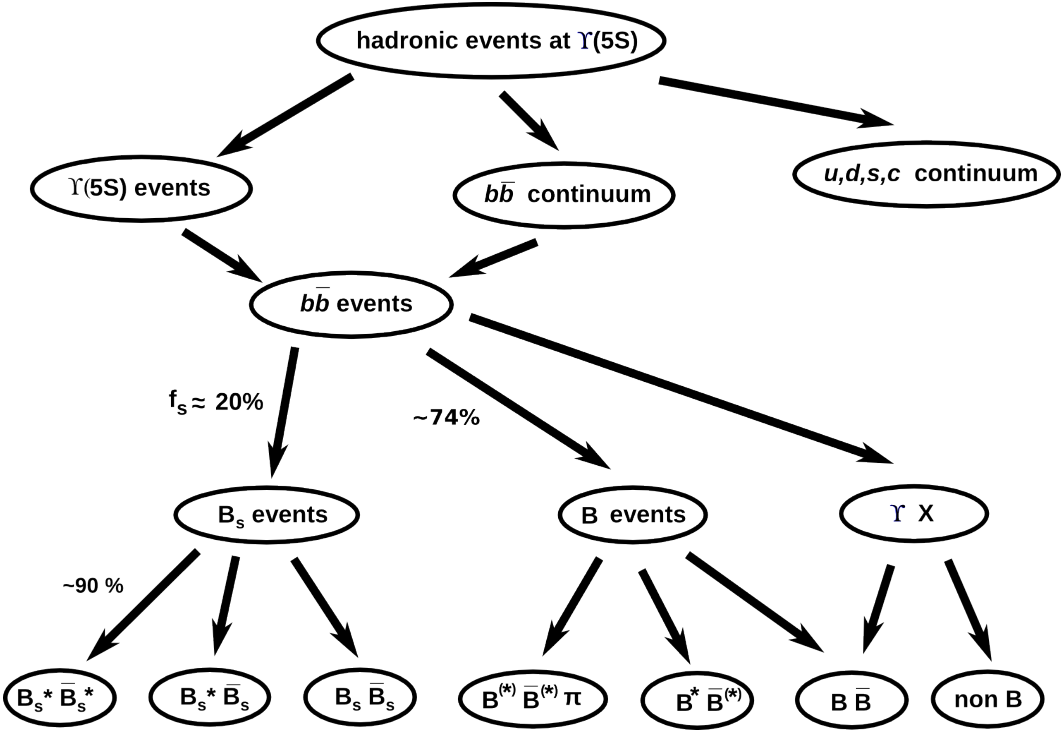

Figure 4.2: Classification of $\Upsilon(5S)$ decays. The category "ΥX" summarises decays to bottomonium states with lower masses (e.g. $\Upsilon(5S) \to \Upsilon(1S)\pi\pi$) and the initial state radiation processes $e^+e^- \to \Upsilon(4S)\gamma_{\mathrm{ISR}}$.

Since this background is large (cf. Table 3.1), its efficient suppression is crucial for analyses of $B_{(s)}$ decays. For this purpose, an elaborate set of variables based on the kinematics of the reconstructed particles and the event topology was developed at the B-factories [50]. In the analyses presented in this thesis, rather simple selection criteria are applied for continuum suppression, discussed later in Sec. 5.4. Applying these criteria, a large fraction of continuum events can be suppressed, but they cannot be eliminated completely. The remaining number of continuum events has to be estimated and subtracted. One possibility to obtain an estimate for the continuum is to simulate the production process with MC techniques. However, the modelling of the $q\bar{q}$ hadronisation is challenging and still far from being fully understood. Therefore, a data-driven approach is preferred, using so-called "off-resonance" samples collected at a beam energy of $\sqrt{s} = 10.52\,\mathrm{GeV}$, below the production threshold of $B\bar{B}$ pairs. These samples exclusively contain continuum events which are produced in very similar conditions as the $\Upsilon(5S)$ data. The total integrated luminosity of the off-resonance data is $\mathcal{L}_{\mathrm{off}} = 62.8\,\mathrm{fb}^{-1}$. To estimate the continuum contribution in $\Upsilon(5S)$ data, the event yields obtained from the off-resonance samples need to be corrected with a scale factor for the difference in integrated luminosities, $\mathcal{L}$, and the $1/s$ dependence of the $e^+e^- \rightarrow q\bar{q}$ cross section

$$S_{\mathrm{cont.}} = \frac{\mathcal{L}_{\Upsilon(5S)}}{\mathcal{L}_{\mathrm{off}}} \cdot \frac{s_{\mathrm{off}}}{s_{\Upsilon(5S)}} = 1.81\,. \tag{4.3}$$

4.2 Measurement of the $b\bar{b}$ cross section

The more interesting part of the hadronic events – at least for the analyses in this thesis – are, of course, the ones where $b\bar{b}$ pairs are produced. The $b\bar{b}$ production via $\Upsilon(5S)$ production interferes with non-resonant production analogous to the continuum of the lighter quarks discussed above. In the literature the convention became established to use the notations "$\Upsilon(5S)$" and $b\bar{b}$ equivalently for any kind of $b\bar{b}$ event.

The cross section $\sigma(e^+e^- \rightarrow b\bar{b})$ at the $\Upsilon(5S)$ centre-of-mass energy was determined by measuring the yield of hadronic events in on-resonance data and subtracting the continuum contribution estimated from off-resonance data [66]:

$$N^{b\bar{b}}_{\Upsilon(5S)} = \frac{1}{\epsilon^{b\bar{b}}_{\Upsilon(5S)}} \left(N^{\text{had}}_{\Upsilon(5S)} - N^{\text{had}}_{\text{off}} \cdot S_{\text{cont.}} \cdot \frac{\epsilon^{q\bar{q}}_{\Upsilon(5S)}}{\epsilon^{q\bar{q}}_{\text{off}}} \right), \tag{4.4}$$

where $N^{\text{had}}_{\Upsilon(5S)}$ and $N^{\text{had}}_{\text{off}}$ are the yields of hadronic events measured in $\Upsilon(5S)$ and off-resonance data, respectively, $\epsilon^{b\bar{b}}_{\Upsilon(5S)}$ is the selection efficiency for $b\bar{b}$ events, $\epsilon^{q\bar{q}}_{\Upsilon(5S)}/\epsilon^{q\bar{q}}_{\text{off}}$ the efficiency ratio for liqht quark continuum events in $\Upsilon(5S)$ and off-resonance data, and $S_{\text{cont.}}$ is the scale factor defined in Eq. 4.3. CLEO measured $\sigma(e^+e^- \to b\bar{b}) = [301 \pm 39]$ pb in $0.42\,\text{fb}^{-1}$ of $\Upsilon(5S)$ data [67], Belle measured $[302 \pm 15]$ pb in $1.86\,\text{fb}^{-1}$ of $\Upsilon(5S)$ data [66]. The method documented in Ref. [66] was later applied to the full $121.4\,\text{fb}^{-1}$ data set with the result [68]:

$$\sigma_{\Upsilon(5S)}(e^+e^- \to b\bar{b}) = [340 \pm 16]\ \text{pb}\,. \tag{4.5}$$

The dominating uncertainty of the measurement is due to the luminosity ratio $\mathcal{L}_{\Upsilon(5S)}/\mathcal{L}_{\text{off}}$ in the continuum scale factor, $S_{\text{cont.}}$. Since the continuum background subtracted in Eq. 4.4 is large compared to the remaining number of $b\bar{b}$ events, $N^{b\bar{b}}_{\Upsilon(5S)}$ (cf. Table 3.1), this uncertainty has a large impact on the final result and cannot easily be reduced.

4.3 Determination of B_s production at $\Upsilon(5S)$

The $b\bar{b}$ events produced at the $\Upsilon(5S)$ resonance can be divided into three categories: B_s events, B events and events without $B_{(s)}$ production. The production fractions are [8]:

$$f_s = [19.9 \pm 3.0]\ \%\,, \quad f_{u,d} = \left[75.9\,^{+2.7}_{-4.0}\right]\ \%\,, \quad f_{\text{non}B} = \left[4.2\,^{+5.0}_{-0.6}\right]\ \%\,. \tag{4.6}$$

By definition, the three production fractions sum up to unity,

$$f_s + f_{u,d} + f_{\text{non}B} = 1\,. \tag{4.7}$$

The B_s production, f_s, can for instance be determined from a measurement of inclusive D_s production in $\Upsilon(5S)$ decays. The measured branching fraction $\mathcal{B}(\Upsilon(5S) \to D_s X)$ is related to f_s by the equation

$$\mathcal{B}(\Upsilon(5S) \to D_s X)/2 = f_{u,d}\mathcal{B}(B \to D_s^{\pm} X) + f_s \mathcal{B}(B_s \to D_s^{\pm} X)\,, \tag{4.8}$$

where the factor $1/2$ on the left side takes into account that $B_{(s)}$ mesons are produced in pairs in $\Upsilon(5S)$ decays. The sensitivity to B_s production is due to the fact that the branching fraction $\mathcal{B}(B \to D_s^{\pm} X) = [8.3 \pm 0.8]$ % is significantly smaller than the branching fraction, $\mathcal{B}(B_s \to D_s^{\pm} X) = [92 \pm 11]$ %. Events with more than one D_s meson in the final state, for example the decays $B_s \to D_s^{+(*)} D_s^{-(*)}$, are double-counted in these branching fractions, i.e. they may take values larger than 100 %. The value of $\mathcal{B}(B \to D_s^{\pm} X)$ is determined from a measurement in $\Upsilon(4S)$ data [64, 69, 70]; the branching fraction $\mathcal{B}(B_s \to D_s^{\pm} X)$ is estimated in a model-dependent way [64]. Using the approximation $f_{\text{non}B} \approx 0$, the parameter $f_{u,d}$ in Eq. 4.8 can be replaced by $1 - f_s$ (cf. Eq. 4.7) and the parameter f_s remains the only unknown. The Belle collaboration applied the described technique [66] to the full 121.4 fb^{-1} data set and obtained the value

$$f_s = [17.2 \pm 3.0]\ \%\,, \tag{4.9}$$

which is now the official value used for Belle analyses.[2] Together with the cross section from Eq. 4.5 the total number of B_s pairs contained in the $\mathcal{L} = 121.4\,\text{fb}^{-1}$ sample collected at the $\Upsilon(5S)$ resonance is:

$$N_{B_s \bar{B}_s} = \mathcal{L}\, \sigma(e^+e^- \to b\bar{b})\, f_s = (7.1 \pm 1.3) \times 10^6\,. \tag{4.10}$$

The dominating uncertainty in this f_s extraction is due to the estimate of the branching fraction $\mathcal{B}(B_s \to D_s^{\pm} X)$. The measurement of the inclusive D_s yield together with Eq. 4.8 could also be used to extract the value of $\mathcal{B}(B_s \to D_s^{\pm} X)$ if f_s was known from other measurements.

The parameter f_s can be also determined from the measurement of other inclusive yields in $\Upsilon(5S)$ decays, for example the inclusive ϕ yield

---

[2] There is a difference between Ref. [66] and the analysis using the full 121.4 fb^{-1} data set: The former reconstructs $D_s \to \phi\pi$; $\phi \to K^+K^-$ while the latter does not require an intermediate ϕ meson and reconstructs $D_s \to K^+K^-\pi$.

(enhanced in B_s decays) [67] or the inclusive D^0 production (enhanced in B decays) [66]. An alternative method to determine f_s was proposed by Sia and Stone [71]. It is based on the reconstruction of same-sign and opposite-sign lepton pairs and exploits the different mixing probabilities of B_s and B^0 mesons. A first attempt to implement this method [72] was not successful because of modelling problems in the lepton momentum spectra of signal and background processes [73]. LHCb and the LEP experiments used $B_s \to D_s X \ell \nu$ decays for the estimation of the B_s production at their facilities [7, 74–76]. It will be shown later that this approach also provides a competitive estimate at Belle (see Sec. 8.1).

The B production, $f_{u,d}$, was determined by fully reconstructing B mesons in hadronic decay modes. The total production of B^0 and B^+ mesons in $\Upsilon(5S)$ decays was measured separately [67, 77, 78]:

$$\begin{aligned} f_d &= \mathcal{B}(\Upsilon(5S) \to B^0 X)/2 &&= [36.1 \pm 3.2]\ \%\,, \\ f_u &= \mathcal{B}(\Upsilon(5S) \to B^+ X)/2 &&= [38.5 \pm 4.2]\ \%\,. \end{aligned} \tag{4.11}$$

The measurements are compatible with B^+ and B^0 being produced with equal probability in $\Upsilon(5S)$ decays. The precision of $f_{u,d}$ achieved with these measurements is approximately 10 %. If one wants to convert this result into a statement on f_s using Eq. 4.7, the fact that f_s is approximately a factor of four smaller than $f_{u,d}$ leads to a four times higher relative uncertainty of f_s. The attempt to determine f_s with satisfactory precision from the measurement of the B production fraction is thus hopeless.

The production fraction of lower-mass bottomonium states, $f_{\mathrm{non}B}$, is relatively small compared to $f_{u,d}$ and f_s. So far, branching fractions of the following decays have been measured:

- $\Upsilon(5S) \to \Upsilon(n\mathrm{S})\pi\pi$ ($n = 1, 2, 3$) [79],
- $\Upsilon(5S) \to \Upsilon(1\mathrm{S})K^+K^-$ [79],
- $\Upsilon(5S) \to \Upsilon(n\mathrm{S})\pi^0\pi^0$ ($n = 1, 2, 3$) [80],
- $\Upsilon(5S) \to h_b(n\mathrm{P})$ ($n = 1, 2$) [81, 82].

Summing up these branching fractions, one obtains $\mathcal{B}(\Upsilon(5S) \to \mathrm{non}\,B) = [4.1 \pm 0.6]$ % which provides a lower limit for $f_{\mathrm{non}B}$ [72].

By analogy to $\Upsilon(4S)$ decays, the bottomonium production in $\Upsilon(5S)$ decays is expected to be much lower [83, 84]. The branching fractions of the processes $\Upsilon(5S) \rightarrow \Upsilon(n\mathrm{S})\pi\pi$ ($n = 1,2,3$) are, however, measured to be a factor of about 100 higher than the expectation [79]. Closer investigations of these unnaturally large branching fractions led to the discovery of the exotic Z_b tetraquark states [82, 85]. These states are produced via $\Upsilon(5S) \rightarrow Z_b\pi$ and can decay into $\Upsilon(n\mathrm{S})\pi$, while the dominant decay mode is into $B^{(*)}B^*$ pairs [86]. A recent analysis of Belle data comes to the conclusion that the $\Upsilon(5S)$ resonance decays exclusively to the exotic Z_b states [87]. This also implies that B_s mesons stem only from non-resonant $b\bar{b}$ production.

4.4 Characterisation of $\Upsilon(5S)$ events in the ΔE-M_{bc} plane

So far, only the follwoing three categories of $\Upsilon(5S)$ decays were discussed: B_s, B and non-$B_{(s)}$. The categorisation of events can be further refined by investigating, if the $B_{(s)}$ mesons are produced in the ground state or an excited state and whether an additional pion is produced or not. This determines the CP eigenstate in which a pair of neutral $B_{(s)}$ mesons is produced and has an impact on the mixing probability (cf. Eq. 2.27). The following variables are calculated to characterise the $\Upsilon(5S)$ events:

$$\begin{aligned} \text{Missing energy:} \quad \Delta E &= \quad E^*_{B_{(s)}} - \sqrt{s}/2\,, \\ \text{Beam-constrained mass:} \quad M_{\mathrm{bc}} &= \quad \sqrt{s/4 - p^*_{B_{(s)}}}\,. \end{aligned} \tag{4.12}$$

The energy, $E^*_{B_{(s)}}$, and the momentum, $p^*_{B_{(s)}}$, of the reconstructed $B_{(s)}$ meson are calculated in the centre-of-mass frame of the e^+e^- collision, which is indicated by the "*" symbol. In case of $B_{(s)}\bar{B}_{(s)}$ pair production, ΔE is equal to zero and M_{bc} is at the nominal $B_{(s)}$ mass. The more additional particles are produced in the event (including photons from $B^*_{(s)}$ decays), the more the associated ΔE value is shifted to negative values and the higher is M_{bc}. This allows the relative rates of the different decay modes to be measured by investigating the event yields in the different regions of the two-dimensional ΔE-M_{bc} plane, as illustrated in Fig. 4.3 (left).

Figure 4.3 (right) shows as an example the ΔE-M_{bc} plane for $B_s \to D_s^- \pi^+$ events reconstructed in $\Upsilon(5S)$ data. The current world averages of the B_s production branching fractions are [8]

$$\begin{aligned} F'_{B_s^* \bar{B}_s^*} &= \mathcal{B}(\Upsilon(5S) \to B_s^* \bar{B}_s^*)/f_s &&= [87.8 \pm 1.5]\ \%\,, \\ F'_{B_s^* \bar{B}_s} &= \mathcal{B}(\Upsilon(5S) \to B_s^* \bar{B}_s)/f_s &&= [6.7 \pm 1.2]\ \%\,, \\ F'_{B_s \bar{B}_s} &= \mathcal{B}(\Upsilon(5S) \to B_s \bar{B}_s)/f_s &&= [2.6 \pm 2.6]\ \%\,. \end{aligned} \tag{4.13}$$

The measured M_{bc} distribution of reconstructed B_s mesons is also used to determine the B_s^* mass because a direct reconstruction of the photon from the $B_s^* \to B_s \gamma$ decay is not feasible due to the low photon energy of $\left[48.7\,^{+2.3}_{-2.1}\right]$ MeV in the B_s^* rest system, which results in the experiment to photon energies near the detection threshold. The B_s^* mass was measured by CLEO [78] and Belle [88]; the results of the two experiments are inconsistent:

$$\begin{aligned} \text{CLEO:} \quad & [5411.7 \pm 1.6\,(\text{stat.}) \pm 0.6\,(\text{syst.})]\ \text{MeV}\,, \\ \text{Belle:} \quad & [5416.4 \pm 0.4\,(\text{stat.}) \pm 0.5\,(\text{syst.})]\ \text{MeV}\,. \end{aligned} \tag{4.14}$$

Therefore, the Particle Data Group [8] scales the uncertainty of their average up to reach a value of $\chi^2/\mathrm{ndf} = 1$ for the combination:

$$M_{B_s^*} = \left[5415.4\,^{+2.4}_{-2.1}\right]\ \text{MeV}\,. \tag{4.15}$$

The distribution of events with a reconstructed B meson in the ΔE-M_{bc} plane reveals two classes of events: events with small M_{bc} values can be attributed to two-body decays, $\Upsilon(5S) \to B^{(*)}\bar{B}^{(*)}$; events with large M_{bc} values originate from three-body decays, $\Upsilon(5S) \to B^{(*)}\bar{B}^{(*)}\pi$ or the initial state radiation (ISR) process $\Upsilon(5S) \to \gamma_{\mathrm{ISR}}\Upsilon(4S); \Upsilon(4S) \to$

$B\bar{B}$. The current world averages of the B two-body decay branching fractions are [8]:

$$\begin{aligned} F_{B\bar{B}} &= \mathcal{B}(\Upsilon(5S) \to B\bar{B}) &&= [5.5 \pm 1.0]\ \%\,, \\ F_{B^*\bar{B}} &= \mathcal{B}(\Upsilon(5S) \to B^*\bar{B}) &&= [13.7 \pm 1.6]\ \%\,, \\ F_{B^*\bar{B}^*} &= \mathcal{B}(\Upsilon(5S) \to B^*\bar{B}^*) &&= [38.1 \pm 3.4]\ \%\,, \\ F_2 &= F_{B\bar{B}} + F_{B^*\bar{B}} + F_{B^*\bar{B}^*}\,. \end{aligned} \tag{4.16}$$

The fractions of the large M_{bc} contributions are [77]:

$$\begin{aligned} F'_{B\bar{B}\pi} &= \mathcal{B}(\Upsilon(5S) \to B\bar{B}\pi)/(f_{u,d} - F_2) &&= [0.2 \pm 6.8]\ \%\,, \\ F'_{B^*\bar{B}\pi} &= \mathcal{B}(\Upsilon(5S) \to B^*\bar{B}\pi)/(f_{u,d} - F_2) &&= [41.6 \pm 12.1]\ \%\,, \\ F'_{B^*\bar{B}^*\pi} &= \mathcal{B}(\Upsilon(5S) \to B^*\bar{B}^*\pi)/(f_{u,d} - F_2) &&= [5.9 \pm 7.8]\ \%\,, \\ F'_{ISR} &= 1 - F'_{B\bar{B}\pi} - F'_{B^*\bar{B}\pi} - F'_{B^*\bar{B}^*\pi}\,. \end{aligned} \tag{4.17}$$

It is assumed for B two-body decays and the ISR process that the B^+ and B^0 fractions are equal: $f_u^{(2)} = f_d^{(2)} = \frac{1}{2}$. In the case of three-body decays, the additional pion allows for either the production of B pairs of the same type, B^+B^- and $B^0\bar{B}^0$, or the mixed combinations $B^+\bar{B}^0$ and B^-B^0. From isospin considerations follows that the fraction of same-type combinations is $f_d^{(3)} = f_u^{(3)} = \frac{1}{6}$ and the mixed-type fraction is $f_{u,d}^{(3)} = \frac{2}{3}$ [72].

4.5 Monte Carlo simulation

Decays at the $\Upsilon(5S)$ and off-resonance beam energies are simulated with Monte Carlo (MC) techniques to study the kinematic distributions and the efficiencies of the various signal and background contributions. The size of the generated MC samples corresponds to six times the integrated luminosity of the data in order to keep the uncertainty due to the MC statistics small in measurements. Particle decays are generated with the EvtGen program, which was originally developed for the experiments CLEO and BaBar and then adapted for Belle [89]. The simulation uses as input two lists. The first one contains the properties of the simulated particles, for example:

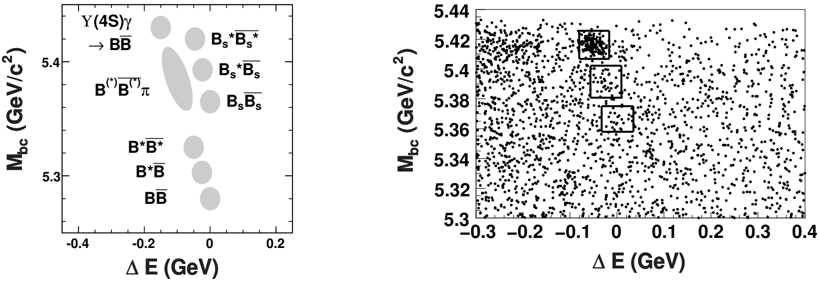

Figure 4.3: The different $\Upsilon(5S)$ decay modes in the ΔE-M_{bc} plane: (left) preferred regions for events with one fully reconstructed $B_{(s)}$ meson; (right) Sample of reconstructed $B_s \to D_s^- \pi^+$ decays from a 23.6 fb^{-1} sample of $\Upsilon(5S)$ data collected at Belle [88]. The corresponding $B_s^* \bar{B}_s^*$, $B_s^* \bar{B}_s$ and $B_s \bar{B}_s$ regions are indicated by boxes.

```
Meson     D_s+     431  1.96849   0    3    0  0.1470
Meson     D_s*+    433  2.1123    0    3    2       0
```

The meaning of the columns is from left to right: the particle type, the identifying string, the identifying integer number, the mass in GeV, the width in GeV, the charge multiplied by 3, the spin multiplied by 2, and the lifetime multiplied by $c \cdot \mathrm{mm}^{-1}$. The second list contains the decay modes with the branching fractions and the decay models used for the generation. For $B_s \to D_s^{(*)} e^+ \nu_e$ decays, this reads for example as follows:

```
Decay B_s0
0.0210   D_s-     e+     nu_e          PHOTOS  ISGW2;
0.0490   D_s*-    e+     nu_e          PHOTOS  ISGW2;
```

The first entry in a row is the branching fraction of the decay mode followed by the daughter particles of the decay. The last entry in each row is the decay model (here: `ISGW2`) that is used for the event generation. The additional parameter `PHOTOS` describes the simulation of final state photon radiation with the PHOTOS package [90].

The B_s branching fractions and the B_s decay parameters are mostly unknown. Therefore the simulation parameters are chosen in analogy to B decays. The simulation considers 223 different decay modes of the B_s meson. For about 43% of the total B_s decay width, no explicit final state is specified and the PYTHIA package [91] takes care of the final state hadronisation. Semileptonic B_s decays are simulated with different models depending on the decay channel. The CLN model is used for $B_s \to D_s^{(*)}\ell\nu$ decays with the model parameters determined in B measurements assuming $\mathrm{SU(3)}_{\mathrm{flavour}}$ symmetry. For $B_s \to D_s^{**}\ell\nu$ decays, the LLSW model is used in the $B_s \to D_s^{(*)}X\ell\nu$ analyses and the ISGW2 model is used in the $B_s \to X\ell\nu$ analysis. The technical details, how the model predictions are considered in the simulation, are given in Appendix A. A challenge in the MC modelling is also the poor knowledge of the D_s^{**} decay modes. Except for a few branching fraction measurements the statements by the Particle Data Group on the D_s^{**} decay modes range from "not seen" over "possibly seen" to "seen" [8]. Table 4.1 summarises the assumptions made in the MC simulation. Besides B_s events, also events with B mesons and bottomonium states are simulated as well as the process $e^+e^- \to q\bar{q}$ $(q = u, d, s, c)$.

The interaction of the simulated particles with the detector is simulated with the GEANT [92] software. In GEANT, a virtual model of the full detector geometry including the arrangement and the materials of the detector components, is implemented. The interaction of a particle with the detector materials is estimated by dividing the particle trajectory into small steps and calculating for each step the probability and outcome of an interaction. The simulated energy deposit is converted into the detector response ("digitisation") and the signal processing as well as the trigger behaviour are emulated. Imperfections of the detector simulation caused by the necessary simplifications of the detector geometry and material budget are studied by comparing data distributions of well-known decays to the corresponding MC prediction. Based on these studies, correction factors are calculated and applied to the MC sample. Details on these calibration factors can be found in Chapter 5.

			Branching fraction	
Mode			Belle MC	Particle Data Group
Decays to D_s mesons				
$D_{s1}(2536)$	$\rightarrow$	D_sX	0 %	seen
D^*_{s0}	$\rightarrow$	D_sX	100 %	seen
$D'_{s1}(2460)$	$\rightarrow$	D_sX	100 %	$\sum > 75\%$
D^*_{s2}	$\rightarrow$	D_sX	0 %	—
Decays to D^*_s mesons				
$D_{s1}(2536)$	$\rightarrow$	D^*_sX	0 %	possibly seen
D^*_{s0}	$\rightarrow$	$D^*_s\gamma$	3 %	$< 6\,\%$
D^*_{s0}	$\rightarrow$	$D^*_s\pi^0$	0 %	$< 11\,\%$
$D'_{s1}(2460)$	$\rightarrow$	D^*_sX	63 %	$\sum \approx 52\%$
D^*_{s2}	$\rightarrow$	D^*_sX	0 %	—
Decays to non $D_s^{(*)}$ mesons				
$D_{s1}(2536)$	$\rightarrow$	D^*K	100 %	$[85 \pm 12]\,\%$
$D_{s1}(2536)$	$\rightarrow$	DKX	0 %	$3 \ldots 24\,\%$
D^*_{s2}	$\rightarrow$	DK	90 %	seen
D^*_{s2}	$\rightarrow$	D^*K	10 %	not seen

Table 4.1: Branching fractions of D_s^{**} mesons in the Belle MC simulation and the information available from the Particle Data Group [8]. The decays to D_s mesons contain also the cases where the D_s meson does not stem directly from a D_s^{**} meson, but from the decay of an intermediate D_s^* meson.

CHAPTER 5

Event reconstruction

Figure 5.1 gives an impression of the topology of an $\Upsilon(5S) \rightarrow B_s\bar{B}_s$ event with a semileptonic B_s decay. In this thesis, semileptonic B_s decays are studied, where the lepton, ℓ^+, is either an electron or an muon. The decays are analysed in both a semi-inclusive and an inclusive approach. In the semi-inclusive $B_s \rightarrow D_s^{(*)}X\ell\nu$ analysis [93], semileptonic B_s decays with a $D_s^{(*)}$ meson in the final state are studied. The final state may contain additional hadrons and photons, X, which are not reconstructed. The reconstructed particles are $D_s^{(*)-}\ell^+$ pairs[1] with opposite-sign electric charges. Only one of the two B_s mesons in the event is used as illustrated in Fig. 5.2 (a). In the inclusive $B_s \rightarrow X\ell\nu$ analysis [94], the hadronic part, X, of the final state is not specified and the lepton, ℓ^+, is the only reconstructed particle of the signal decay. To suppress the background from B production in $\Upsilon(5S)$ decays, a D_s^+ meson from the decay of the second B_s meson in the event is additionally reconstructed (see Fig. 5.2 (b)). The selection of $D_s^+\ell^+$ pairs with same-sign electric charges ensures that both particles stem from decays of different B_s mesons.

---

[1] Throughout this thesis, the inclusion of the charge conjugate mode is implied unless otherwise stated.

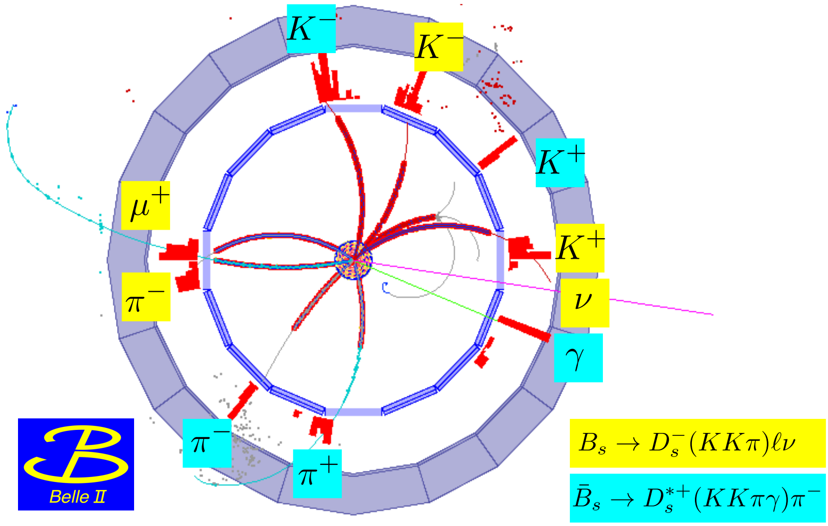

Figure 5.1: Event display of a simulated semileptonic B_s decay in the Belle II detector. For technical reasons, the Belle II software was used to generate this event display, but the event topology looks similar in the Belle detector. The thin, curved lines represent the generated particle trajectories. The inner region shows the vertex detector and the CDC hits. The inner blue ring represents the TOF counters. The energy deposited in the ECL is shown as red histograms. The outer blue ring is the KLM.

Reconstructed samples	Measured decay mode
$D_s^- e^+$, $D_s^- \mu^+$	$B_s \rightarrow D_s X \ell \nu$ (semi-inclusive)
$D_s^{*-} e^+$, $D_s^{*-} \mu^+$	$B_s \rightarrow D_s^* X \ell \nu$ (semi-inclusive)
$D_s^+ e^+$, $D_s^+ \mu^+$ and D_s	$B_s \rightarrow X \ell \nu$ (inclusive)

Table 5.1: Overview of the reconstructed samples for the semi-inclusive and inclusive measurements of semileptonic B_s decays.

In addition to the $D_s^+ \ell^+$ sample, a sample of D_s^+ mesons without the lepton is reconstructed to determine the number of B_s mesons in the sample.

The reconstructed samples and the measured decay modes are summarised in Table 5.1. The semi-inclusive and inclusive analyses have in common that D_s mesons and $D_s^{(*)} \ell$ pairs are reconstructed and therefore the reconstruction procedures are very similar. The selection procedure of the semi-inclusive analysis is described in the following and the differences for the inclusive analysis differs are discussed at the end of this chapter. The event reconstruction is performed in several steps. First of all, the final state particles ($K^\pm$, $\pi^\pm$, $e^\pm$, $\mu^\pm$, γ) are reconstructed from the information of the different subdetectors. In a second step, intermediate decay products (ϕ, D_s, D_s^*) are reconstructed by combining the final state particles. Eventually, signal candidates are formed.

5.1 Reconstruction of charged kaons and pions

Kaons and pions are reconstructed from charged tracks. Only tracks originating from the interaction point are selected by requiring at least one associated hit in the SVD and the impact parameters in $r\phi$ and z to be $|dr| < 0.5\,\text{cm}$ and $|dz| < 2.0\,\text{cm}$. Low momentum tracks are bent in the magnetic field of the solenoid so much that their trajectory describes a spiral in the detector. Such spiral track can easily be misreconstructed as two separate tracks. To remove such duplicate tracks, the following algorithm is applied: The pion hypothesis is applied to each of two tracks with a transverse momentum of less than 275 MeV. If the difference between the absolute values of the measured momenta is less than

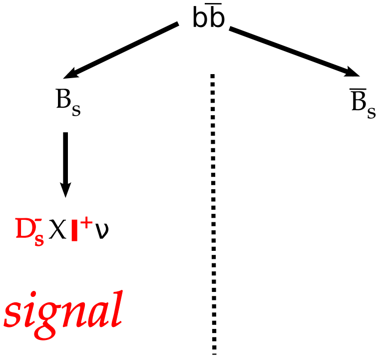

(a) Semi-inclusive analysis.

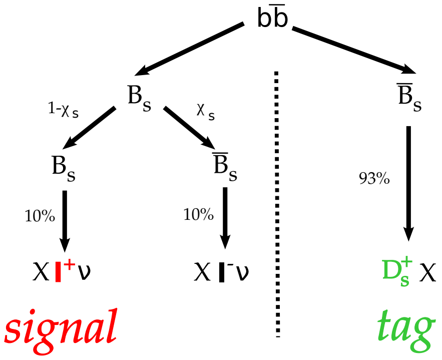

(b) Inclusive analysis.

Figure 5.2: Approaches to study semileptonic B_s decays.

100 MeV, and the angle between the two tracks is less than 15° (same-sign charges) or larger than 165° (opposite-sign charges), the track with the smaller impact parameters, $|dr|$ and $|dz|$, is chosen for the analysis.

Kaons and pions are identified from the Cherenkov light yield in the ACC, the timing information from the TOF and the specific ionisation measured in the CDC. The response of theses detectors is combined into a likelihood, $L_{K,\pi}$, that distinguishes between the kaon and pion hypothesis [95]. The likelihood $L_{K,\pi}$ can take values between 0 and 1, where 0 stands for a high probability that the reconstructed track is a pion and 1 that it is a kaon (see Fig. 5.3). The Belle default requirements for kaons, $L_{K,\pi} > 0.6$, and pions, $L_{K,\pi} < 0.8$, are applied. For a kaon (pion) track with a typical momentum of $p_{K,\pi} = 0.75\,\text{GeV}$, the identification efficiency is about 96 % (92 %), while the probability for pions (kaons) to be misidentified as kaons (pions) is 7 % (2 %).

The kaon and pion identification efficiencies were studied [96] with a sample of reconstructed $D^{+*} \to D^0\pi^+_{\text{slow}}$; $D^0 \to K^-\pi^+$ decays. The charged pion π^+_{slow} from the D^{+*} decay typically has a small momentum because it is produced near threshold. Correctly reconstructed events can be easily recognised because they produce a sharp peak in the distribution of the difference of the reconstructed masses, $m_{K\pi\pi_{\text{slow}}} - m_{K\pi}$. The charge of the slow pion π_{slow} determines the particle species of the other charged tracks. It can then be tested if a kaon or pion track identified via the D^{+*} reconstruction passes the requirement based on the likelihood $L_{K,\pi}$. This test is performed with the data sample divided into bins $j = (p, \theta^{\text{lab}})$ of the kaon (pion) momentum in the lab frame and the kaon (pion) polar angle, respectively. By comparing the event yields obtained from collision data and the MC sample, D_j and M_j, respectively, one derives correction factors for the kaon (pion) efficiencies in the MC simulation:

$$R_j = \frac{D_j}{M_j}\,. \tag{5.1}$$

The difference in kaon and pion identification between the real data and the MC samples is corrected by multiplying each MC event with a weight depending on the number of reconstructed kaons and pions and the detector region where they are detected. For the reconstruction of the decay $D_s^+ \to K^+K^-\pi^+$, the sample is divided in (p, θ^{lab}) bins j, k, l

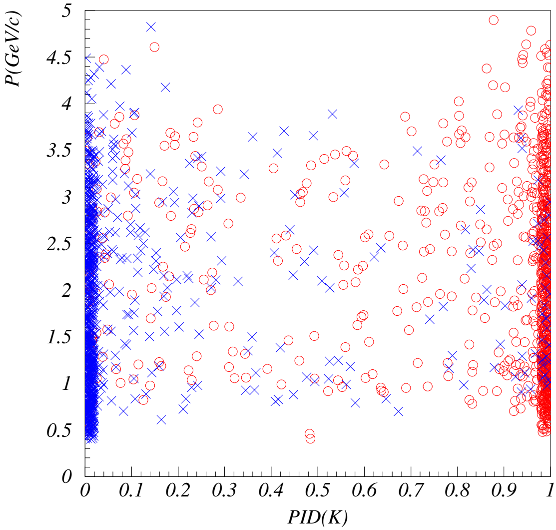

Figure 5.3: Kaon likelihood for kaon (red) and pion (blue) tracks from $D^* \rightarrow D^0\pi^+_{\text{slow}}; D^0 \rightarrow K^-\pi^+$ decays reconstructed in Belle $\Upsilon(4S)$ data. The charge of the slow pion, π^+_{slow}, determines the particle species of the reconstructed tracks. A likelihood $L_{K,\pi} = PID(K) = 1$ stands for a high probability that the reconstructed track is a kaon, and 0 corresponds to a high pion probability. Figure taken from Ref. [48].

corresponding to the K^+, K^-, π^+ tracks, respectively, and the corrected MC expectation N' is calculated from the number of generated events N_{jkl} via

$$N' = \sum_j \sum_k \sum_l R_j R_k R_l N_{jkl} \,. \tag{5.2}$$

The uncertainty of the efficiency correction, ΔR_j, is composed of the statistical uncertainty, $\Delta\ R_{j,\mathrm{stat}}$, of the D^{*+} data and MC samples, and a systematic uncertainty, $\Delta R_{j,\mathrm{syst}}$, due to the determination of the D^{*+} yields and the fact that a potential dependence on the data-taking period is neglected. In the calculation of the total uncertainty of the MC prediction, $\Delta N'$, the statistical uncertainties are treated as uncorrelated between the individual p_h, θ_h^{lab} bins while the systematic uncertainties are treated as fully correlated:

$$\Delta N' = \sqrt{\sum_i \tilde{N}_i^2 \cdot \Delta R_{i,\mathrm{stat}}^2 + \left(\sum_i \tilde{N}_i \cdot \Delta R_{i,\mathrm{syst}}\right)^2} \tag{5.3}$$

with

$$\tilde{N}_i = \sum_i \sum_{j,k,l} \delta_{ij} \delta_{ik} \delta_{il} N_{jkl} R_i \,, \tag{5.4}$$

where δ_{ab} is the Kronecker delta.

5.2 Reconstruction of D_s and D_s^* mesons

The D_s mesons are reconstructed in the decay mode $D_s^+ \to \phi\pi^+$; $\phi \to K^+K^-$, which has a branching fraction of [2.24 ± 0.10] % [8].[2] The reconstruction of the intermediate ϕ resonance is an effective tool to reduce the large combinatorial background from random $K^+K^-\pi^+$ combinations and increase the signal purity of the selected sample because the ϕ resonance is very narrow. The reconstructed di-kaon mass is required

---

[2] The D_s decay modes into $K_S K$ and $K^* K$ were taken into consideration as well, but the corresponding signal-to-background ratios are a factor of 2 to 3 worse than for the $\phi\pi$ mode. Therefore, these modes were discarded.

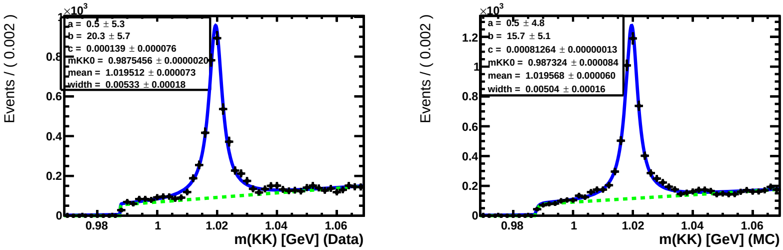

Figure 5.4: Reconstructed K^+K^- mass (black points) for data (left) and MC (right). The blue curve is the result of a fit of the sum of a Breit-Wigner function for the signal and a threshold function for the combinatorial background. The dotted green curve shows the fitted background contribution.

to be within a ± 15 MeV mass window around the nominal ϕ mass of $[1019.455 \pm 0.020]$ MeV [8]. To ensure that the selection efficiency of this mass window is the same for the data and the MC samples, the mass, m_ϕ, and the width, σ_ϕ, of the ϕ mass peak are determined by fitting the sum of a Breit-Wigner and a threshold function[3] to the K^+K^- mass distributions reconstructed in both samples (see Fig. 5.4). The fit results for data and MC are in agreement within the uncertainties:

$$\text{Data:} \quad m_\phi = [1019.51 \pm 0.07]\ \text{MeV}, \quad \sigma_\phi = [5.33 \pm 0.18]\ \text{MeV}, \tag{5.5}$$

$$\text{MC:} \quad m_\phi = [1019.57 \pm 0.06]\ \text{MeV}, \quad \sigma_\phi = [5.04 \pm 0.16]\ \text{MeV}. \tag{5.6}$$

For further background reduction, the helicity angle, θ_{hel}, is used. It is defined in the rest frame of the ϕ meson as the angle between the incoming momentum of the D_s and the negatively charged kaon. Since the decay chain $D_s^+ \to \phi\pi^+;\ \phi \to K^+K^-$ is a scalar-to-vector-scalar transition with the vector meson decaying to two scalars, correctly reconstructed decays preferentially have large $|\cos\theta_{\text{hel}}|$ values, while combinatorial background is uniformly distributed (see Fig. 5.5). Events with $|\cos\theta_{\text{hel}}| > 0.3$ are selected. The selection criteria are op-

---

[3] The function `RooDstD0BG` was originally designed for $D^* \to D^0\pi$ decays. For details see the documentation of the RooFit package [97].

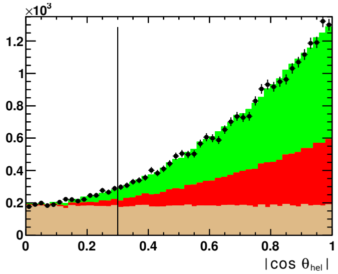

Figure 5.5: The helicity angle distribution of reconstructed $D_s^- \ell^+$; $D_s^- \to \phi(K^+K^-)\pi^-$ candidates. The black points are the 121.4 fb^{-1} $\Upsilon(5S)$ data. The stacked histograms are the MC distributions normalised to the number of data events: misreconstructed D_s (brown), correctly reconstructed D_s (red), correctly reconstructed D_s from $D_s^* \to D_s\gamma$ decays (green). The vertical line represents the threshold set in the $B_s \to D_s^{(*)} X \ell \nu$ analysis.

timised with a figure-of-merit optimisation. As figure-of-merit, $\mathrm{FOM} = S/\sqrt{S+B}$ is chosen. D_s candidates with a reconstructed mass within ±65 MeV around the nominal D_s mass, $m_{D_s} = [1968.50 \pm 0.32]$ MeV [8], are retained for analysis to have large enough side bands for the estimation of the combinatorial background. The reconstructed $K^+K^-\pi^+$ mass distribution is shown in Fig. 5.6 for collision data and the MC sample. The small differences in the shapes and positions of the D_s mass peaks are not relevant for the analyses because the shape of the MC distribution is not used.

The D_s^* candidates are reconstructed in the dominant decay channel $D_s^* \to D_s\gamma$, which has a branching fraction of $[94.2 \pm 0.7]$ % [8]. Only the D_s candidates within a mass window of ±15 MeV around M_{D_s} corresponding to three times the RMS of the D_s mass peak are considered for the D_s^* reconstruction, which removes a large fraction of the combinatorial background from the D_s reconstruction. The chosen mass window is large enough to be insensitive to the small shape differences between the collision data and the MC sample to be seen in Fig. 5.6. The photon candidate is reconstructed from ECL clusters that have not been assigned to a track candidate. It must have a minimum energy of

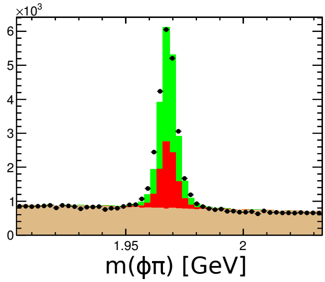

Figure 5.6: Reconstructed D_s mass of $D_s^- \ell^+$; $D_s^- \to \phi(K^+K^-)\pi^-$ candidates. The colour code is explained in Fig. 5.5.

125 MeV in the lab frame. The photon selection is refined using the variable $E9/E25$, defined as the ratio of the energy deposited in the central 3×3 cells of the ECL cluster to the energy contained in the central 5×5 cells. Photon candidates with $E9/E25 > 90\,\%$ are considered for the D_s^* reconstruction. Photons originating from π^0 decays are vetoed by combining each photon candidate with any other photon candidate in the event and excluding both candidates from the analysis if the invariant mass of the di-photon system differs by less than 5 MeV from the nominal π^0 mass, $m_{\pi^0} = [134.9766 \pm 0.0006]$ MeV. The distributions used to select the photon for the D_s^* reconstruction are depicted in Fig. 5.7. For correctly reconstructed D_s^* mesons, the angle between the D_s meson and the photon, $\measuredangle(D_s, \gamma)$, is typically below 90° (see Fig. 5.8) which is used as additional requirement. The mass difference between the reconstructed $D_s^* \to D_s\gamma$ and the D_s candidate,

$$\Delta m = m_{D_s\gamma} - m_{D_s}\,, \tag{5.7}$$

is calculated and candidates with a mass within a ±65 MeV mass window around the nominal value of $\Delta m = [143.8 \pm 0.4]$ MeV are retained for the analysis. The Δm distributions of reconstructed data events and simulated events are shown in Fig. 5.9 (a). The width and the position of the signal peak of the collision data and the simulated data are different with respect to each other. These parameters are, therefore, determined from a fit to the data distribution in the analysis.

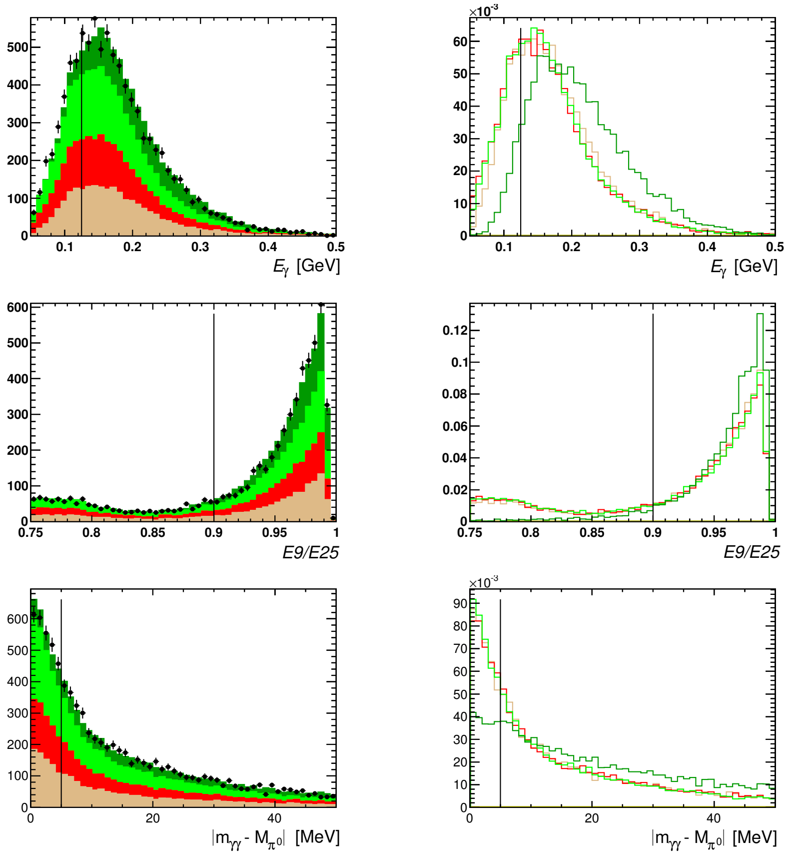

Figure 5.7: Data-MC comparison of the variables used in the photon selection. The selection criteria are represented by vertical lines. For every distribution, each other selection criterion is applied. The distributions are from top to bottom: photon energy, E_γ, in the lab frame; E9/E25 (for the definition see text); difference between the reconstructed di-photon mass and the nominal π^0 mass. The left column shows the sum of the MC expectation scaled to the number of data events. The right column shows the shapes of the variables normalised to unity. The colour code is explained in Fig. 5.5. Additionally, events are distinguished where the D_s^* (dark green) was correctly reconstructed and where the D_s was correctly reconstructed, but not the D_s^* (light green).

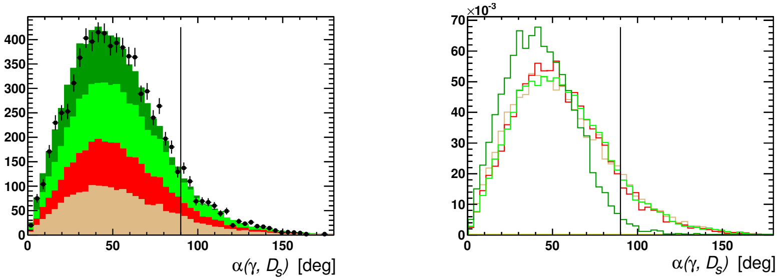

Figure 5.8: Data-MC comparison of the angle between the D_s and the photon in the lab frame, $\measuredangle(D_s, \gamma)$, for reconstructed D_s^* candidates. The photon selection criteria presented in Fig. 5.7 are applied. Left: sum of the MC expectations scaled to the number of data events. Right: shapes of the individual contributions normalised to unity. The vertical line represents selection criterion applied in the analysis. The colour code is explained in Figs. 5.5 and 5.7.

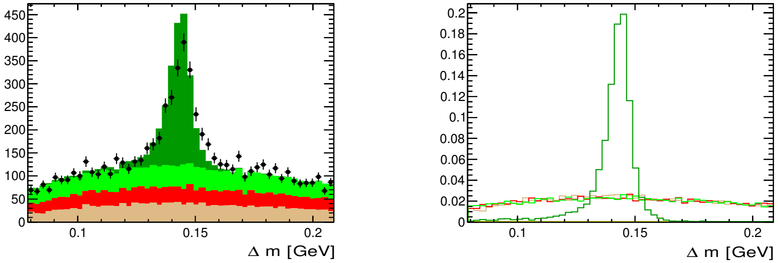

(a)

(b)

Figure 5.9: Mass difference, $\Delta m = m_{D_s^*} - m_{D_s}$, between the reconstructed D_s^* and D_s candidates. Left: Data-MC comparison. Right: Shape comparison of the different components of the Δm distribution. The colour code is explained in Figs. 5.5 and 5.7.

5.3 Lepton reconstruction

Electron and muon candidates are reconstructed from charged tracks selected by the same procedure as kaon and pion tracks (see Sec. 5.1). Only the tracks that are not used for the D_s reconstruction are considered. The lepton momentum measured in the laboratory frame is required to be larger than 0.9 GeV in order to suppress backgrounds from secondary decays and misidentified hadrons, which have typically lower momenta than leptons from semileptonic $B_{(s)}$ decays (cf. Sec. 7.1). Electrons are selected based on a likelihood, L_e, derived from five measured quantities [98]:

1. **Position matching between track and ECL cluster:** The position resolution for electron showers is smaller than for hadronic showers. By taking the difference between the position of the track extrapolated to the ECL and the measured position of the ECL cluster, a discriminating variable is formed.

2. **Ratio of the energy measured in the ECL and the charged-track momentum:** The small electron mass leads to a ratio $E_{\mathrm{ECL}}/p_{\mathrm{track}} \approx 1$ while for hadrons this ratio is significantly smaller.

3. **Transverse ECL shower shape:** For electrons, the variable $E9/E25$ peaks at $E9/E25 = 0.95$. For hadrons, there are two possibilities: either $E9/E25$ equals to 1 because the full energy is deposited in a single ECL cell or the $E9/E25$ value is below 0.95.

4. **Specific ionisation in the CDC:** The measured specific ionisation $\mathrm{d}E/\mathrm{d}x$ and its resolution are compared to the expected values.

5. **ACC light yield:** The measured ACC light yield allows for a separation of electrons and pions with track momenta below 1 GeV, as the Cherenkov threshold for electrons is only a few MeV, while it is between 0.5 GeV and 1.0 GeV for pions.

The acceptance region for electrons is $18 \ldots 150\,^{\circ}$. Tracks are considered as electrons if they have a likelihood of $L_e > 0.5$. The electron efficiency for track momenta above 0.9 GeV is better than 89 %. The misidentification probabilities for kaons and pions are below 1 %.

The identification of muons relies exclusively on the information from the KLM [99]. Adopting the muon hypothesis, each track is extrapolated from the CDC to the KLM and associated hits are looked for. If hits are found in at least two superlayers of the KLM the expected penetration depth defined as the outermost layer with an RPC hit is calculated. If the discrepancy between the measured and the expected penetration depth is not more than five layers, the track is accepted as muon candidate. These vetoes already reject 90 % of the pion tracks, but retain 95.5 % of the muons. After that, a layer-by-layer extrapolation is performed with GEANT [92]. The goodness of fit of the transverse deviations and the difference between the measured and expected penetration depth is used to assign a muon likelihood L_μ. The KLM has an acceptance region of 25 … 145 °. Muon tracks with momenta above 0.9 GeV are identified with an efficiency of more than 82 % for $L_\mu > 0.9$. The probability for kaons and pions to be misidentified as muon is below 2 %.

The lepton efficiencies in the MC simulation are calibrated with events from two photon processes $e^+e^- \to e^+e^-\ell^+\ell^-$ [100]. Similar to the calibration of the kaon and pion efficiencies, data-MC ratios R_j are determined in bins $j = p_{ell}, \theta_\ell^{\text{lab}}$. The MC efficiency of the reconstructed lepton is corrected according to the formula

$$N' = \sum_j R_j \cdot N_j\,, \tag{5.8}$$

where N_j is the number of generated events found in bin j. There are different sources of uncertainty to the ratios R_j: the statistical uncertainty, $\Delta R_{j,\text{stat}}$, of the collision data and the simulated data in the individual bins j, and the systematic uncertainty, $\Delta R_{j,\text{syst}\,1}$, due to the run-period dependence. Moreover, the impact of the particle multiplicity in a hadronic environment on the lepton efficiencies is studied with a $J/\psi \to \ell^+\ell^-$ sample and the difference, $\Delta R_{j,\text{syst}\,2}$, to the $e^+e^- \to e^+e^-\ell^+\ell^-$ sample is considered as additional systematic uncertainty. In the calculation of the total lepton identification uncertainty,

$\Delta N'$, the statistical uncertainties are treated as uncorrelated and the systematic uncertainties as correlated:

$$\Delta N' = \sqrt{\sum_j N_j^2 \cdot \Delta R_{j,\mathrm{stat}}^2 + \left(\sum_j N_j \cdot \Delta R_{j,\mathrm{syst\,1}}\right)^2 + \left(\sum_j N_j \cdot \Delta R_{j,\mathrm{syst\,2}}\right)^2}\,. \tag{5.9}$$

The misidentification probabilities for a kaon (pion) track to be accepted as lepton candidate are studied with the D^{+*} sample mentioned in Sec. 5.1 [101]. The sample is divided into bins of equal size in $j = p_\ell, \theta_\ell^{\mathrm{lab}}$, as for the lepton efficiency studies, and the probabilities that a kaon (pion) passes the chosen L_e or L_μ criterion are determined. The statistical uncertainties of this study are evaluated and considered later in the measurements.

To veto leptons from J/ψ decays, each lepton candidate, ℓ^+, is combined with any other track of the opposite charge, h^-, and excluded from the analysis if $|m_{\ell^+h^-} - m_{J/\psi}| < 5\,\mathrm{MeV}$. Moreover, electron candidates are rejected if they are likely to stem from a photon conversion, $m_{e^+h^-} < 100\,\mathrm{MeV}$, or a Dalitz π^0 decay, $|m_{e^+h^-\gamma} - m_{\pi^0}| < 32\,\mathrm{MeV}$, where γ is any accepted photon candidate.

5.4 Continuum suppression

The reconstruction of D_s mesons leads to a strong suppression of background from continuum processes, $e^+e^- \to q\bar{q}$ with $q = u, d, s$. However, in the case $q = c$, one of the c-quark can hadronise into a D_s meson. This background represents a sizeable contribution to the sample of selected $D_s^{(*)}\ell$ candidates. The D_s mesons from this background stems directly from the hadronisation of a c quark produced in the e^+e^- collision, whereas the D_s from $B_{(s)}$ decays are produced via an intermediate step:

$$\begin{array}{lllllll} e^+e^- & \to & c\bar{c} & \to & D_sX & & \\ e^+e^- & \to & b\bar{b} & \to & B_sX & \to & D_sX'X\,. \end{array} \tag{5.10}$$

Therefore, the D_s from $c\bar{c}$-continuum have significantly higher momenta than the ones from $B_{(s)}$ decays. For an easier comparison of the D_s

momenta in $\Upsilon(5S)$ data and off-resonance data, the reconstructed D_s momentum is divided by the maximum achievable D_s momentum in direct production:

$$x(D_s) = \frac{p^*_{D_s}}{\sqrt{s/4 - M^2_{D_s}}} . \tag{5.11}$$

The obtained variable is independent of the centre-of-mass energy. As the $B_{(s)}$ meson carries away at most half of the available centre-of-mass energy, the criterion $x(D_s) < 0.5$ retains practically all $B_{(s)}$ decays, but removes a large fraction of the $c\bar{c}$-continuum background. Figure 5.10 illustrates the separation power of $x(D_s)$.

To further suppress continuum background, the topology of the event is analysed. While the continuum events have a di-jet-like topology, $B_{(s)}$ pairs decay nearly at rest in the rest frame of the $\Upsilon(5S)$ resonance, leading to an isotropic event topology. The event topology is characterised by the angle θ_{thrust} between the two thrust axes defined as follows: the signal thrust axis $\vec{T}_{\text{sig}}$, points in the direction that maximises the longitudinal momentum of the signal tracks

$$\sum_i \vec{T}_{\text{sig}} \cdot \vec{p}^{\,*}_{\text{sig},i} , \tag{5.12}$$

where $\vec{p}^{\,*}_{\text{sig},i}$ is the momentum in the $\Upsilon(5S)$ rest frame of the i-th signal track; the thrust axis of the rest of the event, $\vec{T}_{\text{rest}}$, is calculated in the same way from the remaining tracks and clusters in the event. The "jet-like" topology of continuum events leads to a peak of the $|\cos\theta_{\text{thrust}}|$ at 1, whereas the spherical topology of $B_{(s)}$ pair events produces a uniform $|\cos\theta_{\text{thrust}}|$ distribution (see Fig. 5.10). For the analysis, the requirement $|\cos\theta_{\text{thrust}}| < 0.8$ is applied.

5.5 Best-candidate selection

After the selection of $D_s^- \ell^+$ pairs, 7.9 % (0.4 %) of the selected events contain more than one (two) $D_s^- \ell^+$ candidates. If there are multiple D_s candidates, a vertex fit of the $K^+K^-\pi^+$ tracks is performed for each can-

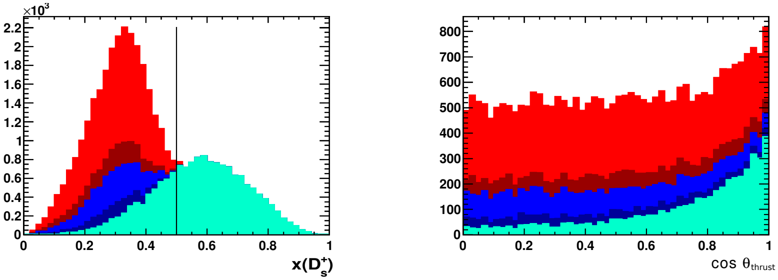

(a) (b)

Figure 5.10: Continuum suppression variables in the MC simulation: (a) $x(D_s)$ and (b) $|\cos\theta_{\text{thrust}}|$ after applying the $x(D_s) < 0.5$ requirement. The stacked histograms represent the following MC contributions from bottom to top: continuum (light blue), leptons from secondary processes and misidentified hadrons (dark blue) and prompt leptons (red). The darker colour is for the B events, and the lighter for the B_s events.

didate and the one with the best χ^2 value of the fit is chosen for the analysis. This procedure selects in 80 % of the cases a correct D_s candidate. The selected best D_s candidate is considered in the following for D_s^* reconstruction. In 36.2 % (9.7 %) of the events, more than one (two) photon candidate(s) form together with a D_s candidate a D_s^* candidate. In this case, the photon candidate with the highest $E9/E25$ value is chosen. Sometimes it happens, that two different photon candidates deposit all of their energy in the central 3×3 cells of an ECL cluster, i.e. $E9/E25 = 1$ for both candidates. For those events, the photon candidate with the higher energy in the lab frame is selected. The described approach to select the photon candidate is marginally better than a random selection. The fraction of events with more than one lepton candidate after selecting the best $D_s^{(*)}$ candidate is relatively small (2.1 %) and a random lepton candidate is selected.

5.6 Event reconstruction in the $B_s \to X\ell\nu$ analysis

As mentioned before, the reconstruction procedure of the inclusive $B_s \to X\ell\nu$ analysis differs only in few points from the one of the semi-inclusive $B_s \to D_s^{(*)}X\ell\nu$ analysis. Since in the combinatorial background in the D_s sample is larger than in the $D_s\ell$ samples, the mass window for the reconstruction of the intermediate ϕ resonance in the decay $D_s^+ \to \phi\pi^+; \phi \to K^+K^-$ is chosen as ± 8 MeV, i.e. tighter than in the $B_s \to D_s^{(*)}X\ell\nu$ analysis. Moreover, a stricter requirement on the helicity angle is used: $|\cos\theta_{\text{hel}}| > 0.5$. The lepton momentum threshold is lowered to $p_\ell > 0.6\,\text{GeV}$ in order to include a larger fraction of the inclusive lepton momentum spectrum in the analysis. The thrust angle, $|\cos\theta_{\text{thrust}}|$, cannot be used for continuum suppression because the signal lepton and the "tag" D_s meson stem from the decay of different B_s mesons and the remaining tracks and ECL cluster cannot be unambiguously assigned to the signal or tag B_s decay. Other event-topology-based continuum suppression variables which do not rely on the reconstruction of the signal B_s, such as the normalised second Fox-Wolfram momentum [102], are not used in order to avoid model dependencies due to differences in the topology of signal events between the data and the MC simulation. No best-candidate selection is performed – the small fraction of events with multiple $D_s \to \phi\pi$ decays is taken into account by the efficiencies. The differences between the selection criteria of the $B_s \to D_s^{(*)}X\ell\nu$ and the $B_s \to X\ell\nu$ analyses are summarised in Table 5.2.

	Semi-inclusive	Inclusive
ϕ mass window	± 15 MeV	± 8 MeV
$\lvert\cos\theta_{\mathrm{hel}}\rvert$	> 0.3	> 0.5
p_ℓ	> 0.9 GeV	> 0.6 GeV
$\lvert\cos\theta_{\mathrm{thrust}}\rvert$	< 0.8	—
Best candidate selection	yes	no

Table 5.2: Differences in the selection between the inclusive and the exclusive analysis.

CHAPTER 6

Semi-inclusive studies: $B_s \to D_s^{(*)} X \ell \nu$

One of the main goals of studying semileptonic B_s decays is the determination of the CKM matrix element $|V_{cb}|$, based on the study of exclusive $B_s \to D_s^{(*)} \ell \nu$ decays, similar to the studies performed with B decays (cf. 2.4.4). However, there are currently still systematic limitations that prohibit such exclusive B_s measurements at Belle — the details will be explained later in this chapter. Therefore, "semi-inclusive" analyses are performed instead of exclusive ones: the decay modes $B_s \to D_s X \ell \nu$ and $B_s \to D_s^{*} X \ell \nu$ are studied, where the X stands for additional particles that can contribute to the final state. These studies already constrain the sum of the different exclusive branching fractions and thus provide implicitly a first test of the predicted exclusive branching fractions. Moreover, they help to identify the challenges of exclusive measurements. Semi-inclusive measurements of $B \to D^{(*)} X \ell \nu$ decays were recently performed at Belle to gain a deeper understanding of $B \to D^{**} \ell \nu$ cross-feed in exclusive $B \to D^{(*)} \ell \nu$ measurements [103]. The measurements of semi-inclusive B_s decays can provide similar insight once the exclusive decays are measured.

The expected $B_s \to D_s X \ell \nu$ branching fraction can be estimated as the difference between the inclusive charmed semileptonic branching fraction, $\mathcal{B}(B_s \to X_c \ell \nu)$, and the branching fraction of charmed semileptonic B_s decays to final state not containing a D_s meson, $\mathcal{B}(B_s \to \not{D}_s X \ell \nu)$.

Using the theory prediction of small SU(3)$_{\text{flavour}}$ symmetry breaking effects (cf. Eq. 2.80) and the measured lifetimes of the B_s and B^0 mesons, τ_{B_s} and τ_{B^0}, one obtains [8]:

$$\mathcal{B}_{\text{est}}(B_s \to X_c \ell \nu) = \frac{\Gamma_{\text{sl}}(B_s)}{\Gamma_{\text{sl}}(B^0)} \cdot \frac{\tau_{B_s}}{\tau_{B^0}} \mathcal{B}(B^0 \to X_c \ell \nu) = [10.0 \pm 0.4]\ \%\,. \quad (6.1)$$

To estimate $\mathcal{B}(B_s \to \not{D}_s X \ell \nu)$, the two modes with a $D_{s1}(2536)$ or a $D_{s2}(2573)$ meson in the final state are considered. Both of these states are above the $D^{(*)}K$ threshold and therefore it can be assumed that they decay with high probability to $D^{(*)}K$: $\mathcal{B}(D_{s1}(2536) \to D^{(*)}K) = \mathcal{B}(D_{s2}(2573) \to D^{(*)}K) = [90 \pm 10]\ \%$. The corresponding semileptonic branching fractions are taken from the prediction by Faustov and Galkin [29]. This leads to the estimate

$$\mathcal{B}(B_s \to \not{D}_s \ell \nu X) = [1.4 \pm 0.2]\ \%\,, \quad (6.2)$$

from which follows

$$\mathcal{B}_{\text{est}}(B_s \to D_s X \ell \nu) = \mathcal{B}_{\text{est}}(B_s \to X_c \ell \nu) - \mathcal{B}(B_s \to \not{D}_s X \ell \nu) = (8.6 \pm 0.5)\%\,. \quad (6.3)$$

The LHCb and D0 experiments have measured the branching fractions with a $D_{s1}(2536)$ or a $D_{s2}(2573)$ meson in the final state (cf. Table 1.1). These measurements, reconstruct the decay $B_s \to D_s X \ell \nu$ and then use an estimate of $\mathcal{B}(B_s \to D_s X \ell \nu)$ to determine number of B_s mesons in their data. Therefore, they cannot be considered for the calculation of $\mathcal{B}_{\text{est}}(B_s \to D_s X \ell \nu)$.

6.1 Analysis overview

The semi-inclusive measurements are based on samples of $D_s^- \ell^+$ and $D_s^{*-} \ell^+$ pairs, where the D_s^- meson is reconstructed in the channel $D_s^- \to \phi\pi^-$; $\phi \to K^+K^-$ and the D_s^{*-} meson in the channel $D_s^{*-} \to D_s^- \gamma$ as described in the preceding chapter. The yields of correctly reconstructed D_s^- and D_s^{*-} decays are determined from fits to the $m_{KK\pi}$ and $\Delta m = m_{D_s\gamma} - m_{D_s}$ distributions, respectively. The $D_s^{(*)-}\ell^+$ samples where the $D_s^{(*)}$ is correctly reconstructed contain miscellaneous signal and background contributions:

1. **Continuum** background from the process $e^+e^- \to c\bar{c}$;
2. $B \to D_s^{(*)} K \ell \nu$ decays;
3. **Wrong-side** combinatorial background where the lepton candidate is paired with a $D_s^{(*)}$ from the other $B_{(s)}$ in the event. The lepton candidate can be either a primary lepton coming directly from a $B_{(s)}$ decay, a secondary leptons stemming from the decay of a $B_{(s)}$ decay product, or a hadron misidentified as a lepton;
4. **Other** backgrounds where a $D_s^{(*)}$ meson is combined with either a secondary lepton or a misidentified hadron from the decay of the same $B_{(s)}$ meson;
5. **Signal** decays. The $D_s^- \ell^+$ sample contains $B_s \to D_s \ell \nu$ and $B_s \to D_s^* \ell \nu$ as well as $B_s \to D_s^{**} \ell \nu$ decays where the D_s^{**} meson decays to a D_s meson. The $D_s^{*-}\ell^+$ sample comprises $B_s \to D_s^* \ell \nu$ decays as well as $B_s \to D_s^{**} \ell \nu$ decays where the D_s^{**} meson decays to a D_s^* meson.

The expected yields of each component at the different steps of the selection are listed in Tables 6.1 and 6.2 for the $D_s^- \ell^+$ samples, and in Table 6.3 and 6.4 for the $D_s^{*-}\ell^+$ samples. The continuum background (1) is estimated from the off-resonance data sample and subtracted from the selected data sample. The small amount of $B \to D_s^{(*)} K \ell \nu$ decays (2) is estimated from a dedicated MC sample. The yields of the remaining

	Fake D_s	Continuum	WS primary	WS other	Other	$B \to D_s K \ell \nu$	$B_s \to D_s \ell \nu$	$B_s \to D_s^* \ell \nu$	$B_s \to D_s^{**} \ell \nu$
Generated							6602	16542	1733
Reconstructed	117986	16688	5714	4200	3517	154	1786	4379	449
$x(D_s) < 0.5$	110143	5579	5707	4193	3515	153	1769	4378	449
$\lvert\cos\theta_{\text{thrust}}\rvert < 0.8$	68813	3270	4735	3432	2844	125	1415	3481	357
$\lvert\cos\theta_{\text{hel}}\rvert > 0.3$	48520	3158	4574	3312	2745	121	1365	3362	345
$p_\ell > 0.9$	19877	1080	3964	775	788	70	1158	3041	281
Best $D_s \ell$	18115	1046	3688	711	727	66	1094	2848	267
$x(D_s) < 0.5$	93%	33%	100%	100%	100%	100%	99%	100%	100%
$\lvert\cos\theta_{\text{thrust}}\rvert < 0.8$	58%	20%	83%	82%	81%	82%	79%	79%	80%
$\lvert\cos\theta_{\text{hel}}\rvert > 0.3$	41%	19%	80%	79%	78%	79%	76%	77%	77%
$p_\ell > 0.9$	17%	6%	69%	18%	22%	46%	65%	69%	63%
Best $D_s \ell$	15%	6%	65%	17%	21%	43%	61%	65%	59%

Table 6.1: Impact of the selection criteria on the different contributions in the $D_s^- e^+$ sample (see Sec. 6.1 for an explanation of the contributions). The numbers are the expectation from the MC simulation after applying all calibration factors. The lower part of the Table lists the fraction of the reconstructed events retained after each selection step.

	Fake D_s	Continuum	WS Primary	WS other	Other	$B \to D_s K \ell \nu$	$B_s \to D_s \ell \nu$	$B_s \to D_s^* \ell \nu$	$B_s \to D_s^{**} \ell \nu$
Generated							6595	16534	1754
Reconstructed	103265	12974	5021	2600	2313	108	1618	3905	398
$x(D_s) < 0.5$	95198	4152	5016	2596	2309	108	1603	3904	398
$\lvert\cos\theta_{\text{thrust}}\rvert < 0.8$	55527	2258	4177	2116	1882	89	1296	3124	318
$\lvert\cos\theta_{\text{hel}}\rvert > 0.3$	39086	2177	4035	2043	1828	86	1255	3024	307
$p_\ell > 0.9$	26756	1412	3766	1186	1106	66	1157	2876	278
Best $D_s\ell$	24530	1363	3505	1072	1018	63	1088	2711	262
$x(D_s) < 0.5$	92%	32%	100%	100%	100%	100%	99%	100%	100%
$\lvert\cos\theta_{\text{thrust}}\rvert < 0.8$	54%	17%	83%	81%	81%	82%	80%	80%	80%
$\lvert\cos\theta_{\text{hel}}\rvert > 0.3$	38%	17%	80%	79%	79%	79%	78%	77%	77%
$p_\ell > 0.9$	26%	11%	75%	46%	48%	62%	72%	74%	70%
Best $D_s\ell$	24%	11%	70%	41%	44%	58%	67%	69%	66%

Table 6.2: Impact of the selection criteria on the different contributions in the $D_s^-\mu^+$ sample (see Sec. 6.1 for an explanation of the contributions). The numbers are the expectation from the MC simulation after applying all calibration factors. The lower part of the Table lists the fraction of the reconstructed events retained after each selection step.

	Fake D_s	Fake D_s^*	Continuum	WS primary	WS other	Other	$B \to D_s K\ell\nu$	$B_s \to D_s^*\ell\nu$	$B_s \to D_s^{**}\ell\nu$
Generated								15589	385
Reconstructed	427120	102746	7852	2382	1738	1392	50	2937	71
$x(D_s) < 0.5$	409593	83560	2660	2382	1737	1391	50	2936	71
$\lvert\cos\theta_{\text{thrust}}\rvert < 0.8$	264604	64871	1561	1971	1414	1127	40	2332	56
$\lvert\cos\theta_{\text{hel}}\rvert > 0.3$	186688	62633	1509	1913	1368	1093	39	2255	55
$p_\ell > 0.9$	74047	35657	518	1664	315	306	22	2035	46
Best $D_s\ell$	67669	33688	501	1545	288	281	20	1907	44
Photon selection	3541	6494	292	805	137	136	10	976	19
Best photon	2358	4201	231	617	99	102	7	711	14
$x(D_s) < 0.5$	96%	81%	34%	100%	100%	100%	100%	100%	71 100%
$\lvert\cos\theta_{\text{thrust}}\rvert < 0.8$	62%	63%	20%	83%	81%	81%	81%	79%	79%
$\lvert\cos\theta_{\text{hel}}\rvert > 0.3$	44%	61%	19%	80%	79%	79%	79%	77%	77%
$p_\ell > 0.9$	17%	35%	7%	70%	18%	22%	44%	69%	66%
Best $D_s\ell$	16%	33%	6%	65%	17%	20%	42%	65%	62%
Photon selection	1%	6%	4%	34%	8%	10%	20%	33%	28%
Best photon	1%	4%	3%	26%	6%	7%	15%	24%	20%

Table 6.3: Impact of the selection criteria on the different contributions in the $D_s^{*-}e+$ samples (see Sec. 6.1 for an explanation of the contributions). The numbers are the expectation from the MC simulation after applying all calibration factors. The lower part of the Table lists the fraction of the reconstructed events retained after each selection step.

	Fake D_s	Fake D_s^*	Continuum	Prompt WS	Other WS	Other CS	$B \to D_s K \ell \nu$	$B_s \to D_s^* \ell \nu$	$B_s \to D_s^{**} \ell \nu$
Generated								15565	387
Reconstructed	352864	78481	6141	2101	1094	925	36	2674	61
$x(D_s) < 0.5$	335836	63587	1995	2100	1094	923	36	2673	61
$\|\cos\theta_{\text{thrust}}\| < 0.8$	203609	49112	1062	1742	888	751	29	2142	49
$\|\cos\theta_{\text{hel}}\| > 0.3$	143520	47469	1026	1689	862	730	28	2080	47
$p_\ell > 0.9$	97471	37709	667	1568	502	445	21	1981	43
Best $D_s \ell$	89500	35578	643	1454	455	414	20	1867	41
Photon selection	4591	6844	384	731	227	209	9	955	19
Best photon	3095	4425	298	553	167	151	6	698	14

$x(D_s) < 0.5$	95%	81%	32%	100%	100%	100%	100%	100%	100%
$\|\cos\theta_{\text{thrust}}\| < 0.8$	58%	63%	17%	83%	81%	81%	81%	80%	81%
$\|\cos\theta_{\text{hel}}\| > 0.3$	41%	60%	17%	80%	79%	79%	77%	78%	78%
$p_\ell > 0.9$	28%	48%	11%	75%	46%	48%	59%	74%	71%
Best $D_s \ell$	25%	45%	10%	69%	42%	45%	55%	70%	68%
Photon selection	1%	9%	6%	35%	21%	23%	25%	36%	32%
Best photon	1%	6%	5%	26%	15%	16%	17%	26%	24%

Table 6.4: Impact of the selection criteria on the different contributions in the $D_s^{*-}\mu^+$ sample (see Sec. 6.1 for an explanation of the contributions). The numbers are the expectation from the MC simulation after applying all calibration factors. The lower part of the Table lists the fraction of the reconstructed events retained after each selection step.

Channel	$B_s \to D_s \ell \nu$	$B_s \to D_s^* \ell \nu$	$B_s \to D_s^{**} \ell \nu$
$D_s X e \nu$	$(16.6 \pm 0.2)\%$	$(17.2 \pm 0.1)\%$	$(15.4 \pm 0.4)\%$
$D_s X \mu \nu$	$(16.5 \pm 0.2)\%$	$(16.4 \pm 0.1)\%$	$(14.9 \pm 0.4)\%$
$D_s^* X e \nu$	—	$(4.6 \pm 0.1)\%$	$(3.6 \pm 0.4)\%$
$D_s^* X \mu \nu$	—	$(4.5 \pm 0.1)\%$	$(3.7 \pm 0.4)\%$

Table 6.5: Signal efficiencies of the different semileptonic decay modes for the studied semi-inclusive decay channels.

three components (3-5) are estimated from kinematic distributions. The kinematic variables are calculated in the centre-of-mass frame of the e^+e^- collision. In this reference system, the B_s meson is approximately at rest as its typical momentum is only $p^*_{B_s} \approx 0.43\,\mathrm{GeV}$[1]. The analysis uses two variables: the lepton momentum, p^*_ℓ, and the variable

$$X_{\mathrm{mis}} = \frac{\sqrt{s/4} - (E^*_{\mathrm{vis}} + p^*_{\mathrm{vis}})}{\sqrt{s/4 - m^2_{B_s}}}\,, \tag{6.4}$$

where $p^*_{\mathrm{vis}} = |\vec{p}^*_\ell + \vec{p}^*_{D_s^{(*)}}|$ is the sum of the lepton and $D_s^{(*)}$ momenta, and $E^*_{\mathrm{vis}} = |E^*_\ell + E^*_{D_s^{(*)}}|$ is sum of the lepton and $D_s^{(*)}$ energies. Figure 6.1 shows the X_{mis} and the p^*_ℓ distributions for simulated $D_s^- e^+$ events. The samples of reconstructed $D_s^{(*)-}\ell^+$ candidates are divided according to these variables into three "counting regions", which are each enhanced in one of the three components (3-5):

Region	Selection		Remark
A	$X_{\mathrm{mis}} < -1$		Exclusively *wrong-side* combinations
B	$X_{\mathrm{mis}} \geq -1$	$p^*_\ell < 1.4\,\mathrm{GeV}$	*Other* background enhanced
C	$X_{\mathrm{mis}} \geq -1$	$p^*_\ell \geq 1.4\,\mathrm{GeV}$	*Signal* enhanced

---

[1] The "$*$" will denote in the following that a variable is calculated in the e^+e^- centre-of-mass frame.

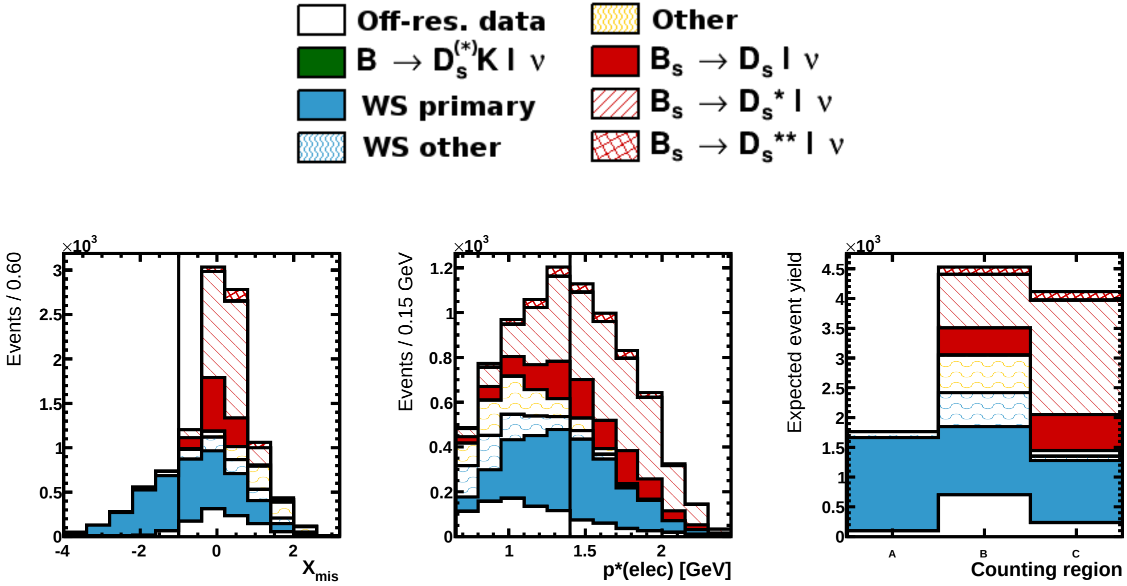

Figure 6.1: Illustration of the three counting regions with simulated $D_s^- e^+$ events. From left to right: X_{mis} distribution of the full sample; p_e^* distribution of the subsample with $X_{\text{mis}} \geq -1$; expected event yields for the three counting regions. The vertical lines represent the boundaries of the counting regions. The small $B \to D_s K \ell \nu$ component is omitted in the distributions shown in this Figure.

As the region A is exclusively populated with events from the *wrong-side* component, the normalisation of this background can be extracted by measuring the event yield in this region. The regions B and C contain all three contributions (3-5). Since the the primary leptons from semileptonic B_s decays have significantly higher momenta compared to secondary leptons and misidentified hadrons, region C is enhanced in *signal* decays while region B is enhanced in the *other* background. The boundary $p_\ell^* = 1.4\,\mathrm{GeV}$ between regions B and C is chosen such that the expected event yields are equal in both regions. The measurement of the $D_s^{(*)}$ yields in the three differently populated counting regions allows to determine the $B_s \to D_s^{(*)} X \ell \nu$ signal yields, N_{sig}, in the data. The semi-inclusive branching fractions can be then extracted using the relation

$$\mathcal{B}(B_s \to D_s^{(*)} X \ell \nu) = \frac{N_{\mathrm{sig}}}{\epsilon_{D_s^{(*)}} \cdot \mathcal{B}_{D_s^{(*)}} \cdot 2 \cdot N_{B_s \bar{B}_s}}\,, \qquad (6.5)$$

where $\epsilon_{D_s^{(*)}}$ are the efficiencies, $N_{B_s \bar{B}_s}$ is the number of B_s pairs contained in the $\Upsilon(5S)$ sample (cf. Eq. 4.10) and $\mathcal{B}_{D_s^{(*)}}$ are the branching fractions of the reconstructed $D_s^{(*)}$ decay modes [8].

6.2 The variable X_{mis}

In the following, the variable X_{mis} defined in Eq. 6.4 is discussed in more detail, since it plays a key role in the extraction of the signal yield. The core piece of X_{mis} is the sum $E^*_{\mathrm{vis}} + p^*_{\mathrm{vis}}$. In the approximation that the centre-of-mass frame of the e^+e^- collision is identical to the rest frame of the decaying B_s meson, the momentum of the unreconstructed neutrino is given by

$$|p_\nu^*| \equiv p_\nu^* = p^*_{\mathrm{vis}} \equiv |\vec{p}_\ell^{\,*} + \vec{p}^{\,*}_{D_s^{(*)}}|\,. \qquad (6.6)$$

Neglecting the tiny neutrino mass, the neutrino momentum equals the neutrino energy:

$$E_\nu^* = p_\nu^* = p^*_{\mathrm{vis}}\,. \qquad (6.7)$$

The sum of the visible energy and the visible momentum gives thus for correctly reconstructed events the B_s mass:

$$E^*_{\text{vis}} + p^*_{\text{vis}} = E^*_\ell + E^*_{D_s^{(*)}} + E^*_\nu = E^*_{B_s} = m_{B_s} \,. \tag{6.8}$$

The other terms in the definition of X_{mis} correct for small, run-depended variations of the centre-of-mass energy, $\sqrt{s}$. They also shift the B_s mass peak to zero and normalise the width of the peak. The width of the peak is determined by the non-zero momentum of the B_s meson in the e^+e^- centre-of-mass frame.

In some events, the final state hadron is only partially reconstructed. For example, in the $B_s \to D_s X \ell \nu$ channel, the decay $B_s \to D_s^* \ell \nu$; $D_s^* \to D_s \gamma$ contributes to the signal yield; the photon from the D_s^* decays is, however, not reconstructed, i.e. $X = \gamma$. In such cases, the signal peak is shifted to positive values in X_{mis} depending on the mass difference between the final state hadron of the semileptonic decay (in the example: D_s^*) and the reconstructed part (in the example: D_s). Therefore, the peaks of individual signal contributions ($D_s \ell \nu$, $D_s^* \ell \nu$ and $D_s^{**} \ell \nu$) are shifted with respect to each other. This could in principle be used to extract the normalisation of the individual contributions from a fit to the measured X_{mis} distribution. Currently, the feasibility of such measurements is limited by the precision of the input parameters defining the exact shape of each signal component. Figure 6.2 (a) shows the data-MC comparison of the X_{mis} distribution. A clear disagreement can be observed: the χ^2 probability is $\approx 10^{-9}$. This disagreement can be of course due to a wrong modelling of the signal composition ($D_s \ell \nu$, $D_s^* \ell \nu$ and $D_s^{**} \ell \nu$) in the simulation. Therefore, a fit of normalisations of the individual signal contributions is performed. This improves the agreement, but the χ^2 probability of the result is still below 10^{-3}. This means that other parameters than the signal composition have to be responsible for the observed disagreement. On closer inspection, one sees that the width of the signal peak in data is smaller with respect to the MC distribution. One parameter determining the width of the signal peak is the B_s momentum, $p^*_{B_s}$, which found to be strongly influenced by the B_s^* mass. In the simulation, the value $m_{B_s^*} = 5412.0\,\text{MeV}$ is used, which is slightly smaller than the world average, $m_{B_s^*} = (5415.4^{+2.4}_{-2.1})$ MeV. This has a large impact on $p^*_{B_s^*}$ because the mass difference $m_{B_s^*} - m_{B_s} = \left[48.7\,^{+2.3}_{-2.1}\right]$ MeV [8] is small. The relation between the B_s^* mass and the B_s momentum is illustrated in Fig. 6.3. Considering only the dominant B_s production mode at the $\Upsilon(5S)$ resonance, $B_s^* \bar{B}_s^*$ (cf. Eq. 4.13), one can calculate

$$p^*_{B_s} \approx p^*_{B_s^*} = \sqrt{s/4 - m^2_{B_s^*}}\,. \tag{6.9}$$

If one compares the value of $p^*_{B_s^*}$ calculated with the world average of $m_{B_s^*}$ [8], to the B_s^* momentum in the MC simulation one observes a large difference

$$\frac{p^*_{B_s^*,\text{w.a.}}}{p^*_{B_s^*,\text{MC}}} = 0.92\,. \tag{6.10}$$

As the momentum $p^*_{B_s}$ determines the width of the signal peak in the X_{mis} distribution, the X_{mis} modelling is very sensitive to the B_s^* mass. The overestimated B_s^* momentum in the MC simulation is corrected by multiplying the calculated X_{mis} value in the signal MC with the ratio calculated in Eq. 6.10. This procedure considerably improves the data-MC agreement in the signal region, as illustrated in Fig. 6.2 (b). However, with a χ^2 probability of 10^{-2} the agreement is still not satisfying. This is not surprising because in addition to the poor precision on the B_s^* mass, the exclusive $B_s \to D_s^{(*)} \ell \nu$ branching fractions and form factor parameters have not been measured yet. The semi-inclusive measurement based on the approach with the three counting regions is less sensitive to the B_s^* mass and the signal modelling.

6.3 Fit results

6.3.1 Determination of the D_s yields by $m_{KK\pi}$ fits

The D_s yields in the three counting regions are determined by binned extended maximum likelihood fits to the D_s peak in the $K^+K^-\pi^+$ mass

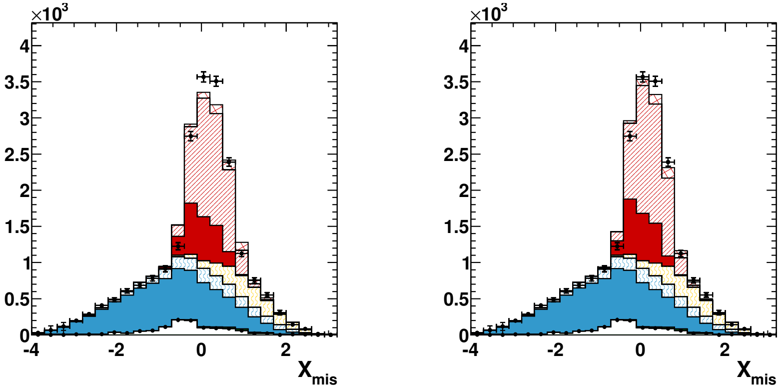

(a) $M_{B_s^*} = 5411.7\,\text{MeV}$ (b) $M_{B_s^*} = 5415.4\,\text{MeV}$

Figure 6.2: X_{mis} distribution of reconstructed $D_s^- \ell^+$ pairs, $\ell = e$ and μ, obtained by $K^+K^-\pi^+$ mass fits to the $\Upsilon(5S)$ data sample (black data points). The stacked histograms represent the MC expectations after applying the scale factors estimated from the event yields in the three counting regions (see text). Figure (a) shows the generated distribution and Figure (b) shows the MC distribution after applying the B_s^* mass correction (cf. Eq. 6.10). The legend explaining the colour code can be found in Fig. 6.1.

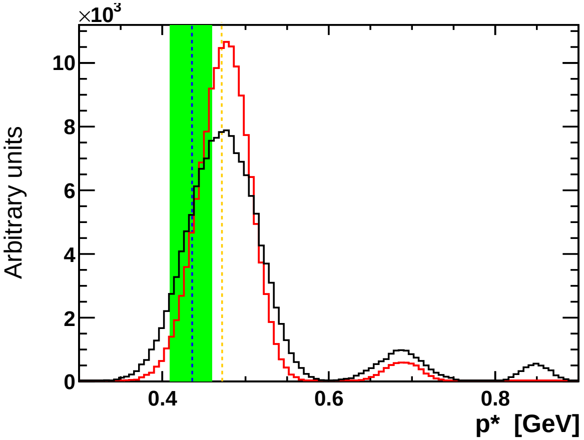

Figure 6.3: Simulated momentum distribution in the centre-of-mass frame of the e^+e^- collision for B_s^* mesons (red) and B_s mesons (black). The three peaks correspond from left to right to the three production modes $B_s^*\bar{B}_s^*$, $B_s\bar{B}_s^*$ and $B_s\bar{B}_s$. Orange line: expected B_s^* momentum for the $B_s^*\bar{B}_s^*$ production mode using the nominal MC B_s^* mass, $m_{B_s^*} = 5412.0\,\mathrm{MeV}$. Blue line with green uncertainty band: Expected B_s^* momentum for the $B_s^*\bar{B}_s^*$ production mode using the B_s^* mass from the PDG [8], $m_{B_s^*} = (5415.4^{+2.4}_{-2.1})\,\mathrm{MeV}$.

Parameter	Initialisation	Limits		
μ / GeV	1.96845	1.96545	…	1.97145
σ_1 / GeV	0.003	0.002	…	0.0075
$r_\sigma = \sigma_2/\sigma_1$	2.2	1.5	…	5.0
$r_N = N_2/N_1$	0.3	0.0	…	1.0
b	-0.15	-1.0	…	+1.0
N_{sig}	1/2 of data events	0	…	10^8
N_{bkg}	1/2 of data events	0	…	10^8

Table 6.6: Initialisation values and ranges of the fit parameters for the fits to the $m_{KK\pi}$ distributions. The shape parameters of the fit are explained in the text. The signal and background yields are given by N_{sig} and N_{bkg}, respectively.

distribution [97, 104]. The shape of the D_s mass peak is modelled as the sum of two Gaussian functions with common mean, μ:

$$P_{\text{sig}}(m_{KK\pi}) \propto \exp\left(\frac{-(m_{KK\pi}-\mu)^2}{2\sigma_1^2}\right) + r_N \cdot \exp\left(-\frac{(m_{KK\pi}-\mu)^2}{2(r_\sigma \cdot \sigma_1)^2}\right) . \quad (6.11)$$

The parameter σ_1 is the width of the first Gaussian, the parameter $r_\sigma = \sigma_2/\sigma 1$ defines the width of the second Gaussian, and the parameter r_N corresponds to the ratio of the normalisation of the second Gaussian to the normalisation of the first Gaussian. The distribution of random $K^+K^-\pi^+$ combinations is modelled as a first order Chebychev polynomial,

$$P_{\text{bkg}}(m_{KK\pi}) \propto 1 + b \cdot m_{KK\pi} . \quad (6.12)$$

The parameters σ_1, r_σ and r_N are fitted simultaneously in all three counting regions, while the mean of the D_s mass peak, μ, and the slope of the background, b, are fitted independently in each counting region. The initialisation values and limits of the fit parameters are listed in Table 6.6. The fit results in the individual counting regions together with the goodness of fit are given in Table 6.7. The fitted $m_{KK\pi}$ distributions are presented in Fig. 6.4. The fit results of the shape parameters are listed in Table B.1 in the Appendix.

(a) $B_s \to D_s X e \nu$ channel.

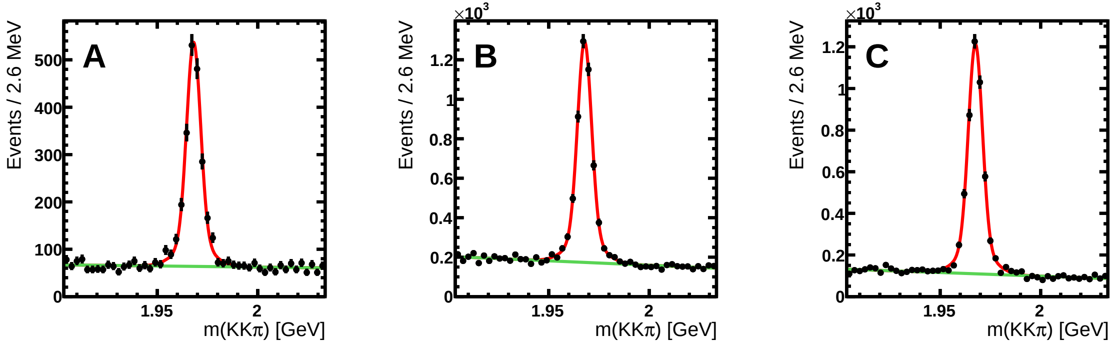

(b) $B_s \to D_s X \mu \nu$ channel.

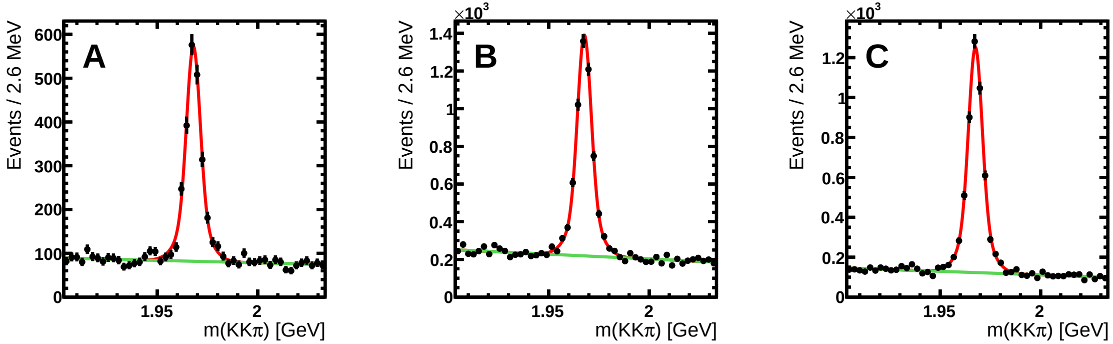

Figure 6.4: Fits to the $m_{KK\pi}$ distributions from $\Upsilon(5S)$ data divided into the three counting regions A, B and C defined in Sec. 6.1. The black points are the data, the green line is the fitted background distribution and the red line is the sum of the fitted signal and background distributions.

	A	B	C	χ^2 probability
$D_s^- e^+$	1807 ± 53	4274 ± 87	4215 ± 82	55 %
$D_s^- \mu^+$	1902 ± 54	4544 ± 89	4375 ± 81	15 %
$D_s^{*-} e^+$	336 ± 33	656 ± 48	662 ± 46	89 %
$D_s^{*-} \mu^+$	370 ± 35	739 ± 52	741 ± 50	12 %

Table 6.7: Results of the $m_{KK\pi}$ fits and the Δm fits to the $\Upsilon(5S)$ data. The D_s^- and D_s^{*-} yields obtained in the three counting regions are quoted with the statistical uncertainties. The goodness of fit is tested using the χ^2 probability of the fit result.

6.3.2 Determination of the D_s^* yields by Δm fits

The D_s^* yields are determined by fits to the mass difference $\Delta m = m_{D_s\gamma} - m_{D_s}$. This distribution provides a sharper signal peak compared to $m_{D_s\gamma}$, because the detector resolution of the D_s reconstruction cancels. The current world average of the measurement of the mass difference Δm is [8]:

$$\Delta m = [143.8 \pm 0.4]\ \text{MeV}\,. \tag{6.13}$$

In contrast to the signal peak in the $m_{KK\pi}$ distribution, the signal peak in the Δm distribution is asymmetric (see Fig. 6.5). The tail towards lower Δm values originates from events where the reconstructed ECL cluster does not contain the full photon energy deposit. To model this feature in the fit, the sum of a Gaussian function and a Crystal Ball function [105] with a common mean, μ, is chosen as PDF for the fit:

$$P_{\text{sig}}(\Delta m) \propto r_N \exp\left(-\frac{(\Delta m - \mu)^2}{2(r_\sigma \cdot \sigma_1)^2}\right) + \begin{cases} p_>(\Delta m) & \text{for } \frac{\Delta m - \mu}{\sigma_1} > -\alpha \\ p_\leq(\Delta m) & \text{for } \frac{\Delta m - \mu}{\sigma_1} \leq -\alpha\,. \end{cases}, \tag{6.14}$$

where

$$p_>(\Delta m) = \exp\left(-\frac{(\Delta m - \mu)^2}{2\sigma_1^2}\right), \tag{6.15}$$

and

$$p_\leq(\Delta m) = \left(\frac{n}{\alpha}\right)^n \cdot \exp\left(-\frac{\alpha^2}{2}\right)\left(\frac{n}{\alpha} - \alpha - \frac{\Delta m - \mu}{\sigma_1}\right)^{-n}. \tag{6.16}$$

The parameters r_N, r_σ, α and n are determined from a fit to the signal peak distribution from the MC simulation (see Fig. 6.5). In the fits to data, these parameters are constrained to the obtained values within the uncertainties. The width, σ_1, and the position, μ, of the signal peak are free parameters to accommodate the differences between the MC simulation and the data (see Fig. 5.9 (a)). The shape of the combinatorial background is described by a third order Chebychev polynomial,

$$P_{\mathrm{bkg},i}(\Delta m) \propto 1 + a_i \cdot \Delta m + b_i \cdot (2\Delta m^2 - 1) + c_i \cdot (4\Delta m^3 - 3\Delta m)\,. \quad (6.17)$$

The background shapes are different in each counting region, $i = A, B, C$, and therefore the parameters a_i, b_i, and c_i are estimated separately for each region from fits to the shapes predicted by the MC simulation (see Fig. B.2). In the fits to data, the parameters are constrained to the obtained values and their uncertainties are taken into account.

The fitted yields in the three counting regions together with the goodness of fit are listed in Table 6.7. The Δm distributions in data compared with the fit results are shown in Fig. 6.6. Table B.2 in the Appendix summarises the fitted shape parameters. The obtained values for the peak position, μ, are in good agreement with the world average from Eq. 6.13. For comparison, the results in the signal enhanced region C are:

$$\begin{aligned} e\,\text{mode}: \quad \mu &= [144.0 \pm 0.4]\ \text{MeV}\,, \\ \mu\,\text{mode}: \quad \mu &= [144.3 \pm 0.4]\ \text{MeV}\,. \end{aligned} \quad (6.18)$$

6.4 Background subtraction

In order to estimate the contribution of $c\bar{c}$ continuum in the three counting regions, the fitting procedure described above is also applied to $D_s^{(*)-}\ell^+$ samples reconstructed in off-resonance data. The off-resonance samples are considerably smaller and therefore all shape parameters of the fit functions are fixed to the values obtained from the fits to $\Upsilon(5S)$ data. A constant centre-of-mass energy, $\sqrt{s} = 10.876\,\text{GeV}$ is inserted in the expression for X_{mis} in Eq. 6.4 because the denominator would otherwise not be defined for the off-resonance energy. The obtained event yields are multiplied with the scale factor from Eq. 4.3 to take

(a) Electron mode

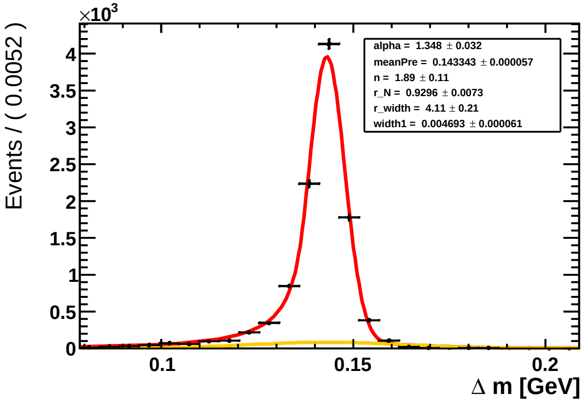

(b) Muon mode

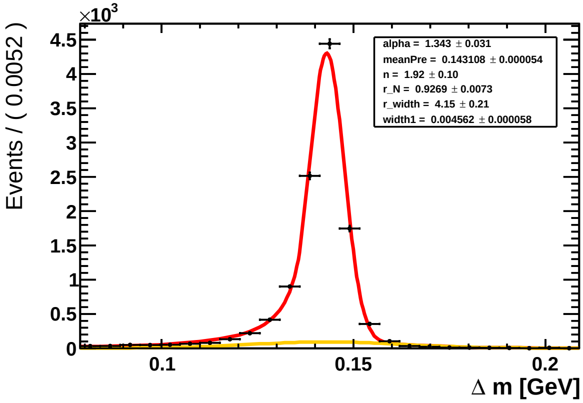

Figure 6.5: Fits to the Δm distribution of correctly reconstructed D_s^* candidates in the MC simulation. The black points represent the simulated decays and the red curve is the fitted signal distribution (Crystal ball + Gaussian function). The orange curve shows the contribution of the Gaussian function.

(a) $B_s \to D_s^{*} X e \nu$ channel.

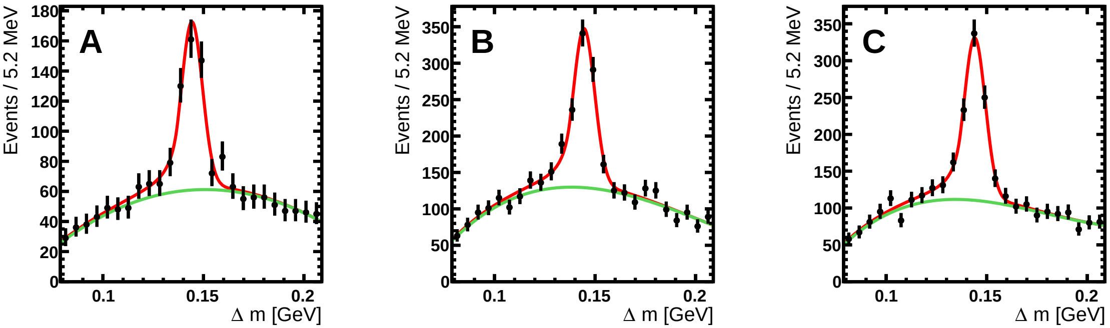

(b) $B_s \to D_s^{*} X \mu \nu$ channel.

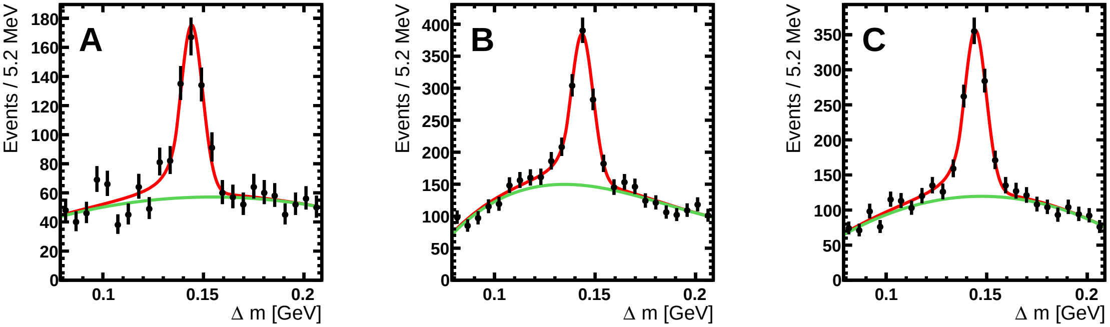

Figure 6.6: Fits to the Δm distributions from $\Upsilon(5S)$ data divided into the three counting regions A, B and C defined in Sec. 6.1. The black points are the data, the green line is the fitted background distribution and the red line is the sum of the fitted signal and background distributions.

into account the difference in luminosities and $e^+e^- \to q\bar{q}$ cross sections between the $\Upsilon(5S)$ and off-resonance data. Additionally, to this global scale factor, the event yields are adjusted in each counting region individually using correction factors determined from the MC simulation of $\Upsilon(5S)$ and off-resonance events. The estimated continuum yields are subtracted in each counting region from the yields obtained in $\Upsilon(5S)$ data.

The background from $B^0 \to D_s^{(*)} K\ell\nu$ and $B^+ \to D_s^{(*)} K\ell\nu$ decays, is estimated from a dedicated MC sample containing 7 938 decays for each of the four modes. The decays are simulated with a simple phase space model. Assuming a B production fraction of $f_{u,d} = 78\,\%$ [8], and using the measured branching fractions $\mathcal{B}(B \to D_s K\ell\nu) \approx \mathcal{B}(B \to D_s^* K\ell\nu) \approx 0.03\,\%$ [106, 107], the simulated yields have to be scaled down by a factor of 0.0476 to reflect the expectation in data. The $B \to D_s^{(*)} K\ell\nu$ backgrounds are subtracted from the measured $\Upsilon(5S)$ data yields in the individual counting regions.

6.5 Signal extraction

Tables 6.8, 6.9, 6.10 and 6.11 summarise the fitted $D_s^{(*)}$ yields in the three counting regions and the subtracted continuum and $B \to D_s^{(*)} K\ell\nu$ backgrounds. The remainder of the events is composed of the three components mentioned in the analysis overview: *wrong-side* combinations, *other* backgrounds and *signal*. For each MC component j a scale factor a_j is introduced. If $N_{i,j}$ are the predicted MC yields of the components j in the counting regions $i = A, B, C$, the scale factors a_j can be chosen such that the sum of the MC prediction in each counting region i equals the signal yield in data, D_i:

$$D_i = \sum_j a_j N_{i,j}\,. \tag{6.19}$$

	A	B	C
$\Upsilon(5S)$ data	1807 ± 53	4274 ± 87	4215 ± 82
(1) Continuum (scaled off-resonance data)	130 ± 34	278 ± 37	137 ± 22
(2) $B \to D_s K \ell \nu$	0	48 ± 7	18 ± 4
(3) Wrong-side, secondary leptons, misid. hadrons	110 ± 4	555 ± 10	61 ± 3
(3) Wrong-side, primary leptons	1565 ± 16	1165 ± 14	1032 ± 13
(4) Other	0	638 ± 10	89 ± 4
(5) Signal ($D_s \ell \nu$)	0	492 ± 9	669 ± 11
(5) Signal ($D_s^* \ell \nu$)	1	951 ± 13	2072 ± 19
(5) Signal ($D_s^{**} \ell \nu$; $D_s^{**} \to D_s^*$)	0	28 ± 2	41 ± 3
(5) Signal ($D_s^{**} \ell \nu$; $D_s^{**} \nrightarrow D_s^*$)	0	117 ± 5	98 ± 4

Table 6.8: $D_s^- e^+$ yields obtained from the $m_{KK\pi}$ fits to $\Upsilon(5S)$ data in the three counting regions and the corresponding signal and background expectations. The MC components (3) – (5) are scaled with the factors obtained from the minimisation of Eq. 6.20 (see Table 6.12). The uncertainties are statistical. Uncertainties are omitted if they are smaller than 0.5.

	A	B	C
$\Upsilon(5S)$ data	1902 ± 54	4544 ± 89	4375 ± 81
(1) Continuum (scaled off-resonance data)	102 ± 32	298 ± 40	134 ± 25
(2) $B \to D_s K \ell \nu$	0	46 ± 7	18 ± 4
(3) Wrong-side, secondary leptons, misid. hadrons	205 ± 6	826 ± 12	107 ± 4
(3) Wrong-side, primary leptons	1594 ± 17	1081 ± 14	1043 ± 14
(4) Other	1	798 ± 11	158 ± 5
(5) Signal ($D_s \ell \nu$)	0	489 ± 9	693 ± 11
(5) Signal ($D_s^* \ell \nu$)	0	872 ± 13	2072 ± 19
(5) Signal ($D_s^{**} \ell \nu$; $D_s^{**} \to D_s^*$)	0	26 ± 2	40 ± 3
(5) Signal ($D_s^{**} \ell \nu$; $D_s^{**} \nrightarrow D_s^*$)	0	109 ± 4	110 ± 4

Table 6.9: $D_s^- \mu^+$ yields obtained from the $m_{KK\pi}$ fits to $\Upsilon(5S)$ data in the three counting regions and the corresponding signal and background expectations. The MC components (3) – (5) are scaled with the factors obtained from the minimisation of Eq. 6.20 (see Table 6.12). The uncertainties are statistical. Uncertainties are omitted if they are smaller than 0.5.

	A	B	C
Measured yields			
$\Upsilon(5S)$ data	336 ± 33	656 ± 48	662 ± 46
(1) Scaled off-resonance data	32 ± 22	61 ± 17	24 ± 11
(2) $B \to D_s K\ell\nu$	0	6 ± 2	2 ± 1
(3) Wrong-side, secondary leptons, misid. hadrons	24 ± 2	60 ± 3	4 ± 1
(3) Wrong-side, primary leptons	279 ± 6	147 ± 5	120 ± 4
(4) Other	0	151 ± 6	20 ± 2
(5) Signal ($D_s^*\ell\nu$)	0	227 ± 6	483 ± 9
(5) Signal ($D_s^{**}\ell\nu$; $D_s^{**} \to D_s^*$)	0	6 ± 1	8 ± 1

Table 6.10: $D_s^{-*}e^+$ yields obtained from the Δm fits to $\Upsilon(5S)$ data in the three counting regions and the corresponding signal and background expectations. The MC components (3) – (5) are scaled with the factors obtained from the minimisation of Eq. 6.20 (see Table 6.12). The uncertainties are statistical.

	A	B	C
Measured yields			
$\Upsilon(5S)$ data	370 ± 35	739 ± 52	741 ± 50
(1) Scaled off-resonance data	49 ± 19	54 ± 18	20 ± 11
(2) $B \to D_s K \ell \nu$	0	4 ± 2	2 ± 1
(3) Wrong-side, secondary leptons, misid. hadrons	48 ± 3	99 ± 4	13 ± 1
(3) Wrong-side, primary leptons	273 ± 7	147 ± 5	109 ± 4
(4) Other	0	188 ± 7	39 ± 3
(5) Signal ($D_s^* \ell \nu$)	0	241 ± 7	547 ± 10
(5) Signal ($D_s^{**} \ell \nu;\ D_s^{**} \to D_s^*$)	0	6 ± 1	11 ± 1

Table 6.11: $D_s^{-*}\mu^+$ yields obtained from the Δm fits to $\Upsilon(5S)$ data in the three counting regions and the corresponding signal and background expectations. The MC components (3) – (5) are scaled with the factors obtained from the minimisation of Eq. 6.20 (see Table 6.12). The uncertainties are statistical.

This problem corresponds to solving a system of three equations with three unknowns. To find the scale factors a_j that solve the system and to evaluate their uncertainties, the expression

$$\chi^2 = \sum_{\text{regions } i} \frac{\left(D_i - \sum_j a_j N_{i,j}\right)^2}{(\Delta D_i)^2 + \sum_j (a_j \Delta N_{i,j})^2} \tag{6.20}$$

is minimised, where ΔD_i and $\Delta N_{i,j}$ are the statistical uncertainties of the data and the MC samples, respectively. The obtained scale factors, a_j, and the signal yields,

$$N_{\text{sig}} = \sum_i a_{\text{sig}} N_{i,\text{sig}} \,, \tag{6.21}$$

are listed in Table 6.12. Figures 6.7 and 6.8 illustrate the good data-MC agreement of the X_{mis} and p^*_ℓ distributions after applying the scale factors.

The generic formula to calculate the semi-inclusive semileptonic branching fractions was already introduced in Eq. 6.5. The efficiencies, $\epsilon_{D_s^{(*)}}$, are calculated as the weighted average of the efficiencies ϵ_k of the individual signal contribution $k = D_s \ell \nu, D_s^* \ell \nu, D_s^{**} \ell \nu$:

$$\epsilon_{D_s^{(*)}} = \frac{\sum_k w_k \epsilon_k}{\sum_k w_k} \,. \tag{6.22}$$

The efficiencies ϵ_k are taken from Table 6.5. The branching fractions of the reconstructed decay modes are [8]:

$$\begin{aligned} \mathcal{B}_{D_s} &= \mathcal{B}(D_s \to \phi \pi^+; \phi \to K^+ K^-) &&= [2.24 \pm 0.10]\ \% \,, \\ \mathcal{B}_{D_s^*} &= \mathcal{B}(D_s^* \to D_s \gamma) \cdot \mathcal{B}(D_s \to \phi \pi^+; \phi \to K^+ K^-) &&= [2.11 \pm 0.09]\ \% \,, \end{aligned} \tag{6.23}$$

(a) $D_s^- e^+$

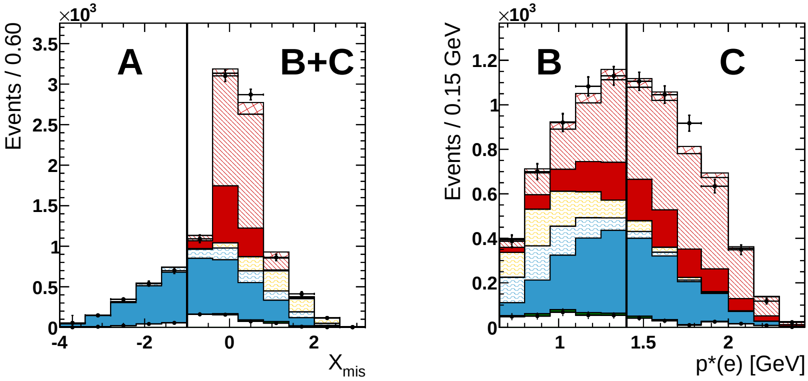

(b) $D_s^- \mu^+$

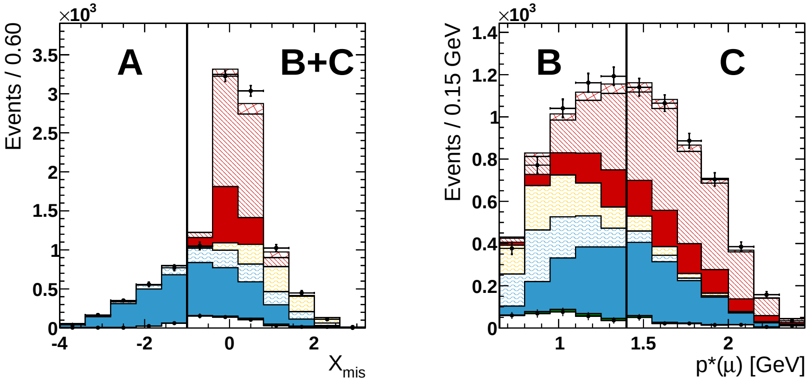

Figure 6.7: Distributions of $X_{\rm mis}$ and p^*_ℓ for $D_s^- \ell^+$ events reconstructed from the $\Upsilon(5S)$ data. The MC components are scaled with the scale factors obtained from the minimisation of Eq. 6.20.

(a) $D_s^{*-} e^+$

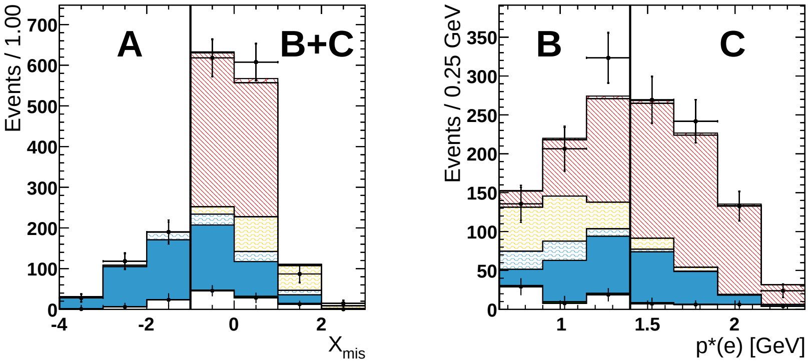

(b) $D_s^{*-} \mu^+$

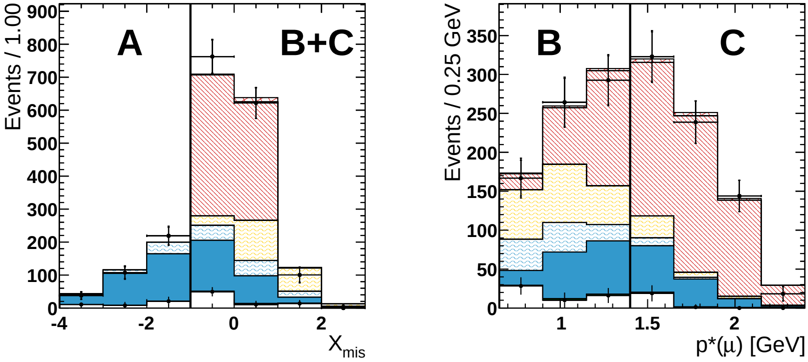

Figure 6.8: Distributions of X_{mis} and p^*_ℓ for $D_s^{*-}\ell^+$ events reconstructed from the $\Upsilon(5S)$ data. The MC components are scaled with the scale factors obtained from the minimisation of Eq. 6.20.

where the branching fraction $\mathcal{B}(D_s \to \phi\pi^+; \phi \to K^+K^-)$ is obtained from the relation

$$\begin{aligned}&\mathcal{B}(D_s \to \phi\pi^+; \phi \to K^+K^-) = \\ &\mathcal{B}(D_s \to K^+K^-\pi^+) \cdot \frac{\mathcal{B}(D_s \to \phi\pi^+; \phi \to K^+K^-)}{\mathcal{B}(D_s \to K^+K^-\pi^+)} \,. \end{aligned} \tag{6.24}$$

It has to be taken into account that the parameter f_s used to calculate $N_{B_s\bar{B}_s}$ is determined from a measurement of the branching fraction $\mathcal{B}(\Upsilon(5S) \to D_sX)$, where the D_s meson is reconstructed in the channel $D_s^+ \to K^+K^-\pi^+$ (cf. Sec. 4.3). This measurement used the branching fraction $\mathcal{B}(D_s \to K^+K^-\pi^+) = [5.49 \pm 0.27]$ % [68]. One obtains

$$\mathcal{B}(D_s \to K^+K^-\pi^+) \cdot N_{B_s\bar{B}_s} = (0.88 \pm 0.16) \times 10^6 \,. \tag{6.25}$$

The branching fraction $\mathcal{B}(D_s \to K^+K^-\pi^+)$ cancels out in Eq. 6.5, leading to

$$\mathcal{B}(B_s \to D_s^{(*)}X\ell\nu) = \frac{N_{\mathrm{sig}}}{\epsilon \cdot \mathcal{B}'_{D_s^{(*)}} \cdot \mathcal{B}(D_s \to K^+K^-\pi^+) \cdot N_{B_s\bar{B}_s} \cdot 2} \,, \tag{6.26}$$

where [8, 108, 109]

$$\begin{aligned}\mathcal{B}'_{D_s} &= \mathcal{B}(D_s \to \phi\pi^+;\ \phi \to K^+K^-)/\mathcal{B}(D_s \to K^+K^-\pi^-) \\ &= [41.6 \pm 0.8]\ \% \,, && (6.27)\\ \mathcal{B}'_{D_s^*} &= \mathcal{B}(D_s \to \phi\pi^+;\ \phi \to K^+K^-)/\mathcal{B}(D_s \to K^+K^-\pi^-)\ \cdot\ \mathcal{B}(D_s^* \to D_s\gamma) \\ &= [39.2 \pm 0.8]\ \% \,. && (6.28)\end{aligned}$$

The semi-inclusive semileptonic branching fractions obtained from Eq. 6.26 are:

$$\begin{aligned}\mathcal{B}(B_s \to D_s e\nu\ X) &= [8.1 \pm 0.3(\mathrm{stat}) \pm 1.4(\mathrm{ext})]\% \,, && (6.29)\\ \mathcal{B}(B_s \to D_s \mu\nu\ X) &= [8.3 \pm 0.3(\mathrm{stat}) \pm 1.5(\mathrm{ext})]\% \,, && (6.30)\\ \mathcal{B}(B_s \to D_s^* e\nu\ X) &= [5.2 \pm 0.6(\mathrm{stat}) \pm 0.9(\mathrm{ext})]\% \,, && (6.31)\\ \mathcal{B}(B_s \to D_s^* \mu\nu\ X) &= [5.7 \pm 0.6(\mathrm{stat}) \pm 1.0(\mathrm{ext})]\% \,, && (6.32)\end{aligned}$$

	Wrong-side	Other	Signal	Signal yield
$D_s e$	1.020 ± 0.039	1.000 ± 0.199	1.062 ± 0.038	4470 ± 161
$D_s \mu$	1.061 ± 0.038	0.939 ± 0.158	1.086 ± 0.040	4411 ± 161
$D_s^* e$	0.89 ± 0.12	1.66 ± 0.71	1.00 ± 0.11	724 ± 79
$D_s^* \mu$	0.96 ± 0.12	1.50 ± 0.58	1.13 ± 0.12	804 ± 86

Table 6.12: Scale factor for the MC components extracted by minimising the χ^2 defined in Eq. 6.20. The quoted errors are the statistical uncertainties of the data and the MC sample. The signal yields are determined by integrating over all three counting regions. The backgrounds yields are given in Tables 6.8, 6.9, 6.10 and 6.11.

	$\epsilon_{D_s^{(*)}}$ [%]	$N_{\mathrm{sig}} \epsilon^{-1}$	$N_{\mathrm{sig}} \epsilon^{-1} \mathcal{B}_{\mathrm{reco}}^{-1} N_{B_s \bar{B}_s}^{-1}$ [%]
$D_s e$	16.9 ± 0.1	26403 ± 951	8.14 ± 0.29
$D_s \mu$	16.3 ± 0.1	27012 ± 986	8.33 ± 0.30
$D_s^* e$	4.6 ± 0.1	15805 ± 1725	5.18 ± 0.56
$D_s^* \mu$	4.6 ± 0.1	17537 ± 1876	5.74 ± 0.61

Table 6.13: Efficiencies, efficiency-corrected yields and measured branching fractions. The quoted uncertainties are purely statistical.

where the first uncertainty is the statistical uncertainty of the measurement and the second uncertainty is due to the external inputs $N_{B_s \bar{B}_s}$ and $\mathcal{B}'_{D_s^{(*)}}$, where the cancellation of the $\mathcal{B}(D_s \to K^+ K^- \pi^+)$ branching fraction in Eq. 6.26 is taken into account.

6.6 Systematic uncertainties

Below, the systematic uncertainties due to detector effects and the modelling of signal and background distributions are described. An overview of all systematic uncertainties can be found in Table 6.14.

	$D_s X e\nu$	$D_s X \mu\nu$	$D_s^* X e\nu$	$D_s^* X \mu\nu$
Detector				
Tracking efficiency	1.4	1.4	1.4	1.4
Photon efficiency	—	—	2.0	2.0
Kaon and pion ID	1.4	1.4	1.4	1.4
Lepton efficiency	1.0	1.6	1.0	1.6
Rate of misidentified hadrons	0.1	1.3	0.1	1.9
Signal and background modeling				
PDF for $m_{KK\pi}$ and Δm fits	3.0	3.0	5.0	5.0
Continuum shape	1.2	0.3	1.2	0.3
$B \to D_s^{(*)} K \ell \nu$ modelling	0.3	0.3	0.1	0.1
Signal				
Composition	4.8	4.8	0.3	< 0.1
Form factors	0.9	1.0	1.0	1.0
Efficiency	3.1	3.1	3.0	3.0
Wrong-side				
Composition	1.6	2.2	1.0	2.5
B_s fraction	0.2	0.2	< 0.1	< 0.1
Shape	1.0	1.0	1.0	1.0
Other				
Composition and shape	0.3	0.3	0.4	0.7
B_s production mode	0.1	0.1	0.3	0.3
Beam energy	1.0	1.0	0.5	0.5
Total	7.3	7.6	6.9	7.6

Table 6.14: Overview of the relative systematic uncertainties in %.

6.6.1 Detector effects

The signal is reconstructed from four charged tracks and the track reconstruction efficiency uncertainty per track is 0.35 %. The resulting uncertainty is thus $4 \cdot 0.35\,\% = 1.4\,\%$. The K/π identification uncertainties are evaluated by varying the MC expectations up and down by their uncertainties (cf. Sec. 5.1). This is done simultaneously in all three counting regions. The measured $D_s^{(*)}$ signal yields change by 1.4 %. The misidentification rates of kaons and pions do not affect the uncertainty of the measurement because only the correctly reconstructed D_s candidates are used from MC simulation. The uncertainties on the lepton identification are evaluated by a simultaneous variation of the MC expectation of true lepton candidates in all three counting regions by the uncertainties calculated from Eq. 5.9. The resulting change of the signal yield is 1.0 % for electrons and 1.6 % for muons. The same procedure is used to determine the uncertainties due to the hadron misidentification probability in the lepton selection. The observed changes of the signal yields are 0.1 % ($D_s X e \nu$), 1.3 % ($D_s X \mu \nu$), 0.1 % ($D_s^* X e \nu$) and 1.9 % ($D_s^* X \mu \nu$). The uncertainty on the photon detection efficiency is investigated with radiative Bhabha events ($e^+e^- \to e^+e^-\gamma$) and is estimated to be 2 % [110].

6.6.2 Signal and background modelling

There are two different types of uncertainties concerning the signal and background modelling. The first type is related to uncertainties in the determination of the $D_s^{(*)}$ yields. The second type is related to uncertainties in the MC modelling of the signal and background processes. The modelling is tested with various control samples and the uncertainties are estimated with data-driven methods where possible.

Determination of the $D_s^{(*)}$ yields from $B_{(s)}$ decays

The modelling of the PDF shapes describing the signal peak and the combinatorial background in the D_s mass fits is studied with the MC samples from the full detector simulation. The D_s yields obtained from the fits to the simulated $m_{KK\pi}$ distributions are compared to the number of generated D_s mesons. An average deviation of $-3\,\%$ is observed which is assigned as PDF uncertainty in the measurement. The uncertainty due to the PDFs used in the Δm fits to the D_s^* samples is tested in an analogous way and the uncertainty is estimated to be $5\,\%$. The combinatorial background in the Δm distribution contains contributions from misreconstructed D_s mesons, correctly reconstructed D_s mesons from D_s^* decays paired with the wrong photon and correctly reconstructed D_s mesons which do not stem from D_s^* decays. Figure 5.9 (b) shows a shape comparison of the different components. No significant difference can be observed. Therefore, no uncertainty is assigned on the composition of the combinatorial background.

A variation of the normalisation of the continuum background within the uncertainties of the global scale factor for the off-resonance data (cf. Eq. 4.3) has no significant effect on the signal yield. To estimate the uncertainty due to the continuum correction for the individual counting regions, the measurement is repeated without this correction. The observed change of the signal yield is $1.2\,\%$ for the electron modes and $0.3\,\%$ for the muon modes. This change is assigned as systematic uncertainty.

The influence of the $B \to D_s^{(*)} K \ell \nu$ modelling on the measured signal yield is estimated by replacing the simple phase space model with the ISGW2 model assuming that the decay proceeds via $B \to D_0^* \ell \nu$; $D_0^* \to D_s^{(*)} K$. The use of this alternative model changes the signal yields by 0.3% ($D_s X \ell \nu$ channels) and 0.1% ($D_s^* X \ell \nu$ channels).

A variation of the $B \to D_s^{(*)} K \ell \nu$ branching fraction by the 20% uncertainty of the current world average changes the signal yields only by a negligible amount.

Signal modelling

The signal MC is a cocktail of the $D_s \ell \nu$, $D_s^* \ell \nu$ and $D_s^{**} \ell \nu$ modes, and each mode has a characteristic p_ℓ^* spectrum determined by the form factors. Therefore, the predicted signal yields in the counting regions B and C depend on the form factor parametrisations and the mixing ratio of the signal components.

Most of the branching fraction predictions for $B_s \to D_s^* \ell \nu$ decays are covered by a ±30 % variation of the nominal value in the simulation, $\mathcal{B}(B_s \to D_s \ell \nu) = 5.3\,\%$ (cf. Fig. 2.9). To evaluate the uncertainty due the signal composition, the $D_s^* \ell \nu$ signal contribution is therefore varied by 30 % and the $D_s \ell \nu$ component is scaled such that the total number of signal events is conserved. The range of the predicted $B_s \to D_s^{**} \ell \nu$ branching fractions is even larger (cf. Table 2.2) and therefore, this contribution is varied by 100 %. The observed changes of the signal yields for both variations are added quadratically. The resulting uncertainty is 4.8 % for the $B_s \to D_s X \ell \nu$ measurements and below 0.3 % for the $B_s \to D_s^* X \ell \nu$ measurements. The smaller uncertainty for the latter mode is expected, as it is dominated by the $D_s^* \ell \nu$ contribution.

The uncertainty on the $B_s \to D_s \ell \nu$ and $B_s \to D_s^* \ell \nu$ CLN form factor parameters due to $\mathrm{SU(3)}_{\mathrm{flavour}}$ symmetry breaking is estimated to be 10 % (cf. Sec. 2.4.2). The impact on the measurement is evaluated by varying each form factor parameter individually by ±10 %. The uncertainty on the modelling of the $D_s^{**} \ell \nu$ modes is determined by testing different options of the LLSW model as specified in Ref. [38]. The average deviation from the nominal signal yield is assigned as systematic uncertainty. The uncertainties are added linearly for each mode. The total uncertainty is calculated by adding the uncertainties of the individual modes quadratically; it is about 1 %. A summary of the form factor uncertainties can be found in Table 6.15.

The signal modelling also affects the efficiencies listed in Table 6.13. The efficiencies are defined as the ratios of the measured signal yields to the true number of signal decays in the detector. They account for the influence of the detector acceptance, the particle reconstruction algorithms and the selection criteria. The signal model used in the MC simulation, i.e. the composition of the signal and the simulated kinematic distributions, influences how much of the signal is expected inside and outside of the acceptance region. The modelling of the signal efficiency is studied with the $D_s^- \ell^+$ samples – the statistical power of the $D_s^{*-} \ell^+$ samples is too low to draw conclusions. Three variables are chosen for this study: p_ℓ^*, X_{mis} and the angle between the lepton and the D_s meson, $\alpha(D_s \ell)$. Figures 6.9 and 6.10 show the efficiencies in bins of these variables. The efficiency increases with the lepton momentum,

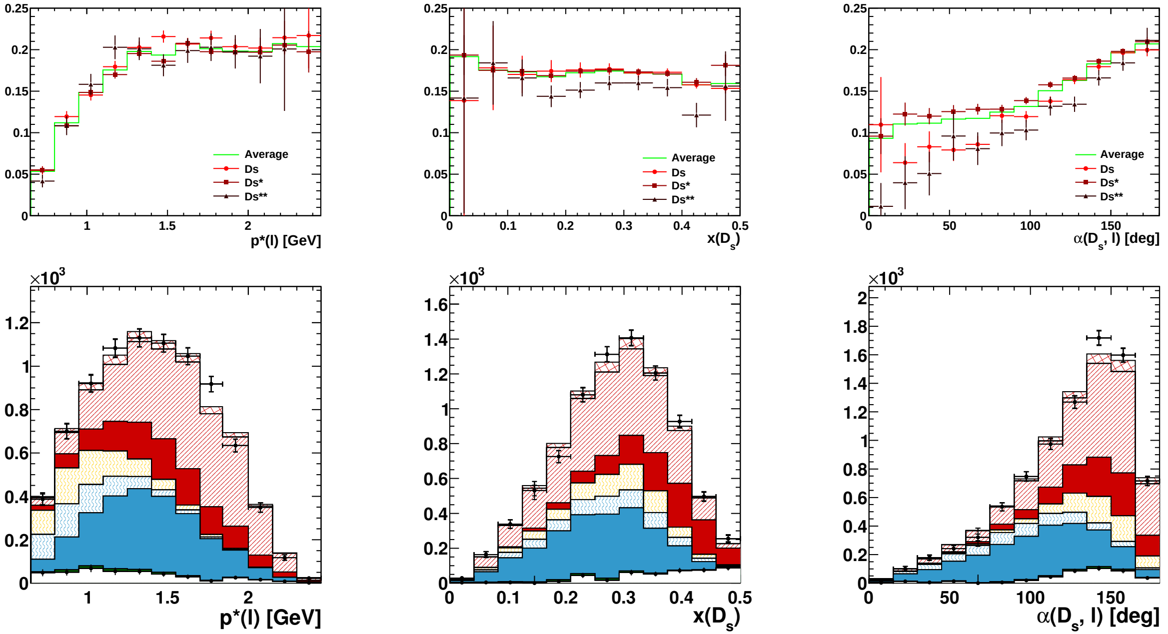

Figure 6.9: Top: Signal efficiencies in bins of the electron momentum, the D_s momentum and the angle between D_s and electron momentum for reconstructed $D_s^- e^+$ events. All variables are calculated in the centre-of-mass frame of the $\Upsilon(5S)$ resonance. Bottom: Corresponding data-MC agreement in the signal region $X_{\text{mis}} > -1$ after applying the scale factors from Table 6.12.

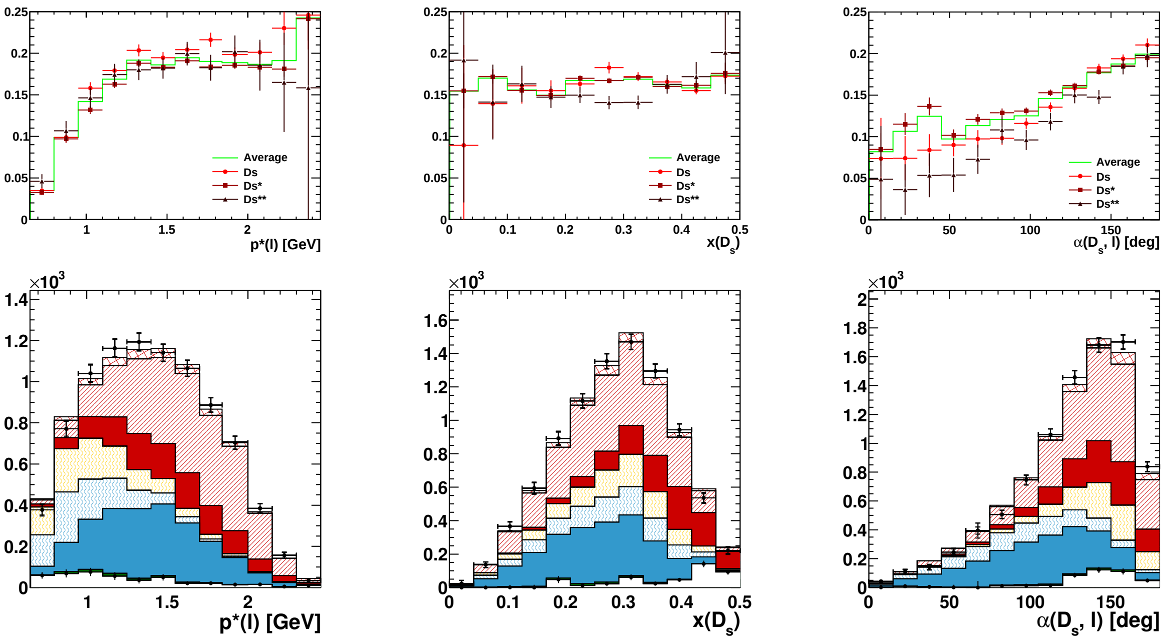

Figure 6.10: Top: Signal efficiencies in bins of the muon momentum, the D_s momentum and the angle between D_s and muon momentum for reconstructed $D_s^- \mu^+$ events. All variables are calculated in the centre-of-mass frame of the $\Upsilon(5S)$ resonance. Bottom: Corresponding data-MC agreement in the signal region $X_{\text{mis}} > -1$ after applying the scale factors from Table 6.12.

	$D_s\ell\nu$	$D_s^*\ell\nu$			$D_s^{**}\ell\nu$	
	ρ_D	ρ	R_1	R_2	LLSW	$\sum$
$D_sXe\nu$	0.21	0.50	0.11	0.24	0.19	0.9
$D_sXmu\nu$	0.08	0.50	0.15	0.22	0.43	1.0
$D_s^*Xe\nu$	—	0.59	0.08	0.26	0.46	1.0
$D_s^*X\mu\nu$	—	0.37	0.26	0.33	0.26	1.0

Table 6.15: Change of the signal yield in % for variations of the different signal model parameters. The HQET2 parameters (ρ_D, ρ, R_1, R_2) are varied individually by ±10%. The LLSW model is evaluated for different model options as specified in Ref. [38]. The uncertainties are added linearly for each mode. The total uncertainty is obtained by adding the uncertainties of the individual modes quadratically.

p^*_ℓ, until it saturates above 1.4 GeV. In $x(D_s)$, it is is more or less uniform over the full range. For $\alpha(D_s\ell)$, the efficiency increases towards larger values. The p^*_ℓ, X_{mis} and $\alpha(D_s\ell)$ data distributions are in good agreement with the MC simulation as shown in Figs. 6.9 and 6.10. Although this is not a proof for the correct description of the signal efficiencies in the MC simulation, it adds some confidence in the modelling.

In order to test the MC description also in the low lepton momentum region, the lepton momentum threshold is lowered to 0.3 GeV for electrons and 0.6 GeV for muons. The scale obtained scale factors from the χ^2 minimisation are in agreement with the nominal scale factors (see Table 6.16). This is a further indication that the p^*_ℓ spectrum is well modelled in the simulation. The data-MC agreement is also tested for subsamples with high lepton momentum ($p^*_\ell > 1.4$ GeV) and low lepton momentum ($p^*_\ell < 1.4$ GeV) separately. The agreement is good except for the $\alpha(D_s\ell)$ distribution in low lepton momentum sample (see Fig. 6.11). This discrepancy could be due to either the signal modelling or the modelling of the backgrounds from secondary leptons and misidentified hadrons. It is assumed that the signal model causes this effect and an uncertainty is assigned. For this, the $\alpha(D_s\ell)$ distribution is divided in two regions, below and above 120°. The average efficiencies estimated from the MC simulation, the observed data-MC differences, and the fractions of the signal are:

	Wrong-side		Other		Signal	
	I	II	I	II	I	II
$D_s e$	1.02 ± 0.04	1.04 ± 0.04	1.00 ± 0.20	0.87 ± 0.10	1.06 ± 0.04	1.07 ± 0.04
$D_s \mu$	1.06 ± 0.04	1.05 ± 0.04	0.94 ± 0.16	0.87 ± 0.12	1.09 ± 0.04	1.10 ± 0.04
$D_s^* e$	0.89 ± 0.12	0.93 ± 0.12	1.66 ± 0.71	1.17 ± 0.34	1.00 ± 0.11	1.02 ± 0.11
$D_s^* \mu$	0.96 ± 0.12	0.91 ± 0.12	1.50 ± 0.58	1.42 ± 0.46	1.13 ± 0.12	1.18 ± 0.12

Table 6.16: Extracted scale factors for (I) the analysis selection with a lepton momentum threshold of $p_\ell > 0.9\,\text{GeV}$ and (II) a selection with lowered thresholds $p_e > 0.3\,\text{GeV}$ and $p_\mu > 0.6\,\text{GeV}$.

B_s branching fraction [%]			Change of efficiency [%]			
$D_s\ell\nu$	$D_s^*\ell\nu$	$D_s^{**}\ell\nu$	$D_s^-e^+$	$D_s^-\mu^+$	$D_s^{*-}e^+$	$D_s^{*-}\mu^+$
2.1	5.3	0.6	Nominal values			
1.1	6.3	0.6	+0.5	−0.1	0.0	0.0
3.1	4.3	0.6	−0.4	+0.1	0.0	0.2
1.8	4.9	1.3	−0.6	−0.6	−0.4	−0.4
Relative uncertainty [%]			0.6	0.6	0.4	0.4

Table 6.17: Efficiencies for the semi-inclusive decays for different sets of signal branching fractions.

$\alpha(D_s, \ell)$	Avg. efficiency	Data-MC difference	Signal fraction
< 120°	≈ 10 %	−25 %	44 %
> 120°	≈ 15 %	25 %	56 %

If the average efficiency is corrected for the observed data-MC discrepancy, it increases by 8 % in this region. Taking into account that the subsample with $p_\ell^* < 1.4\,\text{GeV}$ contains only one third of all reconstructed signal events, the average efficiency changes by only 3 %. Following again the argument that the $D_s^*\ell\nu$ component dominates in the $D_s^-\ell^+$ sample, the same uncertainty is attributed to the efficiency estimation in the $B_s \rightarrow D_s^*X\ell\nu$ measurements.

Modelling of the wrong-side combinations

Two categories of events contribute to the *wrong-side* component. The first one contains events with a primary lepton from a semileptonic B_s or B decay. The second category contains the events with lepton candidates from secondary decays or misidentified hadrons. The leptons from the first category have a significantly harder momentum spectrum than those from the second category. The two categories are merged into the *wrong-side* component for the signal extraction, because the normalisation of both is determined by the inclusive $B_s \rightarrow D_s^{(*)}X$ decay rates. Suitable control samples for these *wrong-side* decays are same-sign samples, $D_s^+\ell^+$, because the same-sign requirement ensures that they are signal-free (cf. Ch. 5). There is one caveat: The relative amount of B_s mesons with respect to B mesons ($N_{B_s\bar{B}_s} : N_{B\bar{B}}$) is higher in the $D_s^+\ell^+$ samples (85 : 15) compared to the $D_s^-\ell^+$ samples (50 : 50). Since the modelling of B decays has been already tested in detail by other analyses with $\Upsilon(4S)$ data, the higher amount of B_s mesons in the control sample is not a problem, but rather an advantage as it increases the sensitivity to the B_s modelling. Figure 6.12 shows the lepton momentum and X_{mis} distributions for the same-sign electron and muon control samples and the fitted MC predictions for the primary leptons and the other lepton candidates. The obtained scale factors of the two fit components listed in Table 6.18 are in agreement within their uncertainties, which justifies the approach of treating the two components as single component in the measurement. The fits are also repeated with lowered lepton momentum thresholds, $p_e = 0.3\,\text{GeV}$ and $p_\mu = 0.6\,\text{GeV}$. Consistent results are obtained. Based on the (statistical) fit uncertainties in Table 6.18 and considering the different $N_{B_s\bar{B}_s} : N_{B\bar{B}}$ composition of the control sample, the uncertainty of the amount of primary leptons in the $D_s^-\ell^+$ *wrong-side* component is estimated conservatively with 10 %. A variation of the amount of primary leptons in the *wrong-side* component by 10 % causes a change of the signal yield between 1.0 % and 2.5 % depending on the reconstructed decay channel.

The *wrong-side* component contains events from B_s and B decays. The uncertainty on the composition given by f_s/f_{ud} is 20 %. A variation of the B_s contribution by this amount, changes the extracted signal yield by only 0.2 %.

The number of processes contributing to the *wrong-side* component is so large that a variation of individual model parameters is not practical. Instead, a data-driven approach is pursued based on the $D_s^+\ell^+$ control samples. The samples are divided into the three counting regions and the event yields are determined by $m_{KK\pi}$ fits. The D_s yields are then compared to the MC predictions of the corresponding counting regions and the data-MC ratios are calculated. These ratios range from 0.861 to 0.907 and from 0.956 to 0.971 for the electron and muon modes, respectively. The analysis procedure is repeated with the ratios applied as scale factors to the MC predictions for the *wrong-side* component of the $D_s^-\ell^+$ samples. The signal yields change by less than 0.4 %. Based on this result, the systematic uncertainty is estimated to be 1 %, which should

	p_ℓ threshold [GeV]	Scale factor "primary"	Scale factor "other"	χ^2 probability
Analysis selection				
$D_s^+ e^+$	0.9	0.90 ± 0.04	0.87 ± 0.09	5%
$D_s^+ \mu^+$	0.9	0.97 ± 0.04	0.99 ± 0.07	63%
Low momentum selection				
$D_s^+ e^+$	0.3	0.87 ± 0.03	0.89 ± 0.03	37%
$D_s^+ \mu^+$	0.6	0.97 ± 0.03	0.99 ± 0.05	58%

Table 6.18: Scale factors and χ^2 probability obtained from fits of the primary and other lepton MC components to the measured lepton momentum spectra in same-sign $D_s^+ \ell^+$ samples with different lower p_ℓ thresholds.

cover potential differences between the $D_s^+ \ell^+$ control samples and the $D_s^- \ell^+$ signal samples. The described method to estimate the modelling uncertainty of the *wrong-side* component cannot be transferred to the $D_s^* X \ell \nu$ channels because the event yields in the $D_s^{*+} \ell^+$ control samples are too low. It can, however, be assumed that the uncertainties are similar because $B_s \to D_s^* X \ell \nu$ decays are expected to be the dominant contribution in the $D_s^- \ell^+$ samples.

Modelling of the other background

The estimation of a systematic uncertainty due to the modelling of the *other* component is challenging because there is no dedicated control sample, and selections based on discriminating variables such as X_{mis} lead to samples with too low event yields. In the discussion of the signal efficiency modelling, it was pointed out that lowering the lepton momentum threshold leads to results consistent with the analysis selection (cf. Table 6.16). As the *other* background is enhanced by the low momentum threshold selection, this can also be taken as an indication that the *other* component is well modelled in the simulation. The plots shown in Fig. B.4 in the Appendix demonstrate the decent modelling of the X_{mis} and p_ℓ^* shapes. The processes contributing to the *other* background are categorised in the four classes listed in Table 6.19. The differences between the composition of the $D_s^- \ell^+$ and $D_s^{*-} \ell^+$ samples are negligible. Since many decay modes contribute to the *other* component, a variation of the individual parameters is not practical. The momentum distributions of secondary leptons from charmed meson (X_c) decays are similar regardless of whether the parent particle is a B_s or a B meson. Leptons from τ decays have higher momenta and also the momentum distribution of misidentified hadrons has a different shape. In the light of the complete absence of measurements for most B_s branching fractions, the fraction of leptons from τ decays and the fraction of misidentified hadrons are varied up and down by as much as 50 % and the measurement is repeated. The average deviation from the nominal signal yields is found to be less than 1 %. The large variation of the composition of the *other* component is expected to cover also the uncertainty due to the modelling of the subcomponents.

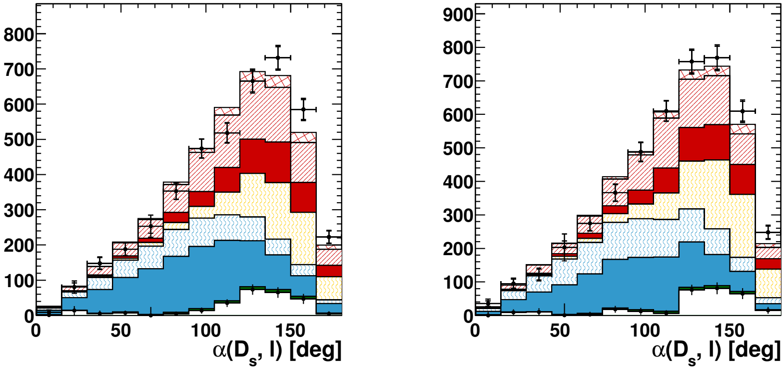

(a) $D_s^- e^+$ (b) $D_s^- \mu^+$

Figure 6.11: Distribution of the angle between the reconstructed momentum of the D_s meson and the lepton candidate in the $D_s^- \ell^+$ subsamples for $X_{\text{mis}} > -1$ and $p_\ell^* < 1.4\,\text{GeV}$.

	$D_s^{(*)} e$	$D_s^{(*)} \mu$
$B \to D_s^{(*)} X_c$	45	29
$B_s \to D_s^{(*)} X_c$	26	18
τ decays	21	16
Misidentified leptons	9	34

Table 6.19: Main sources of *other* leptons with their fractions in %.

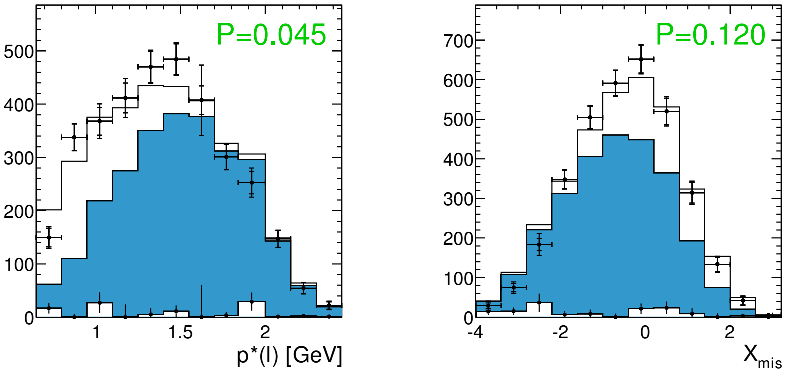

(a) $D_s^+ e^+$

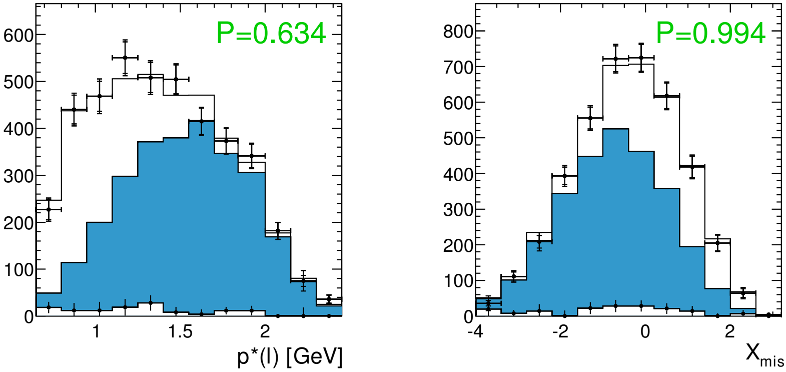

(b) $D_s^+ \mu^+$

Figure 6.12: Lepton momentum and X_{mis} distributions of the $D_s^+ \ell^+$ control samples. The black points with error bars are the data yields obtained from $m_{KK\pi}$ fits. The staked histograms represent from bottom to top: continuum estimated with off-resonance data (white), primary leptons (solid blue), secondary leptons and misidentified hadrons (white). The normalisations of 1. primary leptons and 2. secondary leptons and misidentified hadrons are determined by a fit to data after subtraction of the continuum background. The green numbers indicate the χ^2 probability of the fit.

B_s production mode and beam energy

The different B_s production modes ($B_s^*\bar{B}_s^*$, $B_s^*\bar{B}_s$, $B_s\bar{B}_s$) discussed in Sec. 4 result in slightly different kinematics. This effect is evaluated by varying the fraction of $B_s\bar{B}_s^*$ by 30 % motivated by the uncertainty of $F'_{B_s^*\bar{B}_s}$ (cf. Eq. 4.13). This variation changes the measured branching fraction by only 0.1 % for the $D_s^-\ell^+$ modes and by 0.3 % for the $D_s^{*-}\ell^+$ modes. The beam energy is conservatively varied by 3 MeV (cf. Ref. [80]), which changes the signal yields by 1 % ($D_s^-\ell^+$) and 0.5 % ($D_s^{*-}\ell^+$).

6.7 Results

The semi-inclusive semileptonic branching fractions with the statistical uncertainties, the systematic uncertainties and the uncertainties due to the external inputs are:

$$\mathcal{B}(B_s \to D_s e\nu\, X) = [8.1 \pm 0.3(\text{stat}) \pm 0.6(\text{syst}) \pm 1.4(\text{ext})]\% \quad (6.33)$$
$$\mathcal{B}(B_s \to D_s \mu\nu\, X) = [8.3 \pm 0.3(\text{stat}) \pm 0.6(\text{syst}) \pm 1.5(\text{ext})]\% \quad (6.34)$$
$$\mathcal{B}(B_s \to D_s^* e\nu\, X) = [5.2 \pm 0.6(\text{stat}) \pm 0.4(\text{syst}) \pm 0.9(\text{ext})]\% \quad (6.35)$$
$$\mathcal{B}(B_s \to D_s^* \mu\nu\, X) = [5.7 \pm 0.6(\text{stat}) \pm 0.4(\text{syst}) \pm 1.0(\text{ext})]\% \quad (6.36)$$

The electron and muon measurements are statistically independent because only one $D_s^{(*)-}\ell^+$ candidate is selected per event. The systematic uncertainties are all correlated except for the one due to the lepton identification. Taking into account the correlations, the following weighted averages are calculated:

$$\begin{aligned}\mathcal{B}(B_s \to D_s X\ell\nu) &= [8.2 \pm 0.2(\text{stat}) \pm 0.6(\text{syst}) \pm 1.4(\text{ext})]\%\,,\\ \mathcal{B}(B_s \to D_s^* X\ell\nu) &= [5.4 \pm 0.4(\text{stat}) \pm 0.4(\text{syst}) \pm 0.9(\text{ext})]\%\,.\end{aligned} \quad (6.37)$$

The measurement of the $B_s \to D_s X\ell\nu$ yield can alternatively be used to determine the value of $N_{B_s\bar{B}_s}$. For this, Eq. 6.5 is solved for $N_{B_s\bar{B}_s}$

and the branching fraction estimate from Eq. 6.3 is inserted for $\mathcal{B}(B_s \to D_s X\ell\nu)$:

$$N_{B_s\bar{B}_s} = \frac{N_{\text{sig}}/[\epsilon\mathcal{B}(D_s \to \phi(K^+K^-)\pi^+)]}{2\mathcal{B}_{\text{est}}(B_s \to D_s X\ell\nu}) \,. \tag{6.38}$$

Using for N_{sig}/ϵ the weighted average between the electron and muon mode,

$$N_{\text{sig}}/\epsilon = [26.7\ \pm 0.7\,(\text{stat})\ \pm\ 2.0\,(\text{syst})]\ \times\ 10^3\,, \tag{6.39}$$

one obtains

$$N_{B_s\bar{B}_s} = [6.93 \pm 0.18(\text{stat}) \pm 0.52(\text{syst}) \pm 0.51(\text{ext})] \times 10^6\,. \tag{6.40}$$

Here, the first two uncertainties are the statistical and systematic uncertainties on the measurement of the signal yield and the last uncertainty is due to the branching fraction $\mathcal{B}(D_s \to \phi(K^+K^-)\pi^+)$ and the estimate for $\mathcal{B}_{\text{est}}(B_s \to D_s X\ell\nu)$. The $B_s^{(*)}\bar{B}_s^{(*)}$ production cross-section at a centre-of-mass energy $\sqrt{s} = 10.86\,\text{GeV}$ is calculated by dividing $N_{B_s\bar{B}_s}$ by the integrated luminosity:

$$\begin{aligned}\sigma_{\Upsilon(5S)}(e^+e^- \to B_s^{(*)}\bar{B}_s^{(*)}) &= \frac{N_{B_s\bar{B}_s}}{\mathcal{L}} \\ &= [57.1\ \pm 1.5\,(\text{stat})\ \pm 4.3\,(\text{syst})\ \pm 4.2\,(\text{ext})]\,\text{pb}\,.\end{aligned} \tag{6.41}$$

CHAPTER 7

Inclusive studies: $B_s \to X\ell\nu$

The measurement of the $B_s \to X\ell\nu$ branching fraction, where X stands for an unspecified hadronic final state, tests the SU(3)$_{\text{flavour}}$ symmetry prediction (cf. Eq. 2.80) and can give additional confidence in the correctness of the QCD calculations necessary for the determination of the CKM matrix element $|V_{cb}|$. In the measurement presented in this chapter, the signal decay is reconstructed as a single high momentum track identified as electron or muon. The hadronic final state remains entirely unreconstructed. Such measurement is impossible at a hadron collider experiment like LHCb, which relies on the reconstruction of the B_s vertex from multiple tracks. The simplicity of the signal is on the one hand advantageous for the measurement, but comes also along with a difficulty. The advantage is that a single high-momentum track can be reconstructed with a high efficiency. Together with a $B_s \to X\ell\nu$ branching fraction of about 10 % (cf. Tab. 1.1), this leads to a high signal yield. On the other hand, it is very hard to say if a correctly identified lepton stems from a $B_s \to X\ell\nu$ decay or rather a $B \to X\ell\nu$ decay. Figure 7.1 illustrates that the lepton momentum spectra in the lab frame of the two decays look practically identical. Hence, one has to find a way how to distinguish events with B_s decays from events with B decays by other

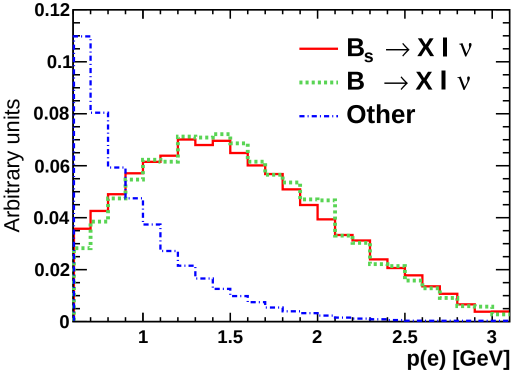

Figure 7.1: Simulated distributions of the momentum in the lab frame of different categories of lepton candidates. The "other" category contains lepton candidates from secondary decays and misidentified hadrons.

means. Here, the pair production of B_s mesons in $\Upsilon(5S)$ decays comes into play. One of the B_s mesons can be fully or partially reconstructed to identify an event with B_s mesons, while the $B_s \to X\ell\nu$ signal decay can be then studied with the second B_s meson in the event. This technique is referred to as "tagging".

The $B_s \to X\ell\nu$ branching fraction was measured before at the experiments Belle and BaBar. The Belle measurement is based on the first $23.6\,\mathrm{fb}^{-1}$ of the $\Upsilon(5S)$ data set. A D_s meson from the Cabibbo-favoured $B_s \to D_s^{\pm}X$ transition is reconstructed to tag B_s pair events. This leads to a considerable enhancement of the B_s fraction in the tagged sample since the branching fraction $\mathcal{B}(B_s \to D_s^{\pm}X) = [93 \pm 25]\ \%$ is much larger than $\mathcal{B}(B \to D_s X) = [8.3 \pm 0.8]\ \%$ [8]. Only the lepton, ℓ, is reconstructed from the decay $B_s \to X\ell\nu$. This lepton can stem either from the decay of the same B_s meson as the D_s meson or the decay of the second B_s meson event. The former case corresponds to the semi-inclusive analysis described in the previous chapter; the latter case is what one wants for the inclusive analysis. In order to select the events where the D_s meson and the lepton come from decays of different B_s mesons, one chooses solely the combinations with same-sign electric

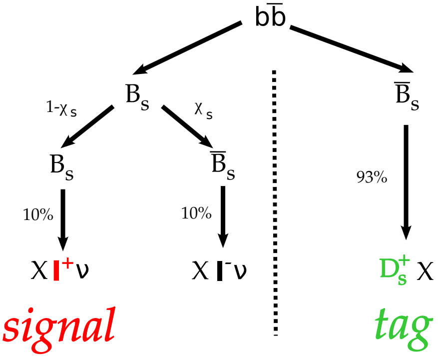

Figure 7.2: Illustration of the "same-sign" D_s tag and the signal loss due to B_s mixing.

charge: "$D_s^+\ell^+$". In the calculation of the $B_s \to X\ell\nu$ branching fraction, it has to be taken into account that due to B_s mixing, the same-sign criterion selects only a fraction of $(1-\chi_s) \approx 50\,\%$ of the signal events as illustrated in Fig. 7.2. In the measurement by BaBar, ϕ mesons are reconstructed to identify B_s pair events [5]. A ϕ tag has the advantage of a higher reconstruction efficiency compared to a D_s tag, but the severe drawback that it does not guarantee that the signal lepton and the tag ϕ stem from different B_s mesons. This means that BaBar's approach is not purely inclusive.

7.1 Analysis overview

The analysis uses the D_s tagging method of the previous Belle analysis described above. Two quantities are measured to extract the $B_s \to X\ell\nu$ branching fraction: the yield of D_s-tagged events, $\mathcal{N}_{D_s}$, and the $D_s^+\ell^+$ yield, $\mathcal{N}_{D_s^+\ell^+}$. For this, D_s mesons are reconstructed in the channel $D_s^+ \to \phi\pi^+$; $\phi \to K^+K^-$. The yields of correctly reconstructed D_s mesons are determined in fits to the reconstructed $K^+K^-\pi^+$ mass distribution. The obtained yields, $\mathcal{N}_{D_s}$ and $\mathcal{N}_{D_s^+\ell^+}$ contain various contributions:

- $e^+e^- \to c\bar{c}$ continuum events, where a D_s meson is produced in the hadronisation;
- B pair events;
- B_s pair events.

The expected yields are estimated from the MC simulation and summarised in Tables 7.1, 7.2 and 7.3. The continuum background is estimated from off-resonance data and subtracted from the yields. The lepton candidates in the selected $D_s^+\ell^+$ pairs are not only *primary* leptons from semileptonic B_s and B decays, but also leptons from secondary decays and misidentified hadrons summarised in the following under the term "'*other*" lepton candidates. The *primary* leptons are characterised by their higher momentum with respect to the *other* lepton candidates (see Fig. 7.1). The yield of *primary* leptons can therefore be extracted from a fit to the reconstructed lepton momentum distribution.

If there was no contribution from B decays, the ratio of the yields,

$$\mathcal{R} = \frac{\mathcal{N}_{D_s^+\ell^+}}{\mathcal{N}_{D_s}}, \tag{7.1}$$

would be directly proportional to the $B_s \to X\ell\nu$ branching fraction. However, also B decays contribute to the final states $D_s^+\ell^+$ and D_s. Using the notation $\mathcal{N}(B_s)$ and $\mathcal{N}(B)$ for the corresponding contribution from B_s and B decays, respectively, the measured ratio can be written as

$$\mathcal{R} = \frac{\mathcal{N}_{D_s^+\ell^+}}{\mathcal{N}_{D_s}} = \frac{\mathcal{N}_{D_s^+\ell^+}(B_s) + \mathcal{N}_{D_s^+\ell^+}(B)}{\mathcal{N}_{D_s}(B_s) + \mathcal{N}_{D_s}(B)}\,. \tag{7.2}$$

To extract the $B_s \to X\ell\nu$ branching fraction from $\mathcal{R}$, the contamination with B decays in the numerator and denominator needs to be estimated. In the preliminary Belle measurement, the B background was estimated using $\Upsilon(4S)$ data. This is, however, problematic as there is no one-to-one correspondence between the B production at the $\Upsilon(4S)$ and $\Upsilon(5S)$ resonance (cf. Ch. 4). In this thesis, the B background is therefore estimated from existing measurements of $B_{(s)}$ branching fractions and $B_{(s)}$ production fractions at the $\Upsilon(5S)$ resonance. The estimation of the B background from external measurements has the advantage, that if the accuracy of these measurements improves in the future, the determination of the $\mathcal{N}_{D_s^+\ell^+}$ and $\mathcal{N}_{D_s}$ yields will not have to be repeated and only the calculation of the $B_s \to X\ell\nu$ branching fraction has to be updated.

7.2 Measurement of the inclusive D_s yield

The inclusive D_s yields are measured in 20 equal bins of the normalised D_s momentum, $x(D_s) = p^*_{D_s} / \sqrt{s/4 - M^2_{D_s}}$, in the interval 0.0 . . . 1.0. The D_s yields are determined from binned extended maximum likelihood fits to the reconstructed $K^+K^-\pi^+$ mass distributions. The fit PDFs are the same as for the semi-inclusive analysis: the signal PDF is modelled as the sum of two Gaussian functions and the PDF for the combinatorial background is a first order Chebychev polynomial (cf. Sec. 6.3.1). In the measurement, only the part of the distribution with $x(D_s) < 0.5$ is considered as signal region. The part with $x(D_s) > 0.5$ contains practically only continuum events and serves as control region for the continuum modelling. The results of the fit to the sample of D_s mesons reconstructed in $\Upsilon(5S)$ data in the signal region $x(D_s) < 0.5$ are depicted in Fig. 7.3. The corresponding $x(D_s)$ distribution is shown in Fig. 7.4. The $K^+K^-\pi^+$ mass fits are performed independently in each $x(D_s)$ bin to allow for differences in the PDF parameters. Figures 7.5 and 7.5 show the fit results for the PDF parameters in the individual $x(D_s)$ bins.

To estimate the yield of D_s mesons coming from the continuum background in the $\Upsilon(5S)$ data, the identical fitting procedure is applied to a sample of reconstructed D_s mesons in off-resonance data. The yields obtained from this off-resonance sample are multiplied with the scale factor from Eq. 4.3 to estimate the corresponding yields in $\Upsilon(5S)$ data. Figure 7.4 includes, as orange histogram, the $x(D_s)$ spectrum from scaled off-resonance data. The good agreement between the distributions from $\Upsilon(5S)$ and off-resonance data in the control region, $x(D_s) > 0.5$, justifies the use of the off-resonance sample for the estimation of the continuum background. The D_s yields in the $\Upsilon(5S)$ and off-resonance

	B_s decays		B decays		$e^+e^- \to c\bar{c}$	
	Eff. [%]	$N_{\text{evts.}}$	Eff. [%]	$N_{\text{evts.}}$	Eff. [%]	$N_{\text{evts.}}$
Generated	100.00 ± 0.08	1495948	100.00 ± 0.12	677539	100.00 ± 0.05	4458688
Reconstructed	32.46 ± 0.05	485575	32.68 ± 0.07	221419	35.00 ± 0.03	1560646
$\lvert\cos\theta_{\text{hel}}\rvert > 0.5$	28.18 ± 0.04	421499	28.42 ± 0.06	192545	30.42 ± 0.03	1356328
$x(D_s) < 0.5$	28.13 ± 0.04	420756	28.36 ± 0.06	192183	10.45 ± 0.02	466088

Table 7.1: D_s reconstruction efficiencies for the D_s^+ sample.

	B_s decays		B decays	
	Eff. [%]	$N_{\text{evts.}}$	Eff. [%]	$N_{\text{evts.}}$
Generated	100.00 ± 0.38	69402	100.00 ± 0.84	14309
Reconstructed	33.20 ± 0.22	23041	32.66 ± 0.48	4673
$\lvert\cos\theta_{\text{hel}}\rvert > 0.5$	28.86 ± 0.20	20026	28.21 ± 0.44	4036
$x(D_s) < 0.5$	28.80 ± 0.20	19987	28.17 ± 0.44	4031

Table 7.2: D_s reconstruction efficiencies for the $D_s^+ e^+$ sample. The reconstruction efficiency of the electron is *not* included.

	B_s decays		B decays	
	Eff. [%]	$N_{\text{evts.}}$	Eff. [%]	$N_{\text{evts.}}$
Generated	100.00 ± 0.38	69191	100.00 ± 0.84	14255
Reconstructed	33.43 ± 0.22	23128	34.08 ± 0.49	4858
$\lvert\cos\theta_{\text{hel}}\rvert > 0.5$	29.11 ± 0.21	20139	29.68 ± 0.46	4231
$x(D_s) < 0.5$	29.06 ± 0.20	20107	29.60 ± 0.46	4219

Table 7.3: D_s reconstruction efficiencies for the $D_s^+ \mu^+$ sample. The reconstruction efficiency of the muon is *not* included.

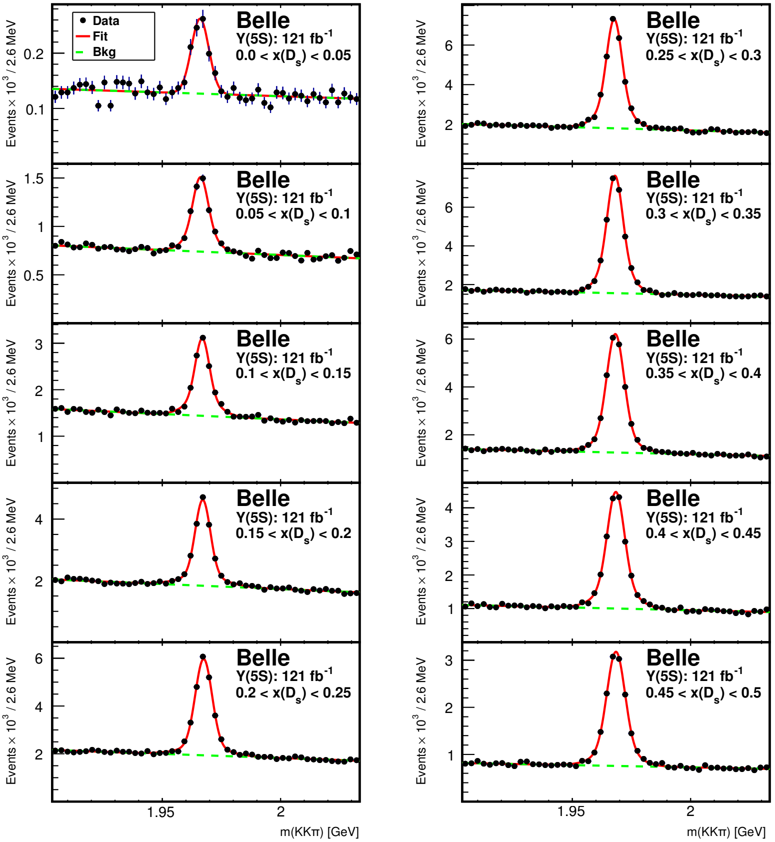

Figure 7.3: $K^+K^-\pi^+$ mass fits in bins of $x(D_s)$. The solid red curve represents the result of the fit, and the dashed green line corresponds to the fitted background distribution.

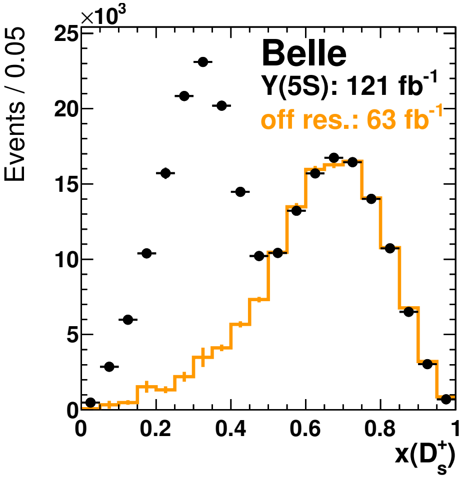

Figure 7.4: $x(D_s)$ spectra obtained from the $K^+K^-\pi^+$ mass fits.

sample are listed in Table 7.4 for the signal and control regions. The continuum subtracted yield of D_s mesons from $B_{(s)}$ decays is

$$N_{D_s} = 97665 \pm 1309\,. \tag{7.3}$$

The continuum subtracted yield in the control region is consistent with the expectation of zero.

N_{D_s}	$x(D_s) < 0.5$	$x(D_s) > 0.5$
$\Upsilon(5S)$	124249 ± 770	107497 ± 424
Off-resonance	14708 ± 542	59959 ± 322
Scaled off-resonance	26583 ± 1058	108369 ± 1727
Continuum subtracted	97665 ± 1309	-872 ± 1778

Table 7.4: Yields of the $K^+K^-\pi^+$ mass fits.

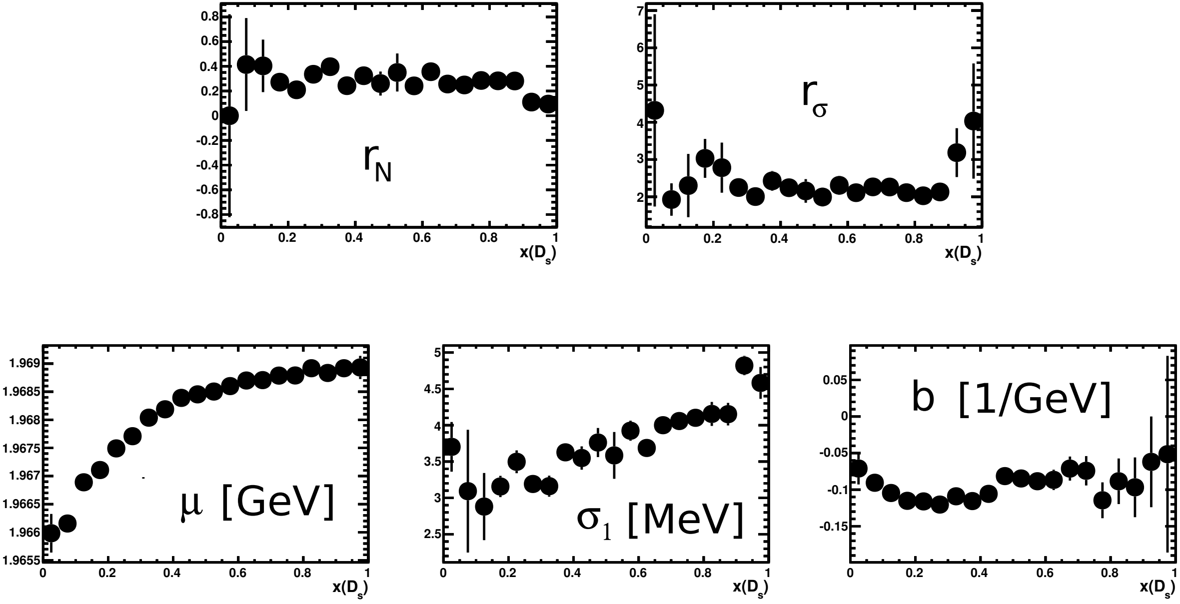

Figure 7.5: Variation of the PDF parameters, r_σ, r_N, μ, σ_1 and b, with $x(D_s)$. The parameters are determined from the $K^+K^-\pi^+$ mass fits to the D_s sample reconstructed in $\Upsilon(5S)$ data.

7.3 Measurement of the $D_s^+\ell^+$ yields

The measurement of the $D_s^+\ell^+$ yields is performed for electrons and muons separately because they are identified with different subdetectors (cf. Sec. 5.3). The yield of correctly reconstructed D_s mesons within the sample of selected $D_s^+\ell^+$ pair events is determined with the $K^+K^-\pi^+$ mass fit procedure that is used for the measurement of the inclusive D_s^+ yield. The mass fits are performed in 9 bins of the lepton momentum measured in the laboratory frame in the range $p_\ell = 0.6 \ldots 0.9\,\text{GeV}$. The $D_s^+\ell^+$ samples contain a factor of 20 less events than the D_s sample. The statistical power is thus not sufficient to determine all PDF parameters in the $K^+K^-\pi^+$ mass fits. Therefore, the parameters r_σ and r_N are fixed to the values $r_\sigma = 2.15 \pm 0.07$ and $r_N = 0.29 \pm 0.02$ determined by fitting a constant function to the distributions in Fig. 7.5. The other PDF parameters, μ, σ_1 and b, are determined from fits to the $K^+K^-\pi^+$ mass distribution of the full $D_s^+\ell^+$ samples without the binning in p_ℓ and then fixed to the obtained values. The results of the fits to the full $D_s^+\ell^+$ samples are shown in Fig. 7.6. In the fits in bins of p_ℓ, only the normalisations of the signal and the background are varied. The mass fits in the individual p_ℓ bins are shown in Figs. B.6 and B.7 in the Appendix.

The D_s yields from continuum events are estimated from the off-resonance samples analogous to the measurement of the inclusive D_s yields. The small difference in the lepton momentum spectrum between the $\Upsilon(5S)$ and the off-resonance data is estimated from the MC simulation and corrected by a bin-by-bin re-weighting. The resulting continuum p_ℓ spectrum is subtracted from the spectrum obtained from $\Upsilon(5S)$ data. The continuum-subtracted p_ℓ distributions are shown in Fig. 7.7 and the integrated yields are listed in Table 7.5.

The continuum-subtracted $D_s^+\ell^+$ yields contain two categories of lepton candidates: 1. *primary* leptons from semileptonic $B_{(s)}$ decays, and 2. *other* lepton candidates. Since the shapes of the lepton momentum spectra of the two components are different, their normalisations can be extracted by a fit to the measured spectrum. Histograms describing the shapes of the lepton momentum distribution of the *primary* and *other*

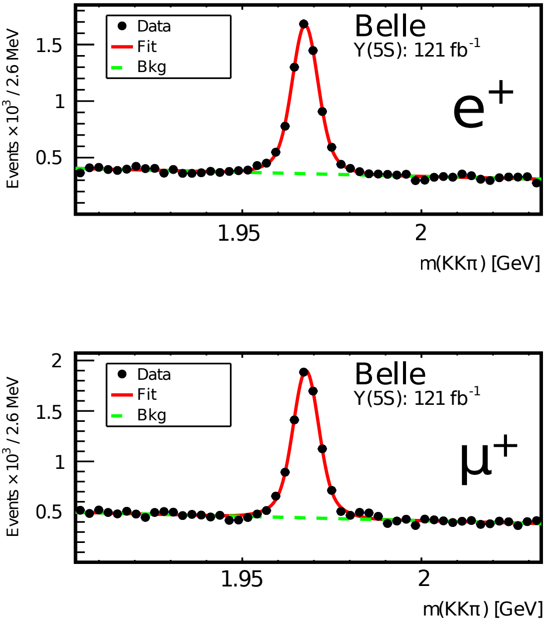

Figure 7.6: $K^+K^-\pi^+$ mass fits of the full $D_s^+e^+$ and the $D_s^+\mu^+$ samples without the binning in p_ℓ.

	Electrons	Muons
$\Upsilon(5S)$ data	5079 ± 91	5617 ± 98
Off-resonance data	120 ± 25	181 ± 44
Scaled off resonance data	230 ± 53	337 ± 82
Continuum subtracted	4848 ± 106	5280 ± 128

Table 7.5: Results of the $K^+K^-\pi^+$ mass fits to the $D_s^+\ell^+$ samples. The uncertainties are statistical and systematic.

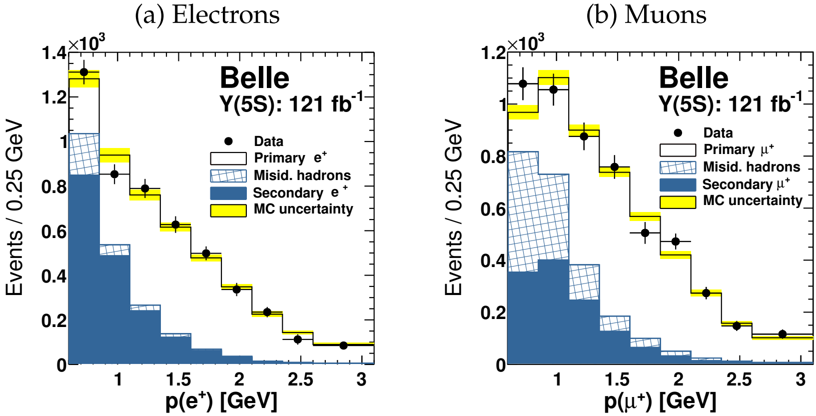
(a) Electrons

(b) Muons

Figure 7.7: Lepton momentum spectra of reconstructed $D_s^+\ell^+$ events after the continuum background subtraction. The stacked histograms represent the result of the two-component fit of 1. *primary* leptons and 2. *other* lepton candidates (misidentified hadrons and secondary leptons).

components are derived from the MC simulation. The normalisations of the two components are determined by minimising

$$\chi^2 = \sum_{\text{bins } i} \frac{\left(D_i - D \cdot \left[a_{\text{primary}} \cdot N_{i,\text{primary}} / N_{\text{primary}} + a_{\text{other}} \cdot N_{i,\text{other}} / N_{\text{other}}\right]\right)^2}{(\Delta D_i)^2 + D^2 \cdot \left[\left(\Delta N_{i,\text{primary}} / N_{\text{primary}}\right)^2 + \left(\Delta N_{i,\text{other}} / N_{\text{other}}\right)^2\right]}, \tag{7.4}$$

where the following nomenclature is used:

i: Lepton momentum bin,
D_i: Measured D_s yield in bin i,
D: Total measured D_s yield (sum over all bins i),
ΔD_i: Statistical uncertainty of the fit to the $K^+K^-\pi^+$ mass distribution of bin i,
j: MC component (primary or other))
a_j: Fraction of data events that belongs to component j
$N_{i,j}$: MC prediction for the component j in bin i,
N_j: Total D_s yield predicted from the component j,
$\Delta N_{i,j}$: Quadratic sum of the statistical and systematic uncertainties of the MC prediction for the component j in bin i.

The fit takes the statistical uncertainties from the $K^+K^-\pi^+$ mass fits into account. The Poissonian errors due to the MC statistics are approximated as Gaussian errors. The systematic uncertainties of the MC simulation comprising the lepton efficiency, the lepton misidentification rate, the continuum corrections and the composition of the fit components are also considered in the fit. The only floating parameters in the fit are the fractions a_j. The signal yield, N_{primary}, is obtained from the fitted fraction, a_{primary}, via

$$N_{\text{primary}} = \frac{a_{\text{primary}} \cdot D}{A_\ell^{\text{mom}} \cdot A_\ell^{\text{geo}} \cdot \epsilon_\ell} \,. \tag{7.5}$$

The signal acceptance, A_ℓ, for the lepton momentum selection $p_\ell > 0.6\,\text{GeV}$ is 93 % and 94 % for electrons and muons respectively. The product of the lepton identification and reconstruction efficiency, and the geometrical acceptance of the detector, $A_\ell^{\text{geo}} \cdot \epsilon_\ell$, is 77 % for electrons and 71 % for muons. The fit results and the signal yields are summarised in Table 7.6.

	Electrons	Muons
$p_\ell = 0.6\,\text{GeV} \ldots 3.1\,\text{GeV}$		
Primary leptons (fit)	2802 ± 143	2922 ± 161
Other leptons (fit)	2111 ± 162	2306 ± 201
χ^2/ndf	$3.6/7$	$5.7/7$
$p_\ell = 0.0\,\text{GeV} \ldots \infty\,\text{GeV}$		
Primary leptons, N_primary	3914 ± 201	4371 ± 240

Table 7.6: Results of the two-component χ^2 fit to the p_ℓ distribution obtained from $K^+K^-\pi^+$ mass fits.

7.4 Calculation of the ratio $\mathcal{R}$

The ratio of the $D_s^+\ell^+$ yield to the D_s yield is calculated from the obtained fit results using the relation

$$\mathcal{R}_\ell = \frac{\mathcal{N}_{D_s^+\ell^+}}{\mathcal{N}_{D_s}} = \frac{N_\text{primary}}{N_{D_s}} \cdot \frac{\epsilon_{K^+K^-\pi^+}(D_s)}{\epsilon_{K^+K^-\pi^+}(D_s^+\ell^+)} \, . \tag{7.6}$$

The small differences in the $K^+K^-\pi^+$ reconstruction efficiencies, $\epsilon_{K^+K^-\pi^+}$, between the D_s and $D_s^+\ell^+$ samples are taken into account. The efficiencies are calculated as weighted averages of the efficiencies for B_s and B events given in Tables 7.1, 7.2 and 7.3:

$$\begin{aligned} \epsilon_{K^+K^-\pi^+}(D_s) &= 28.2\,\%\,, \\ \epsilon_{K^+K^-\pi^+}(D_s^+e^+) &= 28.7\,\%\,, \\ \epsilon_{K^+K^-\pi^+}(D_s^+\mu^+) &= 29.2\,\%\,. \end{aligned} \tag{7.7}$$

The D_s signal peak does not contain only contributions from $D_s\phi\pi; \phi \to K^+K^-$ decays, but also a small amount of cross-feed from other D_s decay modes such as S-wave $D_s \to f_0(980)\pi$ decays and non-resonant $D_s^+ \to K^+K^-\pi^+$ decays [108, 109, 111]. In the determination of the efficiencies, $\epsilon_{K^+K^-\pi^+}$, this cross-feed is interpreted as signal. One obtains the following ratios:

$$\begin{aligned}\mathcal{R}_e = [&394 \pm 18(\text{stat.uncorr.}) \pm 5(\text{stat.corr.})\\ &\pm 4(\text{syst.uncorr.}) \pm 12(\text{syst.corr.})] \times 10^4\,,\end{aligned} \tag{7.8}$$

$$\begin{aligned}\mathcal{R}_\mu = [&432 \pm 21(\text{stat.uncorr.}) \pm 6(\text{stat.corr.})\\ &\pm 9(\text{syst.uncorr.}) \pm 15(\text{syst.corr.})] \times 10^4\,.\end{aligned} \tag{7.9}$$

The correlated and uncorrelated parts of the statistical and systematic uncertainties are quoted separately. The evaluation of the systematic uncertainties is discussed in Sec. 7.5. Considering the uncorrelated uncertainties only, the two measurements are in agreement within 1.3 σ. The combination of the two measurements, taking into account the correlations, gives

$$\mathcal{R}_{\text{meas.}} = [409 \pm 15(\text{stat.}) \pm 14(\text{syst.})] \times 10^4\,. \tag{7.10}$$

7.5 Evaluation of uncertainties

In the following, the uncertainties of the measurement of the ratio $\mathcal{R}$ are discussed. Table 7.7 summarises the systematic uncertainties, which comprise the detector simulation, the fitting procedure, and the signal and background MC modelling.

7.5.1 Statistical uncertainty

The uncertainties of the primary lepton yields, N_{primary}, contain both the statistical uncertainty of the data sample and the MC uncertainties. In order to estimate the pure statistical uncertainty, the fits are repeated with the MC uncertainties, $\Delta N_{i,j}$, in Eq. 7.4 set to zero. The obtained relative statistical uncertainties are

$$\frac{\Delta_{\text{stat}} N(D_s^+ e^+)}{N(D_s^+ e^+)} = \frac{179}{3910} = 4.6\,\%\,, \tag{7.11}$$

		$\Delta\mathcal{R}/\mathcal{R}$ [%]	
		e	μ
	Detector		
⊠	Tracking efficiency	0.4	0.4
□	Lepton identification	0.7	1.4
□	Hadron → lepton mis-identification probability	0.0	0.1
	$K^+K^-\pi^+$ mass fits		
⊠	Signal and background shapes	2.0	2.2
	Background		
⊠	Scale factor for continuum subtraction	0.4	0.4
⊠	Lepton momentum correction for off-resonance data	1.0	1.0
⊠	Variation of the fraction of secondary leptons from X_c and τ	0.9	0.6
□	Variation of the fraction of secondary leptons from other sources	0.2	0.2
□	Variation of the fraction of fake leptons	0.4	1.4
	Signal modelling		
⊠	Form factor model	1.0	1.0
⊠	Variation of the contributions from $B_{(s)} \to X\ell\nu$ modes	1.6	2.1
□	D_s reconstruction efficiency (statistical error of MC simulation)	0.8	0.8
	Correlated (⊠)	3.1	3.6
	Uncorrelated (□)	1.1	2.1
	Total	3.3	4.0

Table 7.7: Overview of the systematic uncertainties. Correlations between the electron and muon measurements are marked with "⊠".

$$\frac{\Delta_{\text{stat}} N(D_s^+ \mu^+)}{N(D_s^+ \mu^+)} = \frac{209}{4328} = 4.8\,\% \,. \tag{7.12}$$

7.5.2 Detector simulation

Uncertainties related to the D_s reconstruction cancel in the ratio $\mathcal{R}$. This cancellation applies to the track reconstruction uncertainties for kaons and pions as well as the uncertainties due to the kaon and pion efficiency calibration described in Sec. 5.2. The track reconstruction uncertainty for the remaining lepton track is 0.35 %. The uncertainty on the calibration of the lepton identification is determined as explained in Sec. 5.3 and evaluated for each p_ℓ bin. The simultaneous variation of the MC predictions in all p_ℓ bins by their uncertainties results in a change of the ratio $\mathcal{R}$ of 0.7 % and 1.4 % for the electron and muon mode, respectively. The uncertainty due to the "hadron ⇒ lepton" misidentification probabilities is also determined by a simultaneously varying the MC predictions in all bins by their uncertainties. The impact on the ratio $\mathcal{R}$ is found to be negligible.

7.5.3 Fitting procedure

Imperfections in the modelling of the D_s peak in the $K^+K^-\pi^+$ mass fits cancel in the ratio $\mathcal{R}$. However, the effect of fixing the PDF parameters in the fits to the $D_s^+\ell^+$ samples needs to be evaluated. For this, the fixed parameters are varied within their uncertainties and the observed change of the ratio $\mathcal{R}$ is assigned as systematic uncertainty. The sum of the uncertainties due to the fixing of the individual PDF parameters in the fits is 2.0 % for the electron mode and 2.2 % for the muon mode.

7.5.4 Background-related uncertainties

The uncertainty on the continuum scale factor from Eq. 4.3 due to the measurements of the $\Upsilon(5S)$ and off-resonance luminosities leads to a systematic uncertainty of the ratio $\mathcal{R}$ of 0.4 %. The statistical uncertainty of the MC sample to determine the lepton momentum correction between off-resonance and $\Upsilon(5S)$ data for the continuum background in the measurement of the $D_s^+\ell^+$ yield adds a further 1.0 % uncertainty to the ratio $\mathcal{R}$.

The *other* lepton component is composed of several subcomponents with similar but not completely identical shapes, as illustrated in Fig. 7.8. The subcomponents are grouped into misidentified hadrons ("fake lepton candidates"), and secondary leptons from X_c decays, from τ decays and from other sources. The fractions of these subcomponents in the MC simulation are given in Table 7.8. It is clear that the shape of the *other* lepton component depends on the chosen fractions in the MC simulation. The systematic uncertainty on the composition of the *other* component is conservatively evaluated by testing the effect of a 30 % variation of the normalisation of each subcomponent, which reflects the current level of knowledge of the B_s branching fractions. The results of these variations are given in Table 7.8. The quadratic sums of all variations are 1.0 % and 1.6 % for the electron and muon mode, respectively.

An interesting particularity of B_s decays is the higher tau production rate compared to B decays. While the $B_s \to \tau\nu$ and $B_s \to X\tau\nu$ branching fractions are expected to be analogous to the ones in B decays, additional tau leptons are produced in decays of D_s mesons from $B_s \to D_s X$. The $D_s^+ \to \tau^+\nu$ branching fraction is with $[5.43 \pm 0.31]$ % [8] much higher than the corresponding $D^+ \to \tau^+\nu$ branching fraction, which has an upper limit of 1.2×10^{-3} at the 90 % confidence level [112]. Many of the secondary leptons from τ decays are in fact "tertiary" leptons from the decay chain $B_s \to D_s \to \tau \to \ell$. Because of the large τ mass, the momentum spectrum of these tertiary leptons is very similar to the one of the secondary leptons from the decay chain $B_s \to \tau \to \ell$.

7.5.5 Signal modelling

The shape of the *primary* lepton momentum spectrum in the simulation is determined by the composition of the semileptonic width and the form factor model used for the MC generation. The shape has of course a direct influence on the result of the χ^2 fit to the p_ℓ spectrum. It also determines the signal acceptance, A_ℓ^{mom}, in Eq. 7.5. Figure 7.9 illustrates the dependence of A_ℓ on the p_ℓ threshold for different contributions to the semileptonic width. The threshold in the analysis selection is set to $p_\ell > 0.6\,\text{GeV}$, where the acceptance differences are small.

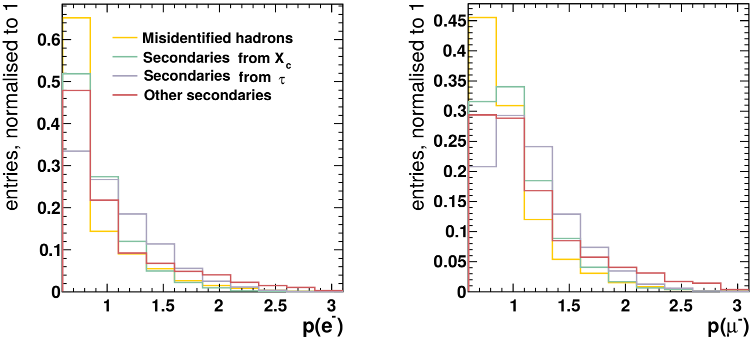

Figure 7.8: Shapes of the p_ℓ spectra of the different contributions to the *other* lepton component: misidentified hadrons and secondary leptons from X_c decays, from τ decays and from other sources.

	Fraction [%]		$\Delta\mathcal{R}/\mathcal{R}$ [%]	
	e	μ	e	μ
Secondary leptons from X_c	58	36	0.6	0.5
Secondary leptons from τ	7	5	0.7	0.4
Secondary leptons from other sources	10	5	0.2	0.2
Hadrons misidentified as leptons	25	53	0.4	1.4

Table 7.8: Composition of the *other* lepton momentum spectrum in the fit region, $p_\ell = 0.6\,\text{GeV} \ldots 3.1\,\text{GeV}$, and the impact of a 30 % variation of the individual fractions on the ratio $\mathcal{R}$.

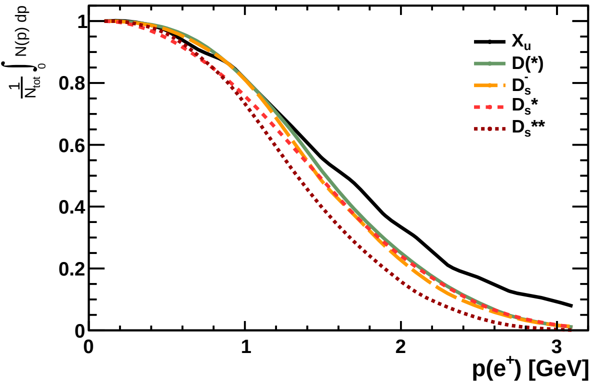

Figure 7.9: Signal acceptance, A_ℓ, as a function of the lower lepton momentum threshold for the individual contributions to the inclusive semileptonic width.

The following contributions are distinguished for the evaluation of the uncertainty due to the signal MC composition: $B_s \to D_s\ell\nu$, $B_s \to D_s^*\ell\nu$, $B_s \to D_s^{**}\ell\nu$ and $B \to D^{(*,**)}\ell\nu$. The fraction of $B_s \to X_u\ell\nu$ decays is expected to be at the order of a few percent from $\mathrm{SU(3)}_{\mathrm{flavour}}$ symmetry [113] and is thus neglected. Each contribution is varied by 30 % and the resulting deviation of the ratio $\mathcal{R}$ from its nominal value is assigned as systematic uncertainty. Table 7.9 summarises the uncertainties arising from the individual variations. The summed systematic uncertainties due to the signal composition are 1.6 % and 2.1 % for electrons and muons, respectively.

The systematic uncertainty due to the $D_s\ell\nu$ and $D_s^*\ell\nu$ form factors is evaluated in the same way as in the $B_s \to D_sX\ell\nu$ analysis (cf. Sec. 6.6.2); it is 1.0 % for both electron and muon mode. No form factor uncertainty is assigned to the $D_s^{**}\ell\nu$ contributions.

Mode	$\Delta\mathcal{R}_e/\mathcal{R}_e$ [%]	$\Delta\mathcal{R}_\mu/\mathcal{R}_\mu$ [%]
$B_s \to D_s\ell\nu$	0.2	0.3
$B_s \to D_s^*\ell\nu$	1.1	1.8
$B_s \to D_s^{**}\ell\nu$	1.2	1.1
$B \to D^{(*,**)}\ell\nu$	0.1	0.2

Table 7.9: Systematic uncertainties on the ratio $\mathcal{R}$ due to a 30 % variation of the individual contributions.

7.6 Branching fraction calculation and results

In order to extract the inclusive semileptonic branching fraction from the measured ratio $\mathcal{R}$, the expressions for $\mathcal{N}_{D_s}(B_s)$, $\mathcal{N}_{D_s}(B)$, $\mathcal{N}_{D_s^+\ell^+}(B_s)$ and $\mathcal{N}_{D_s^+\ell^+}(B)$ in Eq. 7.2 have to be written down explicitly involving the results from external measurements. These measurements include the B_s and B production fractions introduced in Sec. 4 and severalf B_s and B branching fractions. An overview of the external parameters is presented in Table 7.10. The branching fraction $\mathcal{B}(B_s \to X\ell\nu)$ in the formula for $\mathcal{N}_{D_s^+\ell^+}(B_s)$ is the only unknown in Eq. 7.2. The total number of $b\bar{b}$ pairs produced in $\Upsilon(5S)$ decays, $N_{b\bar{b}}$, appears in each contribution $\mathcal{N}$ and therefore cancels in the ratio $\mathcal{R}$. The inclusive D_s production rates from B_s and B decays are given by

$$\mathcal{N}_{D_s}(B_s)/N_{b\bar{b}} = 2 \cdot f_s \cdot \mathcal{B}(B_s \to D_s X)\,, \tag{7.13}$$

$$\mathcal{N}_{D_s}(B)/N_{b\bar{b}} = 2 \cdot f_d \cdot \mathcal{B}(B^0 \to D_s X) + 2 \cdot f_u \cdot \mathcal{B}(B^+ \to D_s X)\,. \tag{7.14}$$

The factor of 2 takes into account that $B_{(s)}$ mesons are produced in pairs, i.e. the D_s meson can stem from the decay of either $B_{(s)}$ meson. The expression for $\mathcal{N}_{D_s^+\ell^+}(B_s)$ is also straightforward, because the mixing probability χ_s is 50 % independent of the CP eigenstate in which the B_s meson pair is produced (cf. Sec. 2.1). One can make the replacement $\chi_s = (1-\chi_s)$ and obtains

$$\begin{aligned}\mathcal{N}_{D_s^+\ell^+}(B_s)/N_{b\bar{b}} &= \mathcal{B}(B_s \to X\ell\nu) \cdot \chi_s \cdot 2 \cdot f_s \cdot \mathcal{B}(B_s \to D_s X) \\ &= \mathcal{B}(B_s \to X\ell\nu) \cdot \chi_s \cdot \mathcal{N}_{D_s}(B_s)/N_{b\bar{b}}\,.\end{aligned} \tag{7.15}$$

Parameter	Value	$\lvert\Delta\mathcal{B}/\mathcal{B}\rvert$ [%]
$f_u = \mathcal{B}(\Upsilon(5S) \to B^+X)/2$	[36.1 ± 3.2] % [77]	0.8
$f_d = \mathcal{B}(B)\Upsilon(5S) \to B^0X/2$	[38.5 ± 4.2] % [77]	0.6
f_s	[19.9 ± 3.0] %	2.4
$\mathcal{B}(B_s \to D_s^{\pm}X)$	[93 ± 25] %	4.4
$\mathcal{B}(B^+ \to D_s^+X)$	[7.9 ± 1.4] %	2.2
$\mathcal{B}(B^0 \to D_s^+X)$	[10.3 ± 2.1] %	1.7
$\mathcal{B}(B^0 \to D_s^-X)$	[1.5 ± 0.8] % [114]	1.1
$\mathcal{B}(B^+ \to D_s^-X)$	[1.1 ± 0.4] %	0.9
$\mathcal{B}(B^0 \to X\ell^+\nu_\ell)$	[10.33 ± 0.28] %	0.4
$\mathcal{B}(B^+ \to X\ell^+\nu_\ell)$	[10.99 ± 0.28] %	0.1
$F_{B^*\bar{B}^*}$	[38.1 ± 3.4] %	0.1
$F_{B^*\bar{B}}$	[13.7 ± 1.6] %	0.1
$F_{B\bar{B}}$	[5.5 ± 1.6] %	0.0
$F'_{B^*\bar{B}^*\pi}$	[5.9 ± 7.8] % [77]	0.1
$F'_{B^*\bar{B}\pi}$	[41.6 ± 12.1] % [77]	0.2
$F'_{B\bar{B}\pi}$	[0.2 ± 6.8] % [77]	0.0
x_d	0.771 ± 0.008	0.1
χ_s	0.500 ± 0.001	0.2

Table 7.10: Central values of the external parameters used to extract the $B_s \to X\ell\nu$ branching fraction, $\mathcal{B}$, from the measured ratio $\mathcal{R}$. The relative systematic uncertainties $\lvert\Delta\mathcal{B}/\mathcal{B}\rvert$ are given for the combined measurement. The parameters are all taken from Ref. [8] unless otherwise stated.

For the prediction of $\mathcal{N}_{D_s^+\ell^+}(B)$ the individual production modes need to be taken into account for B^+ mesons (no mixing) and B^0 mesons (mixing depending on production mode[1]). The different background processes from B decays leading to the $D_s^+\ell^+$ final state are illustrated in Fig. 7.10. The expression for the B background in the $D_s^+\ell^+$ sample is given by Eq. 7.19 (see end of this chapter) using the notation introduced in Sec. 4.4.

Having defined all terms in Eq. 7.2, the inclusive semileptonic branching fractions can be calculated from the measured ratios $\mathcal{R}_\ell$:

$$\mathcal{B}(B_s \to X\ell\nu) = \frac{[\mathcal{N}_{D_s}(B_s) + \mathcal{N}_{D_s}(B)] \cdot \mathcal{R}_\ell - \mathcal{N}_{D_s^+\ell^+}(B)}{\chi_s \cdot \mathcal{N}_{D_s}(B_s)} \,. \tag{7.16}$$

With the measured ratios $\mathcal{R}_\ell$ one obtains

$$\begin{aligned}
\mathcal{B}(B_s \to X e^+\nu_e) &= [\ \ 9.1 \pm 0.5\,\text{(stat.)}\ \pm 0.4\,\text{(meas.)}\ \pm 0.5\,\text{(ext.)}]\%\,,\\
\mathcal{B}(B_s \to X \mu^+\nu_\mu) &= [10.2 \pm 0.6\,\text{(stat.)}\ \pm 0.5\,\text{(meas.)}\ \pm 0.6\,\text{(ext.)}]\%\,.\\
\mathcal{B}(B_s \to X \ell^+\nu_\ell) &= [\ \ 9.6 \pm 0.4\,\text{(stat.)}\ \pm 0.4\,\text{(meas.)}\ \pm 0.6\,\text{(ext.)}]\%\,.
\end{aligned} \tag{7.17}$$

The first and the second uncertainties are the statistical and the systematic uncertainties of the $\mathcal{R}$ measurement, respectively. Since $\mathcal{B}(B_s \to X\ell\nu)$ is linear in $\mathcal{R}$ (see Eq. 7.16), the branching fraction uncertainty, $\Delta\mathcal{B}(B_s \to X\ell\nu)$, is related to the corresponding uncertainty of the ratio, $\Delta\mathcal{R}$, via:

$$\Delta\mathcal{B}(B_s \to X\ell\nu) = \frac{\mathcal{N}_{D_s}(B_s) + \mathcal{N}_{D_s}(B)}{\chi_s \cdot \mathcal{N}_{D_s}(B_s)} \cdot \Delta\mathcal{R}\,. \tag{7.18}$$

The last uncertainty in Eq. 7.17 is due to the external measurements used to estimate the contributions $\mathcal{N}$. It is estimated in the following way: Each parameter is varied up and down in turn, the branching fraction is recalculated and the larger of the two deviations from the nominal result is assigned as systematic uncertainty. The uncertainties determined from the individual variations are listed in Table 7.10. The combination of these uncertainties is ab initio not trivial, since many of

---

[1] The production modes and $B^0\bar{B}^0$, $B^{0*}\bar{B}^{0*}$ are $C = -1$ states, the mode $B^{0*}\bar{B}^0$ is a $C = +1$ state, and the $B^+\bar{B}^0$ and B^-B^0 combinations are not C eigenstates. In the latter case, the mixing probability of the B^0 is identical to $\chi^{(-)}$ defined in Eq. 2.27 [14].

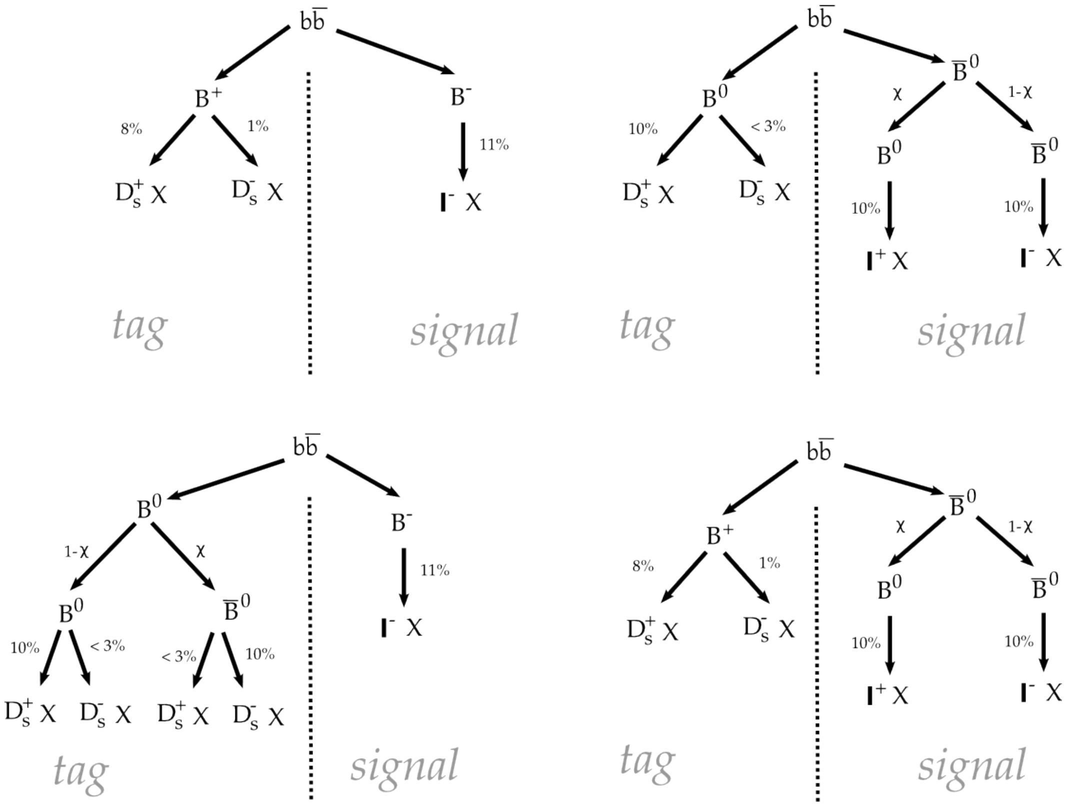

Figure 7.10: Overview of the background processes from *B* meson decays.

the external measurements were performed at Belle and some of them use the same $\Upsilon(5S)$ sample. Since most measurements are based on disjoint sub-samples, they are treated as they would be fully uncorrelated. Also the correlation of the measurement of the ratio $\mathcal{R}$ and the external parameters measured at Belle is negligible, because for most of them only the first $23.6\,\mathrm{fb}^{-1}$ of $\Upsilon(5S)$ data were used. Table 7.11 summarises the contributions of the different systematic uncertainties on the $B_s \to X\ell\nu$ branching fraction measurement.

$$
\begin{aligned}
&\mathcal{N}_{D_s^+\ell^+}(B)/N_{b\bar{b}} = \\
&\quad 2\cdot\frac{f_d}{f_{u,d}}\cdot\ \underbrace{\begin{array}{l}\left[F_{B\bar{B}} + F_{B^*\bar{B}^*} + \frac{1}{3}(f_{u,d}-F_2)\cdot(F'_{B\bar{B}\pi}+F'_{B^*\bar{B}^*\pi}) + (f_{u,d}-F_2)\cdot(1-F'_3)\right]\cdot \\ \left\{\chi_d^{(-)}\cdot\mathcal{B}(B^0\to D_s^+X) + \left(1-\chi_d^{(-)}\right)\cdot\mathcal{B}(B^0\to D_s^-X)\right\}\cdot\mathcal{B}(B^0\to X\ell^+\nu_\ell)\end{array}}_{B^{0(*)}\bar{B}^{0(*)}\text{ pairs, } C\text{ even}} \\
&+\ 2\cdot\frac{f_d}{f_{u,d}}\cdot\ \underbrace{\begin{array}{l}\left[F_{B^*\bar{B}} + \frac{1}{3}(f_{u,d}-F_2)\cdot F'_{B^*\bar{B}\pi})\right]\cdot \\ \left\{\chi_d^{(+)}\cdot\mathcal{B}(B^0\to D_s^+X) + \left(1-\chi_d^{(+)}\right)\cdot\mathcal{B}(B^0\to D_s^-X)\right\}\cdot\mathcal{B}(B^0\to X\ell^+\nu_\ell)\end{array}}_{B^{0}\bar{B}^{0*}\text{ pairs, } C\text{ odd}} \\
&+\ 2\cdot\frac{f_u}{f_{u,d}}\cdot\ \underbrace{\left[F_2 + \frac{1}{3}(f_{u,d}-F_2)\cdot F'_3 + (f_{u,d}-F_2)\cdot(1-F'_3))\right]\cdot\mathcal{B}(B^+\to D_s^-X)\cdot\mathcal{B}(B^+\to X\ell^+\nu_\ell)}_{B^{+(*)}B^{-(*)}\text{ pairs}} \\
&+\ \underbrace{\begin{array}{l}\left[\frac{2}{3}\cdot(f_{u,d}-F_2)\cdot F'_3\right]\cdot \\ \left(\left\{\chi_d^{(-)}\cdot\mathcal{B}(B^0\to D_s^+X) + \left(1-\chi_d^{(-)}\right)\cdot\mathcal{B}(B^0\to D_s^-X)\right\}\cdot\mathcal{B}(B^+\to X\ell^+\nu_\ell) + \right. \\ \left.\left\{\chi_d^{(-)}\cdot\mathcal{B}(B^+\to D_s^+X) + \left(1-\chi_d^{(-)}\right)\cdot\mathcal{B}(B^+\to D_s^-X)\right\}\cdot\mathcal{B}(B^0\to X\ell^+\nu_\ell)\right).\end{array}}_{B^{+(*)}\bar{B}^{0(*)}\text{ and } B^{-(*)}B^{0(*)}\text{ pairs}}
\end{aligned}
\tag{7.19}
$$

Uncertainty [%]	e	μ	e, μ
Detector effects	1.3	1.9	1.2
Fitting procedure	2.4	2.6	2.4
Background modelling	1.8	2.2	1.8
Signal modelling	2.1	2.8	2.4
External parameters (see Tab. 7.10)	5.6	5.9	5.6
Total systematic	6.8	7.5	6.9
Statistical	5.7	6.0	4.2

Table 7.11: Relative uncertainties on the branching fraction $\mathcal{B}(B_s^0 \to X\ell^+\nu_\ell)$ in percent, for the electron and muon mode, and their combination.

CHAPTER 8

Discussion of the results and Outlook

The presented studies of semileptonic B_s decays using the full Belle $\Upsilon(5S)$ data set are a further step towards a more fundamental understanding of semileptonic decays of b-flavoured mesons and fill some of the gaps in the knowledge of semileptonic B_s decays. They represent not only measurements of branching fractions, but also explore the possibilities of further studies of semileptonic B_s decays with the Belle $\Upsilon(5S)$ data set and lay the foundations for future measurements of semileptonic B_s decays with $\Upsilon(5S)$ data.

8.1 Semi-inclusive measurements $B_s \to D_s^{(*)} X\ell\nu$

The branching fraction measurements of the semi-inlcusive semileptonic B_s decays,

$$\mathcal{B}(B_s \to D_s X\ell\nu) = [8.2 \pm 0.2(\text{stat}) \pm 0.6(\text{syst}) \pm 1.4(\text{ext})]\%\,, \tag{8.1}$$

$$\mathcal{B}(B_s \to D_s^* X\ell\nu) = [5.4 \pm 0.4(\text{stat}) \pm 0.4(\text{syst}) \pm 0.9(\text{ext})]\%\,, \tag{8.2}$$

are the first of their kind. The uncertainties are largely dominated by the yet poor knowledge of the number of B_s mesons contained in the sample, $N_{B_s\bar{B}_s}$. The measured $B_s \to D_s X \ell \nu$ branching fraction is in agreement with the expectation from Eq. 6.3 and shows that the semileptonic B_s width is dominated by final states containing a D_s meson. The $B_s \to D_s^* X \ell \nu$ branching fraction can be compared to the different theory predictions for the $B_s \to D_s^* \ell \nu$ branching fraction (see Fig. 2.9). From this, constraints can be deduced on the $B_s \to D_s^{**} \ell \nu$ branching fraction with the D_s^{**} decaying further to D_s^*. A direct comparison with the theory predictions necessitate, however, fully exclusive measurements which require further auxiliary measurements.

The measurement of the $B_s \to D_s X \ell \nu$ yield also provides an estimate for the $B_s^{(*)}\bar{B}_s^{(*)}$ production cross-section at a centre-of-mass energy of $\sqrt{s} = 10.86\,\text{GeV}$,

$$\sigma_{\Upsilon(5S)}(e^+e^- \to B_s^{(*)}\bar{B}_s^{(*)}) = [57.1\ \pm 1.5\,(\text{stat})\ \pm 4.3\,(\text{syst})\ \pm 4.2\,(\text{ext})]\,\text{pb}\,, \tag{8.3}$$

and the number of $B_s^{(*)}\bar{B}_s^{(*)}$ pairs in the Belle $\Upsilon(5S)$ data set:

$$N_{B_s\bar{B}_s} = [6.93 \pm 0.18(\text{stat}) \pm 0.52(\text{syst}) \pm 0.51(\text{ext})] \times 10^6 \tag{8.4}$$

This result is in agreement with the previous Belle measurement, $N_{B_s\bar{B}_s} = (7.1\ \pm\ 1.3)\ \times 10^6$ (cf. Sec. 4.3), but has a significantly smaller uncertainty, namely only 11% compared to 18%. This improvement is a milestone for all existing and future B_s measurements at Belle where the dominating systematic uncertainty is due to $N_{B_s\bar{B}_s}$. Unfortunately, the estimate for $N_{B_s\bar{B}_s}$ from Eq. 8.4 cannot be used in the inclusive $B_s \to X \ell \nu$ analysis because it relies on an assumption for the $B_s \to X \ell \nu$ branching fraction (cf. Eq. 6.3). To obtain the B_s production fraction, the $B_s^{(*)}\bar{B}_s^{(*)}$ cross-section needs to be divided by the $e^+e^- \to b\bar{b}$ cross section:

$$f_s = \frac{\sigma_{\Upsilon(5S)}(e^+e^- \to B_s^{(*)}\bar{B}_s^{(*)})}{\sigma_{\Upsilon(5S)}(e^+e^- \to b\bar{b})} = \frac{[57\ \pm 6]\ \text{pb}}{[340\ \pm 16]\ \text{pb}} = [16.8\ \pm 2.0]\ \%\,. \tag{8.5}$$

The result is in agreement with the world average, $f_s = [19.9 \pm 3.0]$ % [8], and the Belle measurement (cf. Sec. 4.3), $f_s = [17.2 \pm 3.0]$ %.

8.2 Inclusive branching fraction $B_s \to X\ell\nu$

The measurement of the inclusive branching fraction,

$$\mathcal{B}(B_s \to X\ell\nu) = [9.6 \pm 0.4\,(\text{stat.}) \pm 0.7\,(\text{syst.})]\ \%\,, \tag{8.6}$$

is the most precise to date and the most precise of any absolute B_s branching fraction. Similar to most other B_s analyses with $\Upsilon(5S)$ data, the dominant systematic uncertainty is due to the estimation of the B_s production [115]. This uncertainty is 6 %, which is much lower than in other measurements because the parameters f_s and $\mathcal{B}(B_s \to D_s^{\pm}X)$ appear in the numerator and the denominator of the measured ratio $\mathcal{R}$, (see Eq. 7.2) and cancel partially. In other words, the measurement is less affected by the uncertainties of the B_s production parameters because the D_s tag enhances the fraction of B_s events in the selected sample. The measurement is fully inclusive as the same-sign charge requirement on the signal lepton ℓ^+ and the tag D_s^+ ensures that both stem from different B_s decays.

The measurement is consistent with the preliminary Belle result obtained from the first 23.6 fb^{-1} of $\Upsilon(5S)$ data [4],

$$\mathcal{B}(B_s \to X\ell\nu) = [10.2 \pm 0.8\,(\text{stat.}) \pm 0.9\,(\text{syst.})]\ \%\,, \tag{8.7}$$

and the BaBar measurement using 4.25 fb^{-1} of data from an energy scan above the $\Upsilon(4S)$ resonance [5],

$$\mathcal{B}(B_s \to X\ell\nu) = \left[9.5\,^{+2.5}_{-2.0}\,(\text{stat.})\,^{+1.1}_{-1.9}\,(\text{syst.})\right]\%\,. \tag{8.8}$$

It represents a significant improvement of both the statistical and systematic precision. In order to compare the measured branching fraction to theory predictions of the semileptonic width, $\Gamma_{\mathrm{sl}}(B_s)$, one divides by the world average of the B_s life time, $\tau_{B_s} = [1.516 \pm 0.011]\ 10^{-12}\mathrm{s}$ [8]:

$$\Gamma_{\mathrm{sl}}(B_s) = \frac{\mathcal{B}(B_s \to X\ell\nu)}{\tau_{B_s}} = [63.6 \pm 5.4]\ \mathrm{ns}^{-1}\,. \tag{8.9}$$

Figure 8.1 shows the semileptonic width obtained from the combination of the branching fraction measurements and from the individual measurements separately, and a comparison with the BaBar measurement and the expectation from $\mathrm{SU(3)}_{\mathrm{flavour}}$ symmetry. To test $\mathrm{SU(3)}_{\mathrm{flavour}}$ symmetry, the ratio of the B_s to the B^0 width is calculated:

$$\frac{\Gamma_{\mathrm{sl}}(B_s)}{\Gamma_{\mathrm{sl}}(B^0)} = (0.94 \pm 0.08)\,. \tag{8.10}$$

The obtained ratio is consistent with the theory expectations from Eq. 2.80 and Eq. 2.81 within uncertainties. Values outside of the interval $(0.79; 1.08)$ are excluded at the 90 % confidence level. This result is an important test of $\mathrm{SU(3)}_{\mathrm{flavour}}$ symmetry.

8.3 Perspectives for future measurements of semileptonic B_s decays at Belle and Belle II

The preparation work for Belle's successor, Belle II, is currently being completed and the data taking will start in 2016. Hence, the question shall be discussed which studies of semileptonic B_s decays can still be done with the existing $121.4\,\mathrm{fb}^{-1}$ $\Upsilon(5S)$ data set and what possibilities will a larger data set offer in the future. To collect a $B_s\bar{B}_s$ data sample of comparable size as the current Belle $B\bar{B}$ sample containing $N_{B\bar{B}} = 772 \times 10^6$ $B\bar{B}$ pairs, one needs an integrated luminosity of

$$\mathcal{L} = \frac{N_{B\bar{B}}}{f_s \cdot \sigma_{\Upsilon(5S)}(e^+e^- \to b\bar{b})} = \frac{772 \times 10^6}{0.2 \cdot 340\,\mathrm{pb}} \approx 10\,\mathrm{ab}^{-1}\,. \tag{8.11}$$

With such a large data set, rare B_s decay modes will become accessible. Moreover, full reconstruction techniques can be applied, where the de-

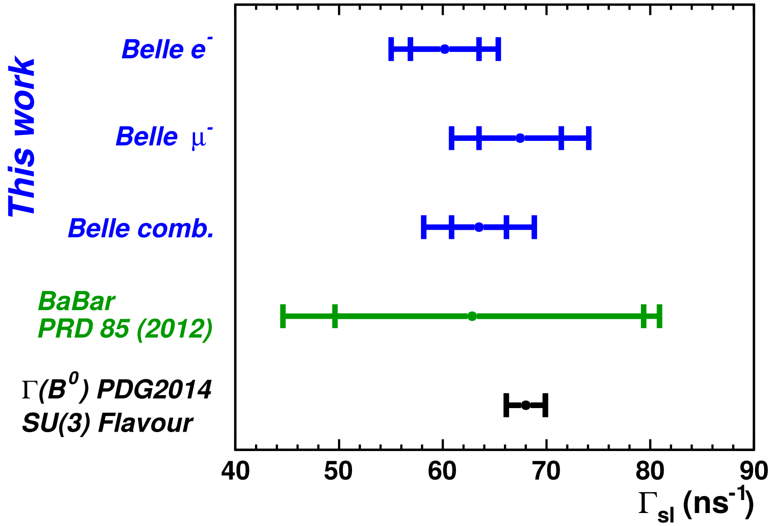

Figure 8.1: Inclusive semileptonic B_s width. From top to bottom: Belle measurements presented in this thesis (electron mode, muon mode and their combination); BaBar measurement [5]; expectation from SU(3)$_{\text{flavour}}$ symmetry calculated from the $B^0 \to X\ell\nu$ branching fraction, the B_s and B^0 lifetimes, and the prediction by Ref. [42].

cay of one B_s meson in the event is reconstructed in either a hadronic or a semileptonic decay mode. The reconstructed B_s meson serves then as "tag" to determine the flavour and the momentum of the second B_s meson in the event, which is used to study the signal decay. The reconstruction of a tag B_s also is a efficient tool to suppress background from continuum processes and B decays. In addition to a full reconstruction, the tag B_s can also be partially reconstructed as it is done in the $B_s \to X\ell\nu$ analysis. In the following, the expected event yields for different analyses of semileptonic B_s decays are estimated for untagged $\Upsilon(5S)$ samples and for different tagging methods applied:

- *Semileptonic tag:* Reconstruction of one B_s in the event in the decay mode $B_s \to D_s X\ell\nu$, where the D_s is reconstructed in the channels $\phi\pi^+$, $K_S K^+$, $\bar{K}^{*0}K^+$, $\phi\rho^+$, $K_S K^{*+}$ and $\bar{K}^{*0}K^{*+}$. The D_s branching fractions sum up to 11 % in total and the expected D_s reconstruction efficiency is about 36 % in average [116];

- *Hadronic tag:* The tag B_s is fully reconstructed in a hadronic mode. The efficiency of the full hadronic B_s tag is estimated to be 0.3% in analogy to the performance of the algorithm implemented for B decays at $\Upsilon(4S)$ [117];

- *Same-sign D_s tag:* Analogous to the $B_s \to X\ell\nu$ analysis described in this thesis, the fraction of B_s events is enhanced by reconstructing a D_s meson with the same-sign charge as the signal lepton. For the D_s reconstruction only the clean decay mode $D_s^+ \to \phi\pi^+$ is considered;

- *Same-sign lepton tag:* A lepton from a semileptonic decay with the same-sign charge as the signal lepton is reconstructed. The combination of two primary leptons with same-sign charges occurs in $B_s\bar{B}_s$ pair events (B_s mixing probability $\chi_s \approx 50\,\%$), but it is less likely for $B^0\bar{B}^0$ pair events and it is impossible for B^+B^- pair events (no mixing). The requirement of the additional same-sign lepton suppresses thus the background from B decays.

The expected B_s yields for the different tagging methods are listed in Table 8.1. Based on these yields, the possibilities for studies of some semileptonic decay modes are evaluated: $B_s \to X\ell\nu$, $B_s \to D_s\ell\nu$, $B_s \to$

Tagging method	$\mathcal{B}_{\text{tag}}$ [%]	ϵ_{tag} [%]	B_s yield [$\times 10^3$]		$N(B_s)/N(B)$
			$121.4\,\text{fb}^{-1}$	$10\,\text{ab}^{-1}$	
Untagged	200	100	14 000	1 157 000	0.3
$B_s \to D_s X \ell \nu$	2	25	70	5800	$\gg 10$
$B_s \to$ hadrons	80	0.3	28	2314	$\gg 10$
Same-sign D_s	2	15	46	3818	6
Same-sign lepton	10	70	980	80 992	1.5

Table 8.1: Expected B_s yields for different tagging methods applied to the $121.4\,\text{fb}^{-1}$ Belle data sample and the corresponding expectation for a potential $10\,\text{ab}^{-1}$ sample collected at Belle II. The estimations are based on the branching fraction, of the reconstructed tag mode, $\mathcal{B}_{\text{tag}}$, and an assumption about its reconstruction efficiency, ϵ_{tag}. The ratio of the number of B_s events to the number of B events, $N(B_s)/N(B)$, is also given.

$D_s^*\ell\nu$, $B_s \to DKX\ell\nu$ and $B_s \to D_s\tau\nu$. The assumed performances are based on the results of this thesis and the experiences of the B analyses with $\Upsilon(4S)$ data. The estimated signal yields are also summarised in Table 8.2.

A measurement of the $B_s \to X\ell\nu$ branching fraction with a fully reconstructed tag B_s meson, i.e. in an environment with low B background, is highly desirable. Such a measurement would be independent of the parameter f_s. The yield expectations in Table 8.2 suggest that a $B_s \to X\ell\nu$ measurement with a fully reconstructed tag B_s is already possible with the Belle $121.4\,\mathrm{fb}^{-1}$ data set. In particular, a measurement with a semileptonic tag seems interesting as this method is easy to implement using the methods for signal extraction presented in this thesis. In the future, the determination of the CKM matrix element $|V_{cb}|$ from a measurement of the lepton energy and hadronic mass moments in $B_s \to X_c\ell\nu$ decays will become feasible with a larger data set at Belle II. This will allow for a comparison with the results obtained from the analysis of semileptonic B decays [39, 118–120].

A measurement of the exclusive $B_s \to D_s^{(*)}\ell\nu$ branching fractions is in principle possible with a fit to distributions like X_{mis}, where the normalisations of the different components of the semileptonic width $D_s\ell\nu$, $D_s^*\ell\nu$ and $D_s^{**}\ell\nu$ are varied (cf. Sec. 6.2). There are, however, several aspects of the simulation which make such measurement challenging:

- The poor precision of the B_s^* mass (see Eq. 4.14) adds a large uncertainty to the width of the X_{mis} signal peak. A complementary measurement of the B_s^* mass with a full B_s^* reconstruction is challenging, because the energy of the photon emitted in the $B_s^* \to B_s\gamma$ decay, $E_\gamma = \left[48.7\,^{+2.3}_{-2.1}\right]$ MeV [8], is just above the photon detection threshold at Belle. An independent measurement of the B_s^* mass, for example at Belle II, could eventually improve the situation.

- The approximation that the $\Upsilon(5S)$ rest frame corresponds to the B_s rest frame is less accurate than in the case of $\Upsilon(4S)$ and B meson. This leads to a worse separation between signal and background in distributions such as X_{mis}. Moreover, differences in the

		$X\ell\nu$	$D_s\ell\nu$	$D_s^*\ell\nu$	$DKX\ell\nu$	$K\ell\nu$	$D_s\tau\nu$
$\mathcal{B}_{\text{sig}}$ [%]		20	0.1	0.3	0.03	0.03	0.02
ϵ_{sig} [%]		70	17	4	17	60	15
Untagged	$121.4\,\text{fb}^{-1}$	Not feasible	2200	1200	760	2500	Not feasible
	$10\,\text{ab}^{-1}$		182 000	101 000	63 000	208 000	
$D_sX\ell\nu$	$121.4\,\text{fb}^{-1}$	9800	11	6	4	13	1
	$10\,\text{ab}^{-1}$	808 000	900	500	310	1000	70
Hadrons	$121.4\,\text{fb}^{-1}$	3900	4	2	2	5	0
	$10\,\text{ab}^{-1}$	324 000	360	200	130	420	27
Same-sign D_s	$121.4\,\text{fb}^{-1}$	6500	7	4	3	8	Not feasible
	$10\,\text{ab}^{-1}$	536 000	600	340	210	690	
Same-sign ℓ	$121.4\,\text{fb}^{-1}$	Not feasible	150	90	50	180	Not feasible
	$10\,\text{ab}^{-1}$		13 000	7000	4400	15 000	

Table 8.2: Expected signal yields for various analyses of semileptonic B_s decays for the different tagging methods listed in Table 8.1. The yields are based on an assumption on the branching fraction of the reconstructed signal mode, $\mathcal{B}_{\text{sig}}$, and its reconstruction efficiency, ϵ_{sig}. The values are based on the analyses in this thesis or they are chosen in analogy to corresponding measurements of semileptonic B decays.

production modes ($B_s^* \bar{B}_s^*$, $B_s^* \bar{B}_s$ and $B_s \bar{B}_s$) have to be taken into account.

- The form factors of semileptonic B_s decays have not been measured yet.
- The D_s^{**} decay modes have to be measured more precisely in order to better understand the cross-feed from $B_s \to D_s^{**} \ell \nu$ decays.

The decays $B_s \to DKX\ell\nu$ were studied already by the D0 and LHCb collaborations [6, 7]. They can also be measured in an untagged analysis based on the present Belle data set. Unfortunately, these measurements will have to use the $N_{B_s \bar{B}_s}$ estimate from the measurement of the inclusive D_s yield and cannot profit from the $N_{B_s \bar{B}_s}$ estimate presented in this thesis (see Eq. 8.4), which it relies on an assumption about the $B_s \to D^0 KX\ell\nu$ branching fraction.

The $B_s \to K\ell\nu$ branching fraction is expected to be around 1.5 % similar to the $B^0 \to \pi\ell\nu$ branching fraction [8, 121–123]. These rare decay modes are of interest for the determination of the CKM matrix element $|V_{ub}|$. The CLEO collaboration demonstrated that a measurement of the $B^0 \to \pi\ell\nu$ branching fraction and an extraction of $|V_{ub}|$ is feasible even with a small data set of only 5×10^6 pairs of B^0 mesons [124]. Hence, a first measurement of $B_s \to K\ell\nu$ should be possible with the current Belle data set. An analysis with fully reconstructed B_s tag, similar to the studies with B mesons in $\Upsilon(4S)$ data [125], will be within the reach of Belle II.

Studies of semileptonic decays with τ leptons are within the most promising fields for discovering “new physics”. Particularly, a measurement recently published by the BaBar collaboration [126], which claims a 3.4σ disagreement of the observed $B \to D^{(*)}\tau\nu$ rates with the standard model is subject to animated debates. Measurements with τ leptons are experimentally challenging because two or three neutrinos escape the detector undetected, depending on the reconstruction channel of the τ meson. Therefore, full reconstruction techniques have to be employed making such measurements with B_s mesons only feasible with the large $\Upsilon(5S)$ data set expected from Belle II.

CHAPTER 9

Conclusion

Semileptonic B_s decays were studied in a semi-inclusive and an inclusive approach, using the 121.4 fb^{-1} data set collected by the Belle detector at the $\Upsilon(5S)$ resonance. The results are summarised in the Table below.

The branching fractions of the semi-inclusive decays $B_s \to D_s X \ell \nu$ and $B_s \to D_s^* X \ell \nu$ were measured for the first time. The measurements are based on the determination of $D_s^{(*)-}\ell^+$ yields in three "counting regions" defined by the kinematics of the $D_s^{(*)-}\ell^+$ pairs. This approach is chosen as it is less sensitive to the modelling of the kinematic distributions of signal decays. The precision of the measurements is systematically limited by the uncertainty on the number of B_s mesons in the data sample. The obtained semi-inclusive $B_s \to D_s^{(*)} X \ell \nu$ branching fractions are in agreement with the sum of the predicted exclusive branching fractions. The measured $B_s \to D_s X \ell \nu$ yield, together with an estimate for the $B_s \to D_s X \ell \nu$ branching fraction, is also used to determine the most precise estimate for the $B_s^{(*)} \bar{B}_s^{(*)}$ production cross-section in e^+e^- collisions at $\sqrt{s} = 10.86\,\mathrm{GeV}$.

The $B_s \to X \ell \nu$ branching fraction was measured with improved precision. A same-sign charge D_s tag is used in this measurement to enhance the fraction of B_s mesons in the selected sample. Therefore, the uncertainty due to the B_s production fraction is reduced, compared to untagged B_s measurements with $\Upsilon(5S)$ data. The $B_s \to X\ell\nu$ branching fraction is extracted from measured D_s and $D_s^+\ell^+$ yields, where the contribution from the remaining B background is estimated from external measurements of B_s and B production and branching fractions. The obtained result is in agreement with the theory expectations that predict only small $\mathrm{SU(3)}_{\mathrm{flavour}}$ symmetry breaking effects.

Quantity	Value	Relative uncertainty	
		This work	Previous
$\mathcal{B}(B_s \to D_s X \ell \nu)$	$[8.2 \pm 0.2(\text{stat}) \pm 0.6(\text{syst}) \pm 1.4(\text{ext})]\ \%$	19 %	—
$\mathcal{B}(B_s \to D_s^* X \ell \nu)$	$[5.4 \pm 0.4(\text{stat}) \pm 0.4(\text{syst}) \pm 0.9(\text{ext})]\ \%$	20 %	—
$\sigma_{\Upsilon(5S)}(e^+e^- \to B_s^{(*)}\bar{B}_s^{(*)})$	$[57.1\ \pm 1.5\,(\text{stat})\ \pm 4.3\,(\text{syst})\ \pm 4.2\,(\text{ext})]\ \text{pb}$	11 %	18 %
$\mathcal{B}(B_s \to X \ell \nu)$	$[9.6\ \pm 0.4\,(\text{stat.})\ \pm 0.7\,(\text{syst.})]\ \%$	8 %	12 %

APPENDIX A

Modelling of semileptonic B_s decays

It goes without saying that the adequate choice of the event generator model and its parameters is extremely important for the analysis of almost any decay or particle reaction. Advances in theory and recent measurements of semileptonic B decays call for a reconsideration of the decisions made at the time, when the Belle MC sample was generated. Therefore, weighting factors are determined for each MC event dependent on the type and the kinematic properties of the semileptonic decay. This approach avoids the repetition of the full detector simulation which is a rather time consuming and computing power intensive process.

A.1 Branching fraction corrections

In Sec. 2.4, various theory publications with different predictions for the exclusive semileptonic B_s branching fractions were cited. In the generation of the MC samples, the branching fractions of semileptonic B_s decays were chosen in analogy to the corresponding B branching frac-

Mode	$\mathcal{B}_{\text{orig}}$ [%]	$\mathcal{B}_{\text{new}}$ [%]	Weight	Ref.
$D_s\ell\nu$	2.10	2.1 ± 0.2	1.00	[29]
$D_s^*\ell\nu$	4.90	5.3 ± 0.5	1.08	[29]
$D_{s1}(2536)\ell\nu$	0.40	0.84 ± 0.09	2.10	[29]
$D_{s0}^*\ell\nu$	0.40	0.36 ± 0.04	0.90	[29]
$D_{s1}(2460)'\ell\nu$	0.70	0.19 ± 0.02	0.27	[29]
$D_{s2}^*\ell\nu$	0.70	0.67 ± 0.07	0.96	[29]
$K^{(*)}\ell\nu$	0.10	—	1.00	—

Table A.1: Composition of the semileptonic width in the MC simulation. The event weight is calculated as the ratio of branching fraction used originally in the simulation, $\mathcal{B}_{\text{orig}}$, and the branching fraction predicted by theory, $\mathcal{B}_{\text{new}}$.

tions, motivated by SU(3)$_{\text{flavour}}$ symmetry. In the $B_s \to X\ell\nu$ analysis, the branching fractions set in the MC generation are kept unchanged. In the $B_s \to D_s^{(*)}X\ell\nu$ analysis, the branching fraction predictions from Ref. [29] are chosen as nominal values, because this publication predicts the branching fraction for the D_s, D_s^* and D_s^{**} decay channels and therefore provides a self-consistent picture of the full semileptonic B_s width. The branching fractions are rescaled by applying weights

$$w_{\mathcal{B}} = \mathcal{B}_{\text{new}}/\mathcal{B}_{\text{orig}}\,, \tag{A.1}$$

where $\mathcal{B}_{\text{new}}$ and $\mathcal{B}_{\text{orig}}$ are the new branching fraction and the original one used in the simulation, respectively. Table A.1 lists the calculated weighting factors.

A.2 Correction of the kinematic distributions

In addition to the branching fractions rescaling, also the modelling of the kinematic distributions of the decays is adjusted. The models and the variables used to re-weight semileptonic B_s decays are summarised in Table A.2. Since the form factor shapes of semileptonic B_s decays have not yet been measured, the ISGW2 quark model (cf. Sec. 2.4.3) was chosen as generator for semileptonic B_s decays in the Belle MC

Mode	Original	$B_s \to D_s^{(*)} X \ell \nu$ analysis	$B_s \to X \ell \nu$ analysis
$B_s \to D_s \ell \nu$	Belle ISGW2	CLN $[q^2, \tilde{p}_\ell]$	CLN $[q^2, \tilde{p}_\ell]$
$B_s \to D_s^* \ell \nu$	Belle ISGW2	CLN $[q^2, \tilde{p}_\ell]$	CLN $[q^2, \tilde{p}_\ell]$
$B_s \to D_s^{**} \ell \nu$	Belle ISGW2	LLSW $[w, \cos\theta_\ell]$	Belle II ISGW2 $[q^2, \tilde{p}_\ell]$

Table A.2: Models for semileptonic decays in the original MC sample and the models used for the re-weighting. The distributions for which the re-weighting is performed are given in square brackets.

sample. Motivated by the considerations in Sec. 2.4.2 and Sec. 2.4.3, the ISGW2 model is replaced for the analyses described in this thesis by the CLN model with the parameters measured in B decays (see Eqs. 2.59 and 2.62). The adjustment of the CLN parameters should involve all variables describing the differential decay width (cf. Sec. 2.4), i.e. the momentum transfer, q^2, is sufficient for $B_s \to D_s \ell \nu$ decays, while $B_s \to D_s^* \ell \nu$ decays require a four-dimensional re-weighting of the q^2, $\cos\theta_\ell$, $\cos\theta_V$, χ distributions. Until now, the default procedure at Belle was to correct solely the q^2 distribution leaving the other distributions uncorrected.

In order to re-weight the generated kinematic distributions of B_s decays from the ISGW2 to the CLN model, 1 million events of semileptonic B_s decays are generated with the EvtGen event generator [89] for both models. Figures A.1 and A.2 show the kinematic distributions of the $B_s \to D_s \ell \nu$ and $B_s \to D_s^* \ell \nu$ decay modes simulated with the Belle ISGW2 generator module and compare them to the predictions of the CLN model. Additionally, the predictions of the Belle II ISGW2 generator are shown. A pronounced disagreement is observed between the Belle ISGW2 generator and the other generators, which manifests itself most prominently in the uniform $\cos\theta_\ell$ distribution. An investigation of the source code of the generator module revealed that this discrepancy is due to missing definitions for B_s decays in the Belle version of the ISGW2 module.

Because of the malfunctioning Belle ISGW2 generator module for $B_s \to D_s \ell \nu$ decays, the correction of a second kinematic distribution is necessary in addition to the q^2 distribution. The lepton momentum in the rest frame of the B_s meson, $\tilde{p}_\ell$, is chosen as second distribution instead of the angle $\cos\theta_\ell$, because the lepton momentum is used for signal extraction in the analyses. The weight for an event in a bin $(q^2, \tilde{p}_\ell)$ is derived using the samples of simulated events by calculating the ratio of the new (correct) predicted yield to the original (wrong) yield in the bin $(q^2, \tilde{p}_\ell)$:

$$\text{weight}(q^2, \tilde{p}_\ell) = \frac{N_\text{new}(q^2, \tilde{p}_\ell)}{N_\text{orig}(q^2, \tilde{p}_\ell)} \,. \tag{A.2}$$

As a test of the re-weighting procedure, the weights are applied to an independent sample of events generated with the Belle ISGW2 module.

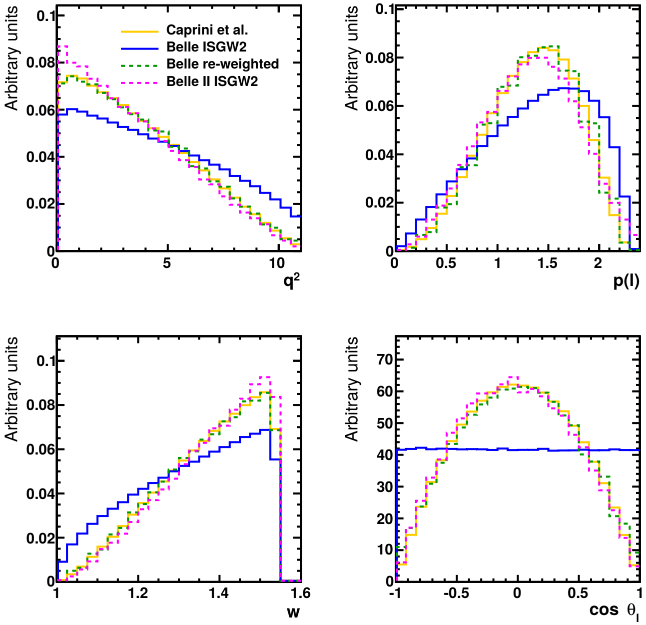

Figure A.1: Generated kinematic distributions of $B_s \to D_s \ell \nu$ decays. The "Caprini et al." (CLN) [28] distributions are generated with the HQET2 EvtGen module using the parameter from Eq. 2.59. The "Belle ISGW2" distributions are generated with the nominal Belle EvtGen ISGW2 module. These distributions are also shown after performing the re-weighting to demonstrate the agreement with the CLN distribution. Furthermore, distributions generated with the EvtGen ISGW2 module from the Belle II simulation are shown.

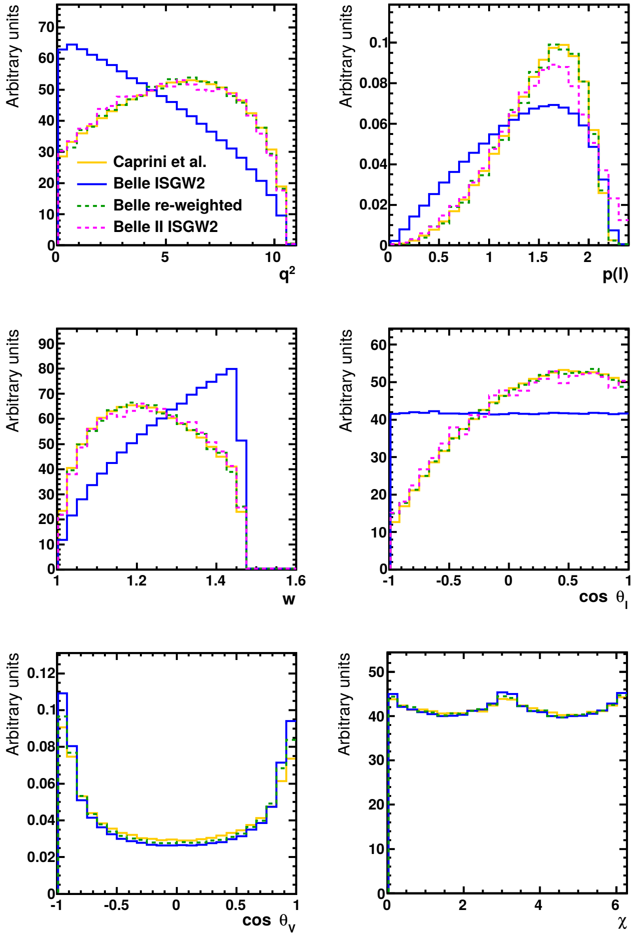

Figure A.2: Generated kinematic distributions of $B_s \to D_s^* \ell \nu$ decays. The "Caprini et al." (CLN) [28] distributions are generated with the HQET2 EvtGen module using the parameter from Eq. 2.62. The "Belle ISGW2" distributions are generated with the nominal Belle EvtGen ISGW2 module. These distributions are also shown after performing the re-weighting to demonstrate the agreement with the CLN distribution. Furthermore, distributions generated with the EvtGen ISGW2 module from the Belle II simulation are shown.

The re-weighted distributions are in good agreement with the CLN distributions as can be seen in Fig. A.1. It also shows that the correction of the $\tilde{p}_\ell$ distribution effectively corrects the $\cos\theta_\ell$ distribution. In the case, of $B_s \to D_s^* \ell \nu$ decays, an analogous two-dimensional re-weighting is performed in bins of $(q^2, \tilde{p}_\ell)$. The $\cos\theta_V$ and χ distributions show sufficient agreement between the ISGW2 and the CLN generator modules (see Fig. A.2) and do not have to be corrected.

The $B_s \to D_s^{**} \ell \nu$ events generated with the malfunctioning Belle ISGW2 module are re-weighted in the $B_s \to D_s^{(*)} X \ell \nu$ analysis to the LLSW model. Since there is no EvtGen module available for the LLSW model, the formula for the differential decay width is implemented in a C++ function and the event yields are determined by numerical integration. The differential decay width is expressed in the variables w and $\cos\theta_\ell$, and therefore these variables are used instead of q^2 and $\tilde{p}_\ell$ to define the bins for the re-weighting. The LLSW model originally developed for $B \to D^{**} \ell \nu$ decays is adapted by replacing the B and D^{**} masses by the corresponding B_s and D_s^{**} masses. The model parameters are chosen to be $\eta_{\mathrm{ke}} = 0$ and $\mathrm{d}\hat{\tau}/\mathrm{d}w = -1.5$. The weights are calculated for the two model options B1 and B2 and the average between the two is used for the analysis. Details on the different model options can be found in Ref. [38]. In the $B_s \to X \ell \nu$ analysis, the Belle II ISGW2 generator is used as reference to calculate the weights for $B_s \to D_s^{**} \ell \nu$ decays.

A.3 Validation of the re-weighting procedure for semileptonic decays with B decays

To validate the two-dimensional re-weighting procedure for semileptonic B_s decays, the re-weighting is tested on exclusive $B^0 \to D^* \ell \nu$ decays. For this decay mode, the weights do not describe the transition from the ISGW2 to the CLN model, but an update of the model parameters:

$$\rho: \quad 1.3 \to 1.207\,, \tag{A.3}$$

$$R_1: \quad 1.18 \to 1.403\,, \tag{A.4}$$

$$R_2: \quad 0.71 \to 0.854\,. \tag{A.5}$$

(a) $B_s \to D^*_{s0}\ell\nu$

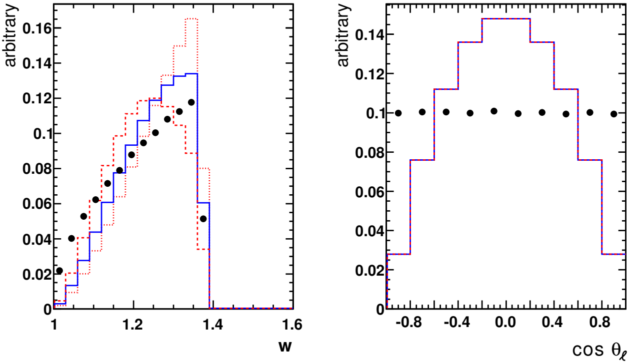

(b) $B_s \to D'_{s1}\ell\nu$

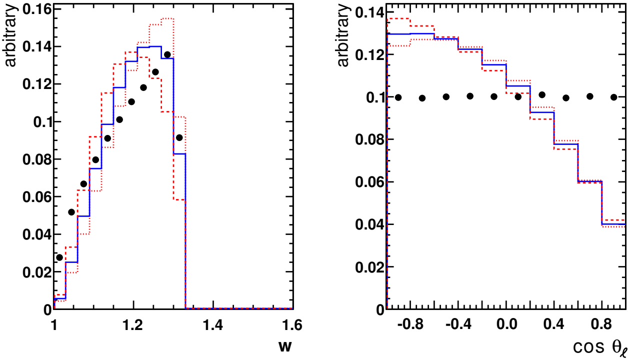

Figure A.3: Kinematic distributions of (a) $B_s \to D^*_{s0}\ell\nu$ decays and (b) $B_s \to D'_{s1}\ell\nu$ decays generated with the Belle ISGW2 module (black points) and the prediction obtained with the LLSW model (blue line). The red lines represent the maximum deviation from the prediction under a variation of the LLSW model parameters (option B1 vs. B2, η_{ke}, and $\mathrm{d}\hat{\tau}/\mathrm{d}w$).

(a) $B_s \to D_{s1}\ell\nu$

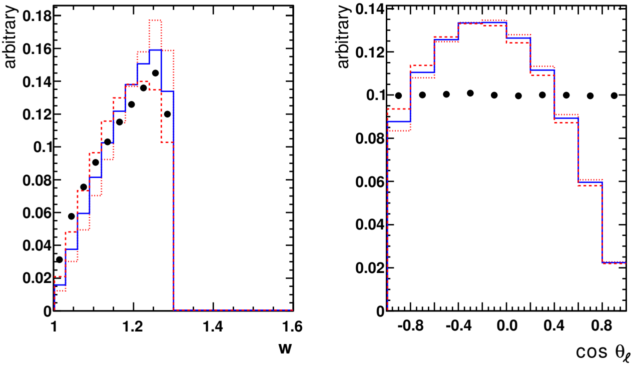

(b) $B_s \to D^*_{s2}\ell\nu$

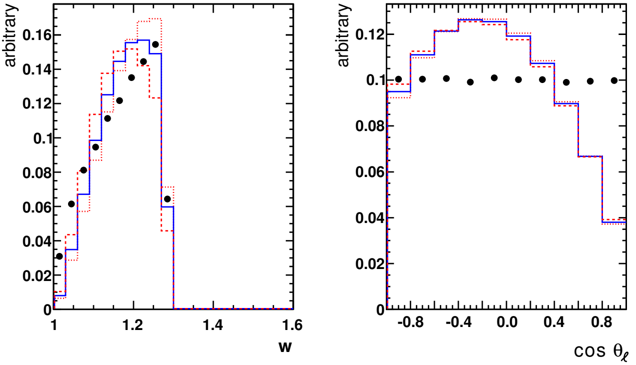

Figure A.4: Kinematic distributions of (a) $B_s \to D_{s1}\ell\nu$ decays and (b) $B_s \to D^*_{s2}\ell\nu$ decays generated with the Belle ISGW2 module (black points) and the prediction obtained with the LLSW model (blue line). The red lines represent the maximum deviation from the prediction under a variation of the LLSW model parameters (option B1 vs. B2, η_{ke}, and $\mathrm{d}\hat{\tau}/\mathrm{d}w$).

Mode	PDG / Estimate [%]
$D^-\ell\nu$	2.18 ± 0.12
$D^{*-}\ell\nu$	4.93 ± 0.11
$D_1\ell\nu$	0.74 ± 0.11
$D_2\ell\nu$	0.47 ± 0.17
$D_1'\ell\nu$	0.26 ± 0.09
$D_0^*\ell\nu$	0.52 ± 0.22

Table A.3: Branching fractions of semileptonic B^0 decays. The estimates for the $D^{**}\ell\nu$ modes are based on the predictions of the LLSW model [38].

The event weights are derived from two simulated samples based on the old and the new parameter sets (cf. Eq.A.2).

The $B^0 \to D^{*-}\ell^+\nu$ decays are reconstructed in a sample of 540 fb^{-1} of $\Upsilon(4S)$ data (experiments 33-71, SVD2). A MC sample of the same size is generated using EvtGen and the Belle detector simulation. Additionally, a 63.4 fb^{-1} sample of off-resonance data is used to study the continuum background. The simulated events are corrected with the procedures described in Sec. 5 to reflect the lepton efficiencies, the misidentification rates from hadrons passing the lepton selection criteria, and the kaon and pion efficiencies of the real detector. The semileptonic branching fractions of B^0 decays in the simulation are listed in Table A.3. The selection criteria for kaons, pions and leptons are analogous to the ones described in Chapter 5. The minimum centre-of-mass frame momentum of the reconstructed signal lepton candidate is set to 1.4 GeV to suppress the background from secondary leptons and misidentified hadrons. The D^{*-} mesons are reconstructed in the decay channel $D^{*-} \to \bar{D}^0\pi^-_{\text{slow}}; \bar{D}^0 \to K^+\pi^-$. The same selection criteria are also applied to the slow pions, π^-_{slow}. The following mass windows are applied to D^{*-} candidates: $|m_{K\pi} - M_{D^0}| < 13.75\,\text{MeV}$ and $144\,\text{MeV} < |m_{K\pi\pi_{\text{slow}}} - m_{K\pi}| < 147\,\text{MeV}$. To suppress background from $c\bar{c}$ continuum, the second normalised Fox-Wolfram momentum [102], R_2, is required to be below 0.4, and for the thrust angle (cf. Sec. 5.4) the criterion $|\cos\theta_{\text{thrust}}| < 0.8$ is

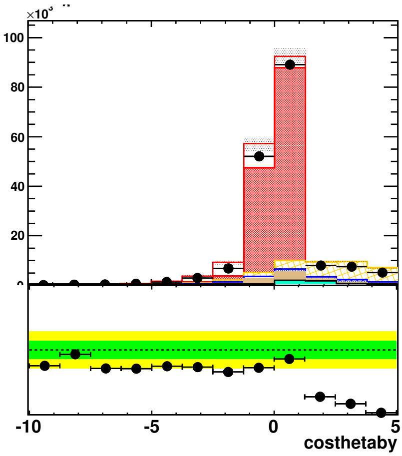

Figure A.5: Distribution of $\cos(\theta_{BD^*\ell})$ for reconstructed $D^{*-}\ell^+$ events from $\Upsilon(4S)$ data (black points). The superimposed MC histograms are from bottom to top: continuum background (light blue), misreconstructed D^{*-} candidates (brown), secondary leptons and misidentified hadrons (hatched blue), D^{*+}-electron combinations from different B^0 decays (hatched orange), $B^0 \to D^{*-}\ell^+\nu$ decays (hatched red), $B^0 \to D^{**}\ell^+\nu$ decays (white). The MC uncertainty is represented by the shaded error band.

applied. A sample which is very pure in signal decays can be obtained using the variable

$$\cos(\theta_{BD^*\ell}) = \frac{2E^*_{\text{beam}}E^*_{D^*\ell} - m_B^2 - m_{D^*\ell}^2}{2|\vec{p}^{\,*}_B||\vec{p}^{\,*}_{D^*\ell}|}\,, \qquad \text{(A.6)}$$

which is similar to the variable X_{mis} defined in Eq. 6.4 and takes for correctly reconstructed signal decays values between -1 and 1. Figure A.5 (b) shows that the data-MC agreement of this variable is not good, but since the signal is concentrated in the region $|\cos(\theta_{BD^*\ell})| < 1$ with only small backgrounds, the criterion $|\cos(\theta_{BD^*\ell})| < 1.2$ is applied for the data-MC comparison.

The w and p^*_ℓ spectra of the reconstructed $B^0 \to D^*\ell\nu$ decays are compared to the re-weighetd MC distributions. Fig. A.6 shows the effect of a re-weighting in bins of q^2 alone and in bins of $(q^2, \tilde{p}_\ell)$. It can be seen that the correction in q^2 alone is insufficient to obtain the correct lepton momentum spectrum, while the agreement using the two-dimensional re-weighting in bins of $(q^2, \tilde{p}_\ell)$ is excellent.

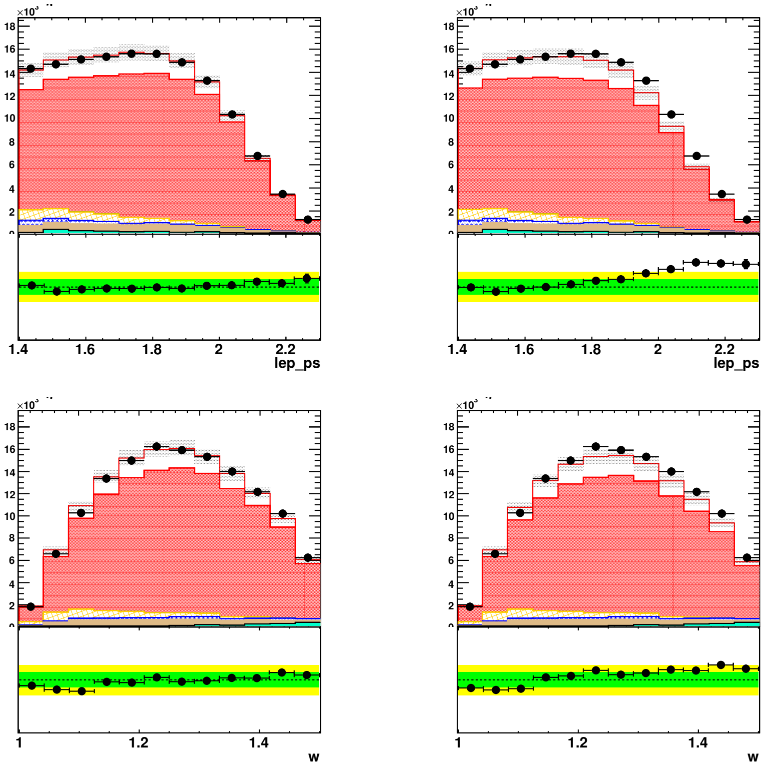

(a) $q^2, \tilde{p}_\ell$ weights

(b) q^2 weights

Figure A.6: Data-MC agreement of the w, and lepton momentum distributions of $B^0 \to D^{*-}\ell^+\nu$ decays reconstructed in a 540 fb^{-1} $\Upsilon(4S)$ sample. The variable w is approximated by $E^*_{D^*}/m_{D^*}$, because the B mesons are produced almost at rest in the $\Upsilon(4S)$ centre-of-mass frame. The black points represent the data and the stacked histograms the MC samples with the following contributions: continuum background (light blue), misreconstructed D^{*-} candidates (brown), secondary leptons and misidentified hadrons (hatched blue), D^{*+}-electron combinations from different B^0 decays (hatched orange), $B^0 \to D^{*-}\ell^+\nu$ decays (hatched red), $B^0 \to D^{**}\ell^+\nu$ decays (white). The MC uncertainty is represented by the shaded error band. The MC distributions are corrected with different re-weighting procedures: (a) the two-dimensional weights in bins of $q^2 \times p^*(\ell)$ and (b) with the conventional one-dimensional weights in bins of q^2 only.

APPENDIX B

Supporting Tables and Figures

(a) $D_s^- e^+$ sample

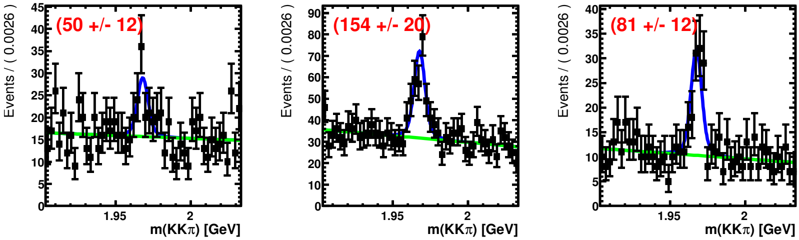

(b) $D_s^- \mu^+$ sample

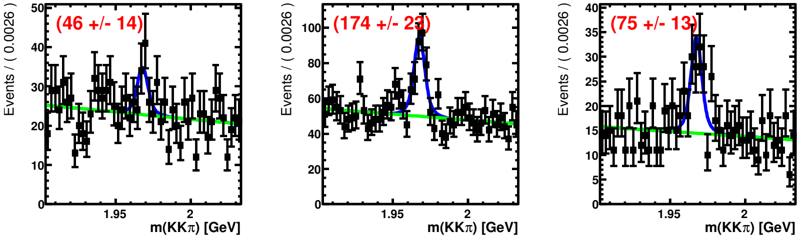

Figure B.1: Fits to the $m_{KK\pi}$ distributions from off-resonance data.

(a) Electron mode

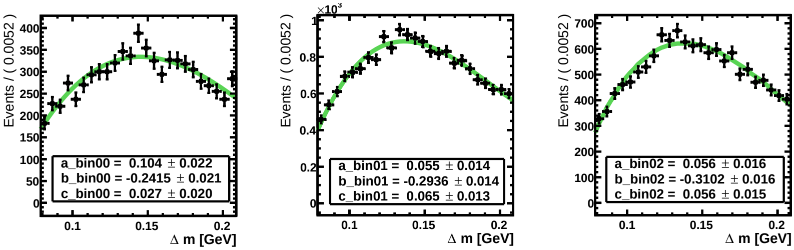

(b) Muon mode

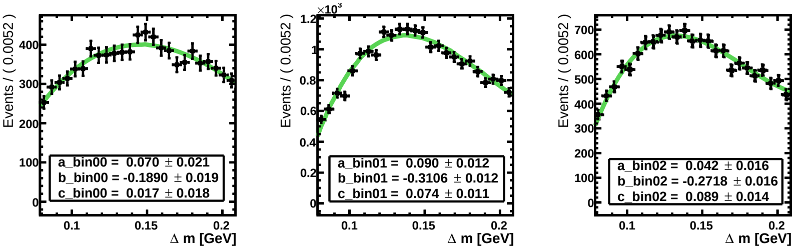

Figure B.2: Fits to the Δm distributions of mis-reconstructed D_s^* candidates in the MC simulation in the three counting regions. The black points represent the simulated decays and the green curve is the fitted third order Chebychev polynomial.

(a) $D_s^{*-} e^+$ sample

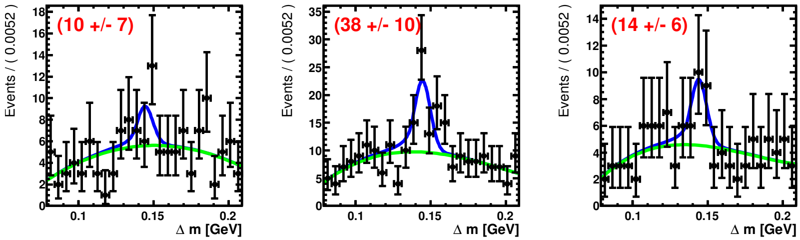

(b) $D_s^{*-} \mu^+$ sample

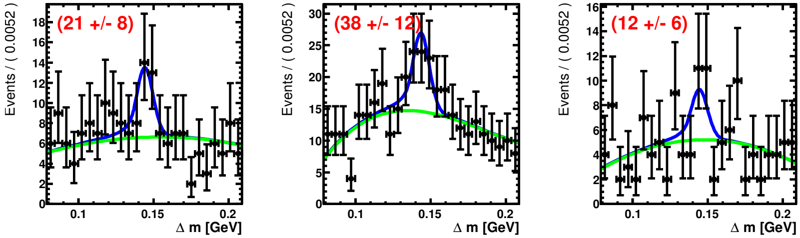

Figure B.3: Fits to the Δm distributions from off-resonance data.

Parameter	Electrons	Muons
μ / GeV, region A	1.9681 ± 0.0001	1.9680 ± 0.0001
μ / GeV, region B	1.9678 ± 0.0001	1.9678 ± 0.0001
μ / GeV, region C	1.9676 ± 0.0001	1.9676 ± 0.0001
σ_1 / GeV	0.0034 ± 0.0001	0.0033 ± 0.0001
r_σ	2.4 ± 0.3	2.2 ± 0.1
r_N	0.22 ± 0.05	0.34 ± 0.06
b, region A	-0.05 ± 0.03	-0.09 ± 0.03
b, region B	-0.17 ± 0.02	-0.15 ± 0.02
b, region C	-0.21 ± 0.02	-0.19 ± 0.02

Table B.1: Fit results of the D_s mass fits.

Parameter	Electrons	Muons
μ / GeV, region A	0.1442 ± 0.0005	0.1441 ± 0.0005
μ / GeV, region B	0.1445 ± 0.0004	0.1435 ± 0.0004
μ / GeV, region C	0.1440 ± 0.0004	0.1443 ± 0.0004
σ_1 / GeV	0.0052 ± 0.0002	0.0054 ± 0.0002
α	1.35 ± 0.03	1.34 ± 0.03
n	1.89 ± 0.11	1.92 ± 0.10
r_σ	4.1 ± 0.2	4.2 ± 0.2
r_N	0.930 ± 0.007	0.927 ± 0.007
a, region A	0.14 ± 0.06	0.06 ± 0.05
a, region B	0.05 ± 0.04	0.04 ± 0.04
a, region C	0.07 ± 0.04	0.06 ± 0.04
b, region A	-0.30 ± 0.06	-0.10 ± 0.06
b, region B	-0.32 ± 0.04	-0.27 ± 0.04
b, region C	-0.27 ± 0.04	-0.26 ± 0.04
c, region A	0.00 ± 0.14	0.00 ± 0.06
c, region B	0.06 ± 0.03	0.07 ± 0.03
c, region C	0.08 ± 0.04	0.00 ± 0.06

Table B.2: Fit results of the Δm fits.

(a) $D_s^- e^+$ sample

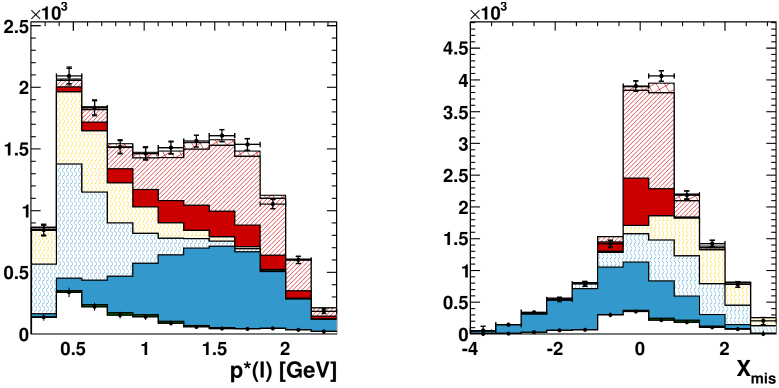

(b) $D_s^- \mu^+$ sample

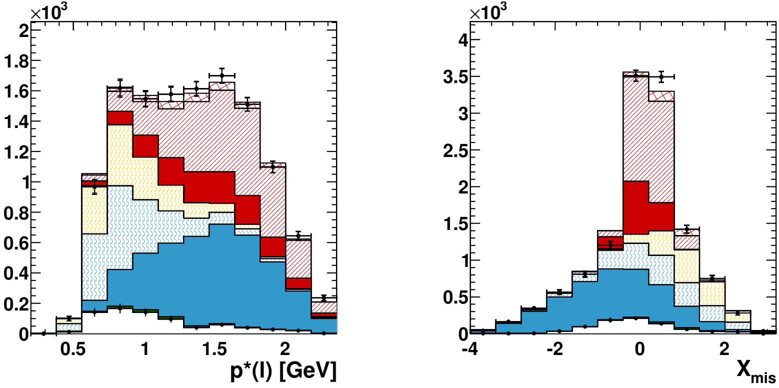

Figure B.4: $D_s^- \ell^+$ events reconstructed in $\Upsilon(5S)$ data (low lepton momentum threshold). Look back plots of the p_a^* nd the X_{mis} distributions. The scale factors obtained in the measurement are applied to the MC components.

(b) $D_s^{*-}e^+$ sample

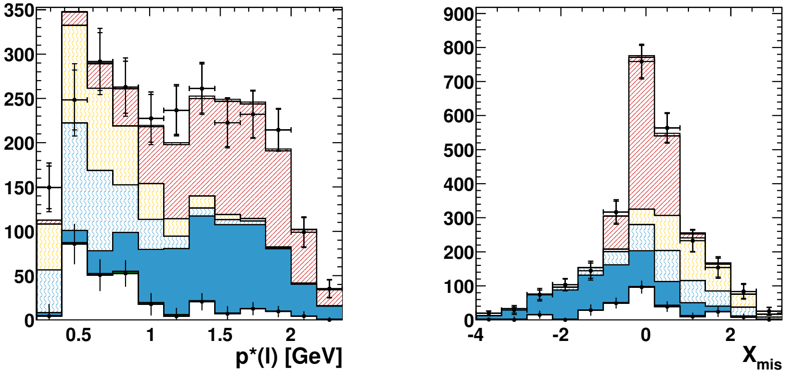

(b) $D_s^{*-}\mu^+$ sample

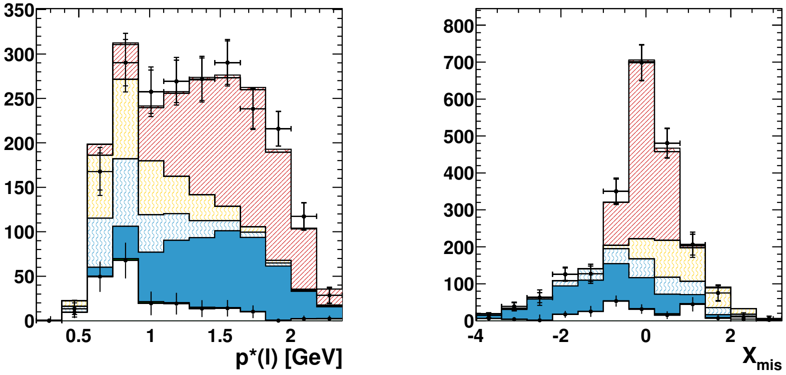

Figure B.5: $D_s^{*-}\ell^+$ events reconstructed in $\Upsilon(5S)$ data (low lepton momentum threshold). Look back plots of the p_a^* nd the X_{mis} distributions. The scale factors obtained in the measurement are applied to the MC components.

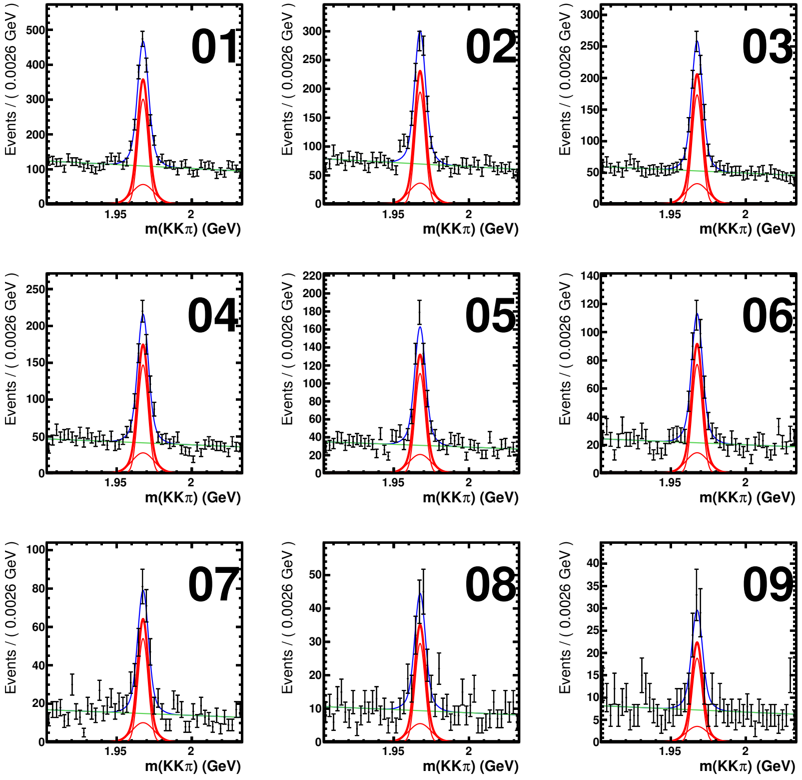

Figure B.6: Fits to the $K^+K^-\pi^+$ mass distributions of $D_s^+e^+$ events reconstructed in $\Upsilon(5S)$ data in 9 bins of electron momentum, p_e. The black points with error bars are the data. The blue line is the fit result. The green line is the fitted background function, the thick red line the fitted signal function, which is the sum of two Gaussian functions (thin red lines).

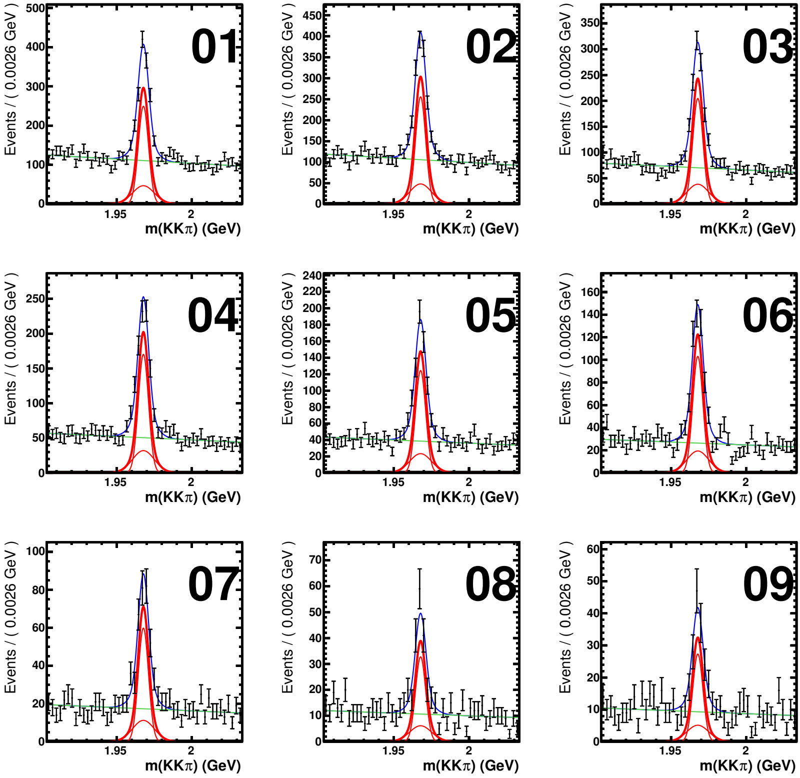

Figure B.7: Fits to the $K^+K^-\pi^+$ mass distributions of $D_s^+\mu^+$ events reconstructed in $\Upsilon(5S)$ data in 9 bins of electron momentum, p_μ. The black points with error bars are the data. The blue line is the fit result. The green line is the fitted background function, the thick red line the fitted signal function, which is the sum of two Gaussian functions (thin red lines).

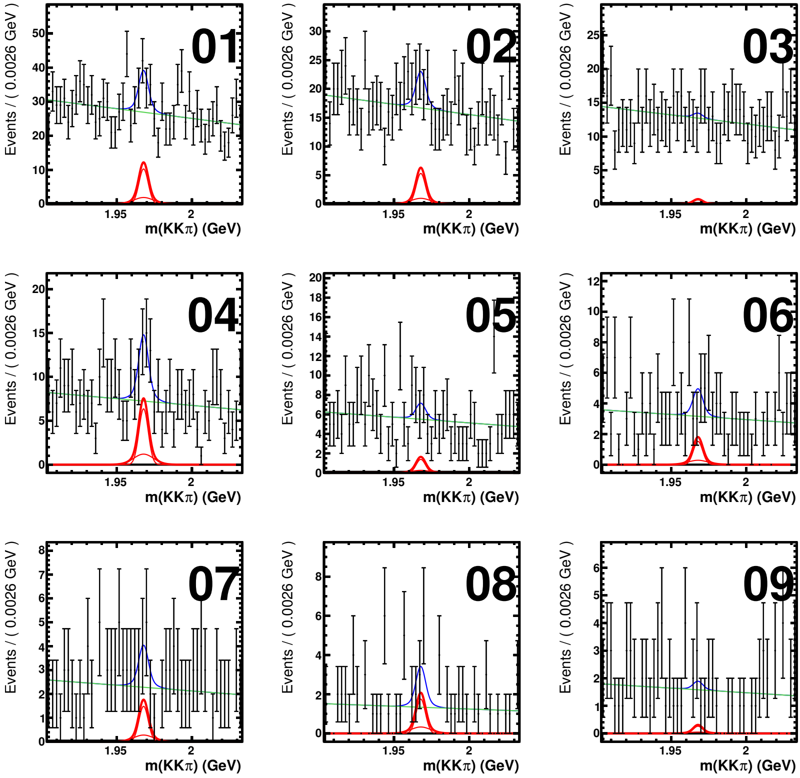

Figure B.8: Fits to the $K^+K^-\pi^+$ mass distributions of $D_s^+e^+$ events reconstructed in off-resonance data in 9 bins of electron momentum, p_e. The black points with error bars are the data. The blue line is the fit result. The green line is the fitted background function, the thick red line the fitted signal function, which is the sum of two Gaussian functions (thin red lines).

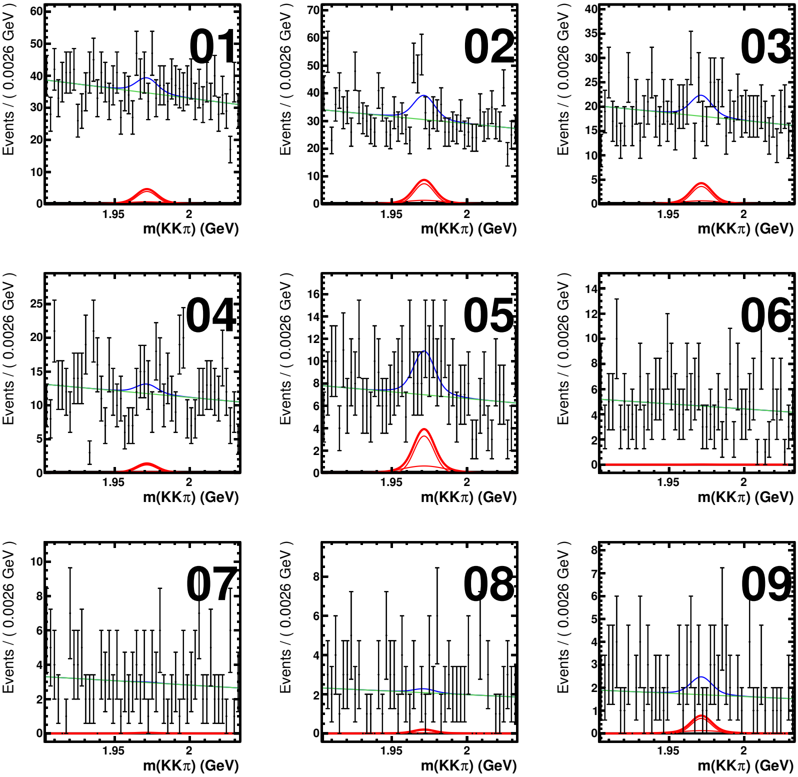

Figure B.9: Fits to the $K^+K^-\pi^+$ mass distributions of $D_s^+\mu^+$ events reconstructed in off-resonance data in 9 bins of electron momentum, p_μ. The black points with error bars are the data. The blue line is the fit result. The green line is the fitted background function, the thick red line the fitted signal function, which is the sum of two Gaussian functions (thin red lines).

Bibliography

[1] C. Oswald, "Tests of DEPFET pixel detectors and Simulation of the Belle II vertex detector", Diploma thesis, 2011.

[2] J. Dingfelder and T. Mannel,
"Leptonic and Semileptonic Decays of B mesons",
Unpublished manuscript (2014).

[3] C. Yanagisawa et al., "B semileptonic decays at the Upsilon (4S) and the Upsilon (5S)", *Phys.Rev.Lett.* 66 (1991) 2436–2439,
DOI: `10.1103/PhysRevLett.66.2436`.

[4] K. Abe et al., "Measurement of the inclusive $B_s^0 \to X^+\ell^-\nu$ semileptonic decay branching fraction" (2007),
arXiv: `0710.2548 [hep-ex]`.

[5] J. Lees et al., "A Measurement of the Semileptonic Branching Fraction of the B_s Meson", *Phys.Rev.* D85 (2012) 011101,
DOI: `10.1103/PhysRevD.85.011101`,
arXiv: `1110.5600 [hep-ex]`.

[6] V. Abazov et al.,
"Measurement of the B_s^0 semileptonic branching ratio to an orbitally excited D_s state, $\mathcal{B}(B_s^0 \to D_{s1}^-(2536)\mu^+\nu X)$",
Phys.Rev.Lett. 102 (2009) 051801,
DOI: `10.1103/PhysRevLett.102.051801`,
arXiv: `0712.3789 [hep-ex]`.

[7] R. Aaij et al., "First observation of $\bar{B}_s^0 \to D_{s2}^{*+} X \mu^- \bar{\nu}$ decays", *Phys.Lett.* B698 (2011) 14–20,
DOI: `10.1016/j.physletb.2011.02.039`,
arXiv: `1102.0348 [hep-ex]`.

[8] J. Beringer et al., "The Review of Particle Physics", *Phys. Rev.* D86 (2012), and 2013 partial update for the 2014 edition 010001.

[9] S. Chatrchyan et al., "Study of the Mass and Spin-Parity of the Higgs Boson Candidate Via Its Decays to Z Boson Pairs", *Phys.Rev.Lett.* 110 (2013) 081803,
DOI: `10.1103/PhysRevLett.110.081803`,
arXiv: `1212.6639 [hep-ex]`.

[10] G. Aad et al.,
"Observation of a new particle in the search for the Standard Model Higgs boson with the ATLAS detector at the LHC", *Phys.Lett.* B716 (2012) 1–29,
DOI: `10.1016/j.physletb.2012.08.020`,
arXiv: `1207.7214 [hep-ex]`.

[11] C. Wu et al.,
"Experimental Test of Parity Conservation in Beta Decay", *Phys.Rev.* 105 (1957) 1413–1414,
DOI: `10.1103/PhysRev.105.1413`.

[12] M. Ciuchini et al.,
"2000 CKM triangle analysis: A Critical review with updated experimental inputs and theoretical parameters",
JHEP 0107 (2001) 013,
DOI: `10.1088/1126-6708/2001/07/013`,
arXiv: `hep-ph/0012308 [hep-ph]`.

[13] A. Hocker et al.,
"A New approach to a global fit of the CKM matrix",
Eur.Phys.J. C21 (2001) 225–259,
DOI: `10.1007/s100520100729`,
arXiv: `hep-ph/0104062 [hep-ph]`.

[14] R. Louvot, O. Schneider and T. Aushev, "Prospects for precise measurements of B_s^0 branching fractions",
Belle Note 1140 (internal report).

[15] H. Georgi, “Heavy quark effective field theory”, *Perspectives in the standard model*, ed. by R. K. Ellis, C. T. Hill and J. D.Lykken, 1991.

[16] A. V. Manohar and M. B. Wise, *Heavy Quark Physics*, ed. by T. Ericson and P. V. Landshoff, vol. 10, Cambridge University Press, 2000.

[17] W. Dungel, “Precision measurements of the CKM-matrix elements $|V_{cb}|$ and the form factors of semileptonic decays of B mesons”, PhD thesis, 2009.

[18] K. G. Wilson, “Confinement of Quarks”, *Phys.Rev.* D10 (1974) 2445–2459, DOI: `10.1103/PhysRevD.10.2445`.

[19] M. Atoui et al., “$B_s \to D_s \ell \nu_\ell$ near zero recoil in and beyond the Standard Model”, *Eur.Phys.J.* C74 (2014) 2861, DOI: `10.1140/epjc/s10052-014-2861-z`, arXiv: `1310.5238 [hep-lat]`.

[20] J. A. Bailey et al., “$B_s \to D_s/B \to D$ Semileptonic Form-Factor Ratios and Their Application to BR($B_s^0 \to \mu^+\mu^-$)”, *Phys.Rev.* D85 (2012) 114502, DOI: `10.1103/PhysRevD.85.114502,10.1103/PhysRevD.86.039904`, arXiv: `1202.6346 [hep-lat]`.

[21] Y.-Y. Fan, W.-F. Wang and Z.-J. Xiao, “Study of $\bar{B}_s^0 \to (D_s^+, D_s^{*+}) l^- \bar{\nu}_l$ decays in the pQCD factorization approach”, *Phys.Rev.* D89 (2014) 014030, DOI: `10.1103/PhysRevD.89.014030`, arXiv: `1311.4965 [hep-ph]`.

[22] X. Chen et al., “Estimating Form Factors of $B_s \to D_s^{(*)}$ and their Applications to Semi-leptonic and Non-leptonic Decays”, *J.Phys.* G39 (2012) 045002, DOI: `10.1088/0954-3899/39/4/045002`, arXiv: `1106.3003 [hep-ph]`.

[23] Y.-Y. Fan et al., “Semileptonic decays $B \to D^{(*)} l\nu$ in the perturbative QCD factorization approach”, *Chin.Sci.Bull.* 59 (2014) 125–132, DOI: `10.1007/s11434-013-0049-9`, arXiv: `1301.6246 [hep-ph]`.

[24] R.-H. Li, C.-D. Lu and Y.-M. Wang, “Exclusive B_s decays to the charmed mesons $D_s^+(1968, 2317)$ in the standard model”, *Phys.Rev.* D80 (2009) 014005, DOI: `10.1103/PhysRevD.80.014005`, arXiv: `0905.3259 [hep-ph]`.

[25] K. Azizi, “QCD Sum Rules Study of the Semileptonic $B_s(B^\pm)(B^0) \to D_s[1968](D^0)(D^\pm)\ell\nu$ Decays”, *Nucl.Phys.* B801 (2008) 70–80, DOI: `10.1016/j.nuclphysb.2008.04.011`, arXiv: `0805.2802 [hep-ph]`.

[26] K. Azizi and M. Bayar, “Semileptonic $B_{(q)} \to D^*_{(q)}\ell\nu$ $(q = s, d, u)$ Decays in QCD Sum Rules”, *Phys.Rev.* D78 (2008) 054011, DOI: `10.1103/PhysRevD.78.054011`, arXiv: `0806.0578 [hep-ph]`.

[27] P. Blasi et al., “Phenomenology of B_s decays”, *Phys.Rev.* D49 (1994) 238–246, DOI: `10.1103/PhysRevD.49.238`, arXiv: `hep-ph/9307290 [hep-ph]`.

[28] I. Caprini, L. Lellouch and M. Neubert, “Dispersive bounds on the shape of $\bar{B} \to D^{(*)}\ell\bar{\nu}$ form-factors”, *Nucl.Phys.* B530 (1998) 153–181, DOI: `10.1016/S0550-3213(98)00350-2`, arXiv: `hep-ph/9712417 [hep-ph]`.

[29] R. Faustov and V. Galkin, “Weak decays of B_s mesons to D_s mesons in the relativistic quark model”, *Phys.Rev.* D87 (2013) 034033, DOI: `10.1103/PhysRevD.87.034033`, arXiv: `1212.3167`.

[30] C. Albertus, "Weak decays of $\bar{B}_s$ mesons", *Phys.Rev.* D89 (2014) 065042, DOI: `10.1103/PhysRevD.89.065042`, arXiv: `1401.1791 [hep-ph]`.

[31] J. Segovia et al., "Semileptonic B and B_s decays into orbitally excited charmed mesons", *Phys.Rev.* D84 (2011) 094029, DOI: `10.1103/PhysRevD.84.094029`, arXiv: `1107.4248 [hep-ph]`.

[32] S.-M. Zhao, X. Liu and S.-J. Li, "Study on $B_{(s)} \to D_{sJ}(2317, 2460)\ell\bar{\nu}$ Semileptonic Decays in the CQM Model", *Eur.Phys.J.* C51 (2007) 601–606, DOI: `10.1140/epjc/s10052-007-0322-7`, arXiv: `hep-ph/0612008 [hep-ph]`.

[33] J.-M. Zhang and G.-L. Wang, "B_s Semileptonic Decays to D_s and D_s^* in Bethe-Salpeter Method", *Chin.Phys.Lett.* 27 (2010) 051301, DOI: `10.1088/0256-307X/27/5/051301`, arXiv: `1003.5576 [hep-ph]`.

[34] G. Li, F.-l. Shao and W. Wang, "$B_s \to D_s(3040)$ form factors and B_s decays into $D_s(3040)$", *Phys.Rev.* D82 (2010) 094031, DOI: `10.1103/PhysRevD.82.094031`, arXiv: `1008.3696 [hep-ph]`.

[35] N. Isgur et al., "Semileptonic B and D Decays in the Quark Model", *Phys.Rev.* D39 (1989) 799–818, DOI: `10.1103/PhysRevD.39.799`.

[36] D. Scora and N. Isgur, "Semileptonic meson decays in the quark model: An update", *Phys.Rev.* D52 (1995) 2783–2812, DOI: `10.1103/PhysRevD.52.2783`, arXiv: `hep-ph/9503486 [hep-ph]`.

[37] M.-Q. Huang, “Exclusive semileptonic B(s) decays to excited D(s) mesons: Search of D(sJ)(2317) and D(sJ)(2460)”, *Phys.Rev.* D69 (2004) 114015, DOI: `10.1103/PhysRevD.69.114015`, arXiv: `hep-ph/0404032 [hep-ph]`.

[38] A. K. Leibovich et al., “Semileptonic B decays to excited charmed mesons”, *Phys.Rev.* D57 (1998) 308–330, DOI: `10.1103/PhysRevD.57.308`, arXiv: `hep-ph/9705467 [hep-ph]`.

[39] Y. Amhis et al., “Averages of B-Hadron, C-Hadron, and tau-lepton properties as of early 2012” (2012), arXiv: `1207.1158 [hep-ex]`.

[40] W. Dungel et al., “Measurement of the form factors of the decay $B0 \to D^{*-}\ell^{+}\nu$ and determination of the CKM matrix element $|V_{cb}|$”, *Phys.Rev.* D82 (2010) 112007, DOI: `10.1103/PhysRevD.82.112007`, arXiv: `1010.5620 [hep-ex]`.

[41] D. Benson et al., “Imprecated, yet impeccable: On the theoretical evaluation of $\Gamma(B \to X_c \ell \nu)$”, *Nucl.Phys.* B665 (2003) 367–401, DOI: `10.1016/S0550-3213(03)00452-8`, arXiv: `hep-ph/0302262 [hep-ph]`.

[42] I. Bigi, T. Mannel and N. Uraltsev, “Semileptonic width ratios among beauty hadrons”, *JHEP* 1109 (2011) 012, DOI: `10.1007/JHEP09(2011)012`, arXiv: `1105.4574 [hep-ph]`.

[43] M. Giorgi, ed., *CP violation: From quarks to leptons. Proceedings, International School of Physics 'Enrico Fermi', 163rd Course, Varenna, Italy,* July 2006.

[44] M. Gronau and J. L. Rosner,
"Ratios of heavy hadron semileptonic decay rates",
Phys.Rev. D83 (2011) 034025,
DOI: `10.1103/PhysRevD.83.034025`,
arXiv: `1012.5098 [hep-ph]`.

[45] T. Abe et al., "Achievements of KEKB",
PTEP 2013 (2013) 03A001, DOI: `10.1093/ptep/pts102`.

[46] S. Kurokawa, "Overview of the KEKB accelerators",
Nucl.Instrum.Meth. A499 (2003) 1–7,
DOI: `10.1016/S0168-9002(02)01771-0`.

[47] T. Abe et al., "Compensation of the Crossing Angle with Crab Cavities at KEKB", *Conf.Proc.* C070625 (2007) 27,
arXiv: `0706.3248 [physics.ins-det]`.

[48] A. Abashian et al., "The Belle detector", *Nucl.Instrum.Meth.* A479.1 (2002), Detectors for Asymmetric B-factories 117–232,
ISSN: 0168-9002, DOI: `http://dx.doi.org/10.1016/S0168-9002(01)02013-7`.

[49] K. Abe et al., "Observation of large CP violation in the neutral *B* meson system", *Phys.Rev.Lett.* 87 (2001) 091802,
DOI: `10.1103/PhysRevLett.87.091802`,
arXiv: `hep-ex/0107061 [hep-ex]`.

[50] J. Brodzicka et al.,
"Physics Achievements from the Belle Experiment",
PTEP 2012 (2012) 04D001, DOI: `10.1093/ptep/pts072`,
arXiv: `1212.5342 [hep-ex]`.

[51] H. Hirano et al., "A high resolution cylindrical drift chamber for the KEK B factory",
Nucl.Instrum.Meth. A455 (2000) 294–304,
DOI: `10.1016/S0168-9002(00)00513-1`.

[52] H. Aihara et al., "Belle SVD2 vertex detector",
Nucl.Instrum.Meth. A568 (2006) 269–273,
DOI: `10.1016/j.nima.2006.05.281`.

[53] H. Bethe, “Zur Theorie des Durchgangs schneller Korpuskularstrahlen durch Materie”, *Annalen der Physik* 397.3 (1930) 325–400, ISSN: 1521-3889, DOI: `10.1002/andp.19303970303`, URL: `http://dx.doi.org/10.1002/andp.19303970303`.

[54] F. Bloch, “Zur Bremsung rasch bewegter Teilchen beim Durchgang durch Materie”, *Annalen der Physik* 408.3 (1933) 285–320, ISSN: 1521-3889, DOI: `10.1002/andp.19334080303`, URL: `http://dx.doi.org/10.1002/andp.19334080303`.

[55] W. Leo, *Techniques for Nuclear and Particle Physics Experiments: A How to Approach*, 1987.

[56] M. Cheng and other, “A study of CP violation in B meson decays – technical design report”, tech. rep. 95-1, KEK, Apr. 1995.

[57] T. Iijima et al., “Aerogel Cherenkov counter for the BELLE detector”, *Nucl.Instrum.Meth.* A453 (2000) 321–325, DOI: `10.1016/S0168-9002(00)00652-5`.

[58] I. Frank and I. Tamm, *Compt. rend. acad. sci. U.R.S.S.* 14 (1937) 109.

[59] “KEKB breaks luminosity record”, *CERN COURIER* (June 2009).

[60] B. Casey, “HadronB”, Belle Note 390 (internal report).

[61] B. Barish et al., “Measurements of the B semileptonic branching fraction with lepton tags”, *Phys.Rev.Lett.* 76 (1996) 1570–1574, DOI: `10.1103/PhysRevLett.76.1570`.

[62] D. Besson et al., “Observation of New Structure in the e+ e- Annihilation Cross-Section Above B anti-B Threshold”, *Phys.Rev.Lett.* 54 (1985) 381, DOI: `10.1103/PhysRevLett.54.381`.

[63] D. Lovelock et al., “MASSES, WIDTHS, AND LEPTONIC WIDTHS OF THE HIGHER UPSILON RESONANCES”, *Phys.Rev.Lett.* 54 (1985) 377–380, DOI: `10.1103/PhysRevLett.54.377`.

[64] M. Artuso et al., “First evidence and measurement of $B_s^{(*)}\bar{B}_s^{(*)}$ production at the $\Upsilon(5S)$”, *Phys.Rev.Lett.* 95 (2005) 261801, DOI: `10.1103/PhysRevLett.95.261801`, arXiv: `hep-ex/0508047 [hep-ex]`.

[65] G. Bonvicini et al., “Observation of $B_s^{(*)}\bar{B}_s^{(*)}$ production at the $\Upsilon(5S)$ resonance”, *Phys.Rev.Lett.* 96 (2006) 022002, DOI: `10.1103/PhysRevLett.96.022002`, arXiv: `hep-ex/0510034 [hep-ex]`.

[66] A. Drutskoy et al., “Measurement of inclusive $D_{(s)}$, D^0 and J/ψ rates and determination of the $B_s^{(*)}\bar{B}_s^{(*)}$ production fraction in $b\bar{b}$ events at the $\Upsilon(5S)$ resonance”, *Phys.Rev.Lett.* 98 (2007) 052001, DOI: `10.1103/PhysRevLett.98.052001`, arXiv: `hep-ex/0608015 [hep-ex]`.

[67] G. Huang et al., “Measurement of $\mathcal{B}(\Upsilon(5S) \to B_s^{(*)}\bar{B}_s^{(*)})$ Using ϕ Mesons”, *Phys.Rev.* D75 (2007) 012002, DOI: `10.1103/PhysRevD.75.012002`, arXiv: `hep-ex/0610035 [hep-ex]`.

[68] J. Wicht and K. Kinoshita, “$\Upsilon(5S)$ sub-group report, N_{BsBs} with inclusive D_s, $B_s \to J/\psi f_0(980, 1370)$”, Slides shown at the Belle Analysis Meeting, Feb. 2011.

[69] B. Aubert et al., “Measurement of D_s^+ and D_s^{*+} production in B meson decays and from continuum e^+e^- annihilation at $\sqrt{s} = 10.6$ GeV”, *Phys.Rev.* D65 (2002) 091104, DOI: `10.1103/PhysRevD.65.091104`, arXiv: `hep-ex/0201041 [hep-ex]`.

[70] P. Haas et al., "Observation of the Decay $B \to$ F X", *Phys.Rev.Lett.* 56 (1986) 2781, DOI: `10.1103/PhysRevLett.56.2781`.

[71] R. Sia and S. Stone, "Model independent methods for determining $\mathcal{B}(\Upsilon(5S) \to B_s^{(*)}\bar{B}_s^{(*)})$", *Phys.Rev.* D74 (2006), Erratum-ibid. D80 039901 (2009). 031501, DOI: `10.1103/PhysRevD.74.031501,10.1103/PhysRevD.80.039901`, arXiv: `hep-ph/0604201 [hep-ph]`.

[72] R. Louvot, "Study of B_s-meson production and measurement of B_s decays into a D_s and a light meson in e^+e^- collisions at $\sqrt{s} = 10.87$ GeV ", PhD thesis: EPFL, Nov. 2011.

[73] R. Louvot, Private Communication. 2011.

[74] D. Buskulic et al., "Measurement of the B_s^0 lifetime and production rate with $D_s^- \ell^+$ combinations in Z decays", *Phys.Lett.* B361 (1995) 221–233, DOI: `10.1016/0370-2693(95)01173-N`.

[75] P. Abreu et al., "Evidence for B_s^0 meson production in Z^0 decays", *Phys.Lett.* B289 (1992) 199–210, DOI: `10.1016/0370-2693(92)91385-M`.

[76] P. Acton et al., "Evidence for the existence of the strange b flavored meson B_s^0 in Z^0 decays", *Phys.Lett.* B295 (1992) 357–370, DOI: `10.1016/0370-2693(92)91578-W`.

[77] A. Drutskoy et al., "Measurement of $\Upsilon(5S)$ decays to B^0 and B^+ mesons", *Phys.Rev.* D81 (2010) 112003, DOI: `10.1103/PhysRevD.81.112003`, arXiv: `1003.5885 [hep-ex]`.

[78] O. Aquines et al., "First measurements of the exclusive decays of the $\Upsilon(5S)$ to B meson final states and improved B_s^* mass measurement", *Phys.Rev.Lett.* 96 (2006) 152001,

DOI: `10.1103/PhysRevLett.96.152001`,
arXiv: `hep-ex/0601044 [hep-ex]`.

[79] K. Chen et al., “Observation of anomalous $\Upsilon(1S)\pi^+\pi^-$ and $\Upsilon(2S)\pi^+\pi^-$ production near the $\Upsilon(5S)$ resonance”, *Phys.Rev.Lett.* 100 (2008) 112001,
DOI: `10.1103/PhysRevLett.100.112001`,
arXiv: `0710.2577 [hep-ex]`.

[80] P. Krokovny et al., “First observation of the $Z_b^0(10610)$ in a Dalitz analysis of $\Upsilon(10860) \to \Upsilon(nS)\pi^0\pi^0$”, *Phys.Rev.* D88.5 (2013) 052016,
DOI: `10.1103/PhysRevD.88.052016`,
arXiv: `1308.2646 [hep-ex]`.

[81] I. Adachi et al., “First observation of the P-wave spin-singlet bottomonium states $h_b(1P)$ and $h_b(2P)$”, *Phys.Rev.Lett.* 108 (2012) 032001,
DOI: `10.1103/PhysRevLett.108.032001`,
arXiv: `1103.3419 [hep-ex]`.

[82] A. Bondar et al., “Observation of two charged bottomonium-like resonances in Y(5S) decays”, *Phys.Rev.Lett.* 108 (2012) 122001,
DOI: `10.1103/PhysRevLett.108.122001`,
arXiv: `1110.2251 [hep-ex]`.

[83] B. Aubert et al., “Study of hadronic transitions between Υ states and observation of $\Upsilon(4S) \to \eta\Upsilon(1S)$ decay”, *Phys.Rev.* D78 (2008) 112002,
DOI: `10.1103/PhysRevD.78.112002`,
arXiv: `0807.2014 [hep-ex]`.

[84] A. Sokolov et al., “Measurement of the branching fraction for the decay $\Upsilon(4S) \to \Upsilon(1S)\pi^+\pi^-$”, *Phys.Rev.* D79 (2009) 051103,
DOI: `10.1103/PhysRevD.79.051103`,
arXiv: `0901.1431 [hep-ex]`.

[85] A. Garmash et al., “Amplitude analysis of $e^+e^- \to \Upsilon(nS)\pi^+\pi^-$ at $\sqrt{s} = 10.865$ GeV” (2014), arXiv: `1403.0992 [hep-ex]`.

[86] I. Adachi et al., "Study of Three-Body $\Upsilon(10860)$ Decays" (2012), arXiv: `1209.6450 [hep-ex]`.

[87] D. Santel et al., "Measurements of $\sigma(e^+e^- \to \Upsilon(nS)\pi^+\pi^-)$ and $\sigma(e^+e^- \to b\bar{b})$ in the $\Upsilon(10860)$ and $\Upsilon(11020)$ resonance region", *KEK Preprint 2014-33* (2014).

[88] R. Louvot et al.,
"Measurement of the Decay $B_s^0 \to D_s^- \pi^+$ and Evidence for $B_s^0 \to D_s \pm K^\pm$ in e^+e^- Annihilation at $\sqrt{s} = 10.87$ GeV", *Phys.Rev.Lett.* 102 (2009) 021801,
DOI: `10.1103/PhysRevLett.102.021801`,
arXiv: `0809.2526 [hep-ex]`.

[89] D. Lange, "The EvtGen particle decay simulation package", *Nucl.Instrum.Meth.* A462 (2001) 152–155,
DOI: `10.1016/S0168-9002(01)00089-4`.

[90] E. Barberio and Z. Was, "PHOTOS: A Universal Monte Carlo for QED radiative corrections. Version 2.0", *Comput.Phys.Commun.* 79 (1994) 291–308,
DOI: `10.1016/0010-4655(94)90074-4`.

[91] T. Sjostrand, "High-energy physics event generation with PYTHIA 5.7 and JETSET 7.4", *Comput.Phys.Commun.* 82 (1994) 74–90,
DOI: `10.1016/0010-4655(94)90132-5`.

[92] R. Brun et al., "GEANT3 Users Guide", tech. rep. EE/84-1, CERN, 1986.

[93] C. Oswald et al.,
"Semi-inclusive studies of semileptonic B_s decays at Belle" (2015), arXiv: `1504.02004 [hep-ex]`.

[94] C. Oswald et al., "Measurement of the inclusive semileptonic branching fraction $\mathcal{B}(B_s^0 \to X^- \ell^+ \nu_\ell)$ at Belle", *Phys.Rev.* D87.7 (2013) 072008,
DOI: `10.1103/PhysRevD.87.072008`,
arXiv: `1212.6400 [hep-ex]`.

[95] H. Hamasaki et al., "Kaon Identification in Belle", Belle Note 321 (internal report), July 2000.

[96] S. Nishida, “Study of the Kaon and Pion Identification Using Inclusive D^* Sample”, Belle Note 779 (internal report), Jan. 2005.

[97] W. Verkerke and D. Kirkby, *The RooFit Toolkit for Data Modeling*, `http://roofit.sourceforge.net/`, 2014.

[98] K. Hanagaki et al., “Electron identification in Belle”, *Nucl.Instrum.Meth.* A485 (2002) 490–503, DOI: `10.1016/S0168-9002(01)02113-1`, arXiv: `hep-ex/0108044 [hep-ex]`.

[99] A. Abashian et al., “Muon identification in the Belle experiment at KEKB”, *Nucl.Instrum.Meth.* A491 (2002) 69–82, DOI: `10.1016/S0168-9002(02)01164-6`.

[100] L. Hinz, “Lepton ID efficiency correction and systematic error”, Belle Note 954 (internal report), July 2006.

[101] P. Urquijo, “Measurement of $B \to D^{(*)} X \ell \nu$ decays”, Belle Note 1251 (internal report), Aug. 2012.

[102] G. C. Fox and S. Wolfram, “Observables for the Analysis of Event Shapes in e+ e- Annihilation and Other Processes”, *Phys.Rev.Lett.* 41 (1978) 1581, DOI: `10.1103/PhysRevLett.41.1581`.

[103] C. Oswald, “Semileptonic B/B_s decays at Belle”, *PoS* ICHEP2012 (2013) 253, arXiv: `1305.3846 [hep-ex]`.

[104] R. Brun and F. Rademakers, “ROOT - An Object Oriented Data Analysis Framework”, *Nucl. Inst. & Meth. in Phys. Res.* A 389 (1997) 81–86.

[105] M. J. Oreglia, “A Study of the Reactions $\psi' \to \gamma\gamma\psi$”, PhD thesis: Stanford University, 1980.

[106] J. Stypula et al., “Evidence for $B^- \to D_s^+ K^- \ell^- \bar{\nu}_\ell$ and search for $B^- \to D_s^{*+} K^- \ell^- \bar{\nu}_\ell$”, *Phys.Rev.* D86 (2012) 072007, DOI: `10.1103/PhysRevD.86.072007`, arXiv: `1207.6244 [hep-ex]`.

[107] P. del Amo Sanchez et al.,
"Observation of the Decay $B^- \to D_s^{(*)+} K^- \ell^- \bar{\nu}_\ell$",
Phys.Rev.Lett. 107 (2011) 041804,
DOI: `10.1103/PhysRevLett.107.041804`,
arXiv: `1012.4158 [hep-ex]`.

[108] P. del Amo Sanchez et al.,
"Dalitz plot analysis of $D_s^+ \to K^+ K^- \pi^+$",
Phys.Rev. D83 (2011) 052001,
DOI: `10.1103/PhysRevD.83.052001`,
arXiv: `1011.4190 [hep-ex]`.

[109] R. Mitchell et al., "Dalitz Plot Analysis of $D_s^+ \to K^+ K^- \pi^+$",
Phys.Rev. D79 (2009) 072008,
DOI: `10.1103/PhysRevD.79.072008`,
arXiv: `0903.1301 [hep-ex]`.

[110] H. W. Kim et al., "Study of High Energy Photon Detection Efficiency Using Radiative Bhabha",
Belle Note 499 (internal report), Apr. 2002.

[111] J. Alexander et al., "Absolute Measurement of Hadronic Branching Fractions of the D_s^+ Meson",
Phys.Rev.Lett. 100 (2008) 161804,
DOI: `10.1103/PhysRevLett.100.161804`,
arXiv: `0801.0680 [hep-ex]`.

[112] B. Eisenstein et al.,
"Precision Measurement of $\mathcal{B}(D^+ \to mu + nu)$ and the Pseudoscalar Decay Constant $f(D^+)$",
Phys.Rev. D78 (2008) 052003,
DOI: `10.1103/PhysRevD.78.052003`,
arXiv: `0806.2112 [hep-ex]`.

[113] P. Urquijo et al., "Measurement Of $|V_{ub}|$ From Inclusive Charmless Semileptonic B Decays",
Phys.Rev.Lett. 104 (2010) 021801,
DOI: `10.1103/PhysRevLett.104.021801`,
arXiv: `0907.0379 [hep-ex]`.

[114] B. Aubert et al., "Study of inclusive B^- and $\bar{B}^0$ decays to flavor-tagged D, D_s and Λ_c^+", *Phys.Rev.* D75 (2007) 072002, DOI: `10.1103/PhysRevD.75.072002`, arXiv: `hep-ex/0606026 [hep-ex]`.

[115] C. Oswald and T. K. Pedlar, "Results in B_s physics and bottomonium spectroscopy using the Belle $\Upsilon(5S)$ data", *Mod.Phys.Lett.* A28 (2013) 1330036, DOI: `10.1142/S021773231330036X`, arXiv: `1311.3547 [hep-ex]`.

[116] S. Esen et al., "Precise measurement of the branching fractions for $B_s \to D_s^{(*)+} D_s^{(*)-}$ and first measurement of the $D_s^{*+} D_s^{*-}$ polarization using e^+e^- collisions", *Phys.Rev.* D87.3 (2013) 031101, DOI: `10.1103/PhysRevD.87.031101`, arXiv: `1208.0323`.

[117] M. Feindt et al., "A Hierarchical NeuroBayes-based Algorithm for Full Reconstruction of B Mesons at B Factories", *Nucl.Instrum.Meth.* A654 (2011) 432–440, DOI: `10.1016/j.nima.2011.06.008`, arXiv: `1102.3876 [hep-ex]`.

[118] P. Urquijo et al., "Moments of the electron energy spectrum and partial branching fraction of $B \to X_c e \nu$ decays at Belle", *Phys.Rev.* D75 (2007) 032001, DOI: `10.1103/PhysRevD.75.032001`, arXiv: `hep-ex/0610012 [hep-ex]`.

[119] C. Schwanda et al., "Moments of the Hadronic Invariant Mass Spectrum in $B \to X_c \ell nu$ Decays at Belle", *Phys.Rev.* D75 (2007) 032005, DOI: `10.1103/PhysRevD.75.032005`, arXiv: `hep-ex/0611044 [hep-ex]`.

[120] B. Aubert et al., "Measurement and interpretation of moments in inclusive semileptonic decays $\bar{B} \to X_c \ell^- \bar{nu}$", *Phys.Rev.* D81 (2010) 032003, DOI: `10.1103/PhysRevD.81.032003`, arXiv: `0908.0415 [hep-ex]`.

[121] R. Faustov and V. Galkin, "Charmless weak B_s decays in the relativistic quark model", *Phys.Rev.* D87.9 (2013) 094028, DOI: `10.1103/PhysRevD.87.094028`, arXiv: `1304.3255`.

[122] C. Albertus et al., "$\bar{B}_s \to K$ semileptonic decay from an Omnès improved constituent quark model", *Phys.Lett.* B738 (2014) 144–149, DOI: `10.1016/j.physletb.2014.09.037`, arXiv: `1404.1001 [hep-ph]`.

[123] U.-G. Meißner and W. Wang, "$B_s \to K^{(*)}\ell\bar{\nu}$, Angular Analysis, S-wave Contributions and $|V_{ub}|$", *JHEP* 1401 (2014) 107, DOI: `10.1007/JHEP01(2014)107`, arXiv: `1311.5420 [hep-ph]`.

[124] S. Athar et al., "Study of the q^2 dependence of $B \to \pi\ell\nu$ and $B \to \rho(\omega)\ell\nu$ decay and extraction of $|V_{ub}|$", *Phys.Rev.* D68 (2003) 072003, DOI: `10.1103/PhysRevD.68.072003`, arXiv: `hep-ex/0304019 [hep-ex]`.

[125] A. Sibidanov et al., "Study of Exclusive $B \to X_u\ell\nu$ Decays and Extraction of $|V_{ub}|$ using Full Reconstruction Tagging at the Belle Experiment", *Phys.Rev.* D88.3 (2013) 032005, DOI: `10.1103/PhysRevD.88.032005`, arXiv: `1306.2781 [hep-ex]`.

[126] J. Lees et al., "Evidence for an excess of $\bar{B} \to D^{(*)}\tau^-\bar{\nu}_\tau$ decays", *Phys.Rev.Lett.* 109 (2012) 101802, DOI: `10.1103/PhysRevLett.109.101802`, arXiv: `1205.5442 [hep-ex]`.

Danksagung

Allen voran bedanke ich mich bei Jochen Dingfelder und Phill Urquijo für die Betreuung meiner Doktorarbeit. In den letzten vier Jahren habe ich viel gelernt, nicht nur in fachlicher, sondern auch in menschlicher Hinsicht. Sie brachten mir zahlreiche handwerkliche Kniffe bei und gaben wertvolle Tipps, wie man wissenschaftlichen Texten den letzten Feinschliff gibt. Bei Fragen und Problemen stand ihre Tür immer offen. Wo es nur ging, förderten sie meine Arbeit und unterstützten meine Ideen. Nicht zuletzt gaben sie immer den Antrieb, das Erreichte noch weiter zu verbessern.

Ich möchte auch meinen Kollegen aus der Belle-Kollaboration danken, im Besonderen der CKM-Arbeitsgruppe unter der Leitung von Christoph Schwanda und dem Review-Komitte meiner Analysen, Maria Rozanska, Kay Kinoshita und Tadao Nozaki. Sie alle haben wichtige Anregungen gegeben haben und meine Analysen mit den richtigen, kritischen Fragen begleitet und vorangetrieben.

An meine Kollegen aus der Arbeitsgruppe in Bonn: Aga, Benedikt, Birgit, Bruno, Carlos, Cesar, David, Dennis, Elisabeth, Federico, Florian, Holger, Jan, Jessica, Klara, Luis, Michael, Sascha, Sonja, Stephan, Thomas und Will – vielen Dank für die schöne Zeit in- und außerhalb des Instituts. Ohne Euch wäre es fad gewesen!

Des Weiteren danke ich der Rheinischen Friedrich-Wilhelms Universität Bonn für die Unterstützung meines Promotionsprojekts durch ein Stipendium im Rahmen der individuellen Graduiertenförderung.

Schließlich danke ich meiner Familie und meinen Freunden, die mich während der ganzen Zeit begleiteten und mir auch in schwierigen Phasen zur Seite standen. Danke für die Unterstützung und die manchmal notwendige Ablenkung von der Physik!